Microstructural Evolution in Commercial Ni-based Alloys under Irradiation

by

Li-Jen Yu

A dissertation submitted in partial fulfillment
of the requirements for the degree of
Doctor of Philosophy
(Materials Science and Engineering)
in the University of Michigan
2020

Doctoral Committee:

Professor Emmanuelle Marquis, Chair
Associate Professor Kevin G. Field
Professor Amit Misra
Assistant Professor Liang Qi

Li-Jen Yu

ljezrayu@umich.edu

ORCID iD: 0000-0002-5675-8668

© Li-Jen Yu 2020

ACKNOWLEDGEMENTS

I would like to express my sincere gratitude to my advisor, Dr. Emmanuelle Marquis, for her support, guidance, patience, and constructive advice throughout my Ph.D. journey. I would also like to thank my committee members, Dr. Kevin G. Field, Dr. Amit Misra, and Dr. Liang Qi, for providing helpful suggestions to improve this dissertation.

I would like to acknowledge the funding from the U.S. Department of Energy's Nuclear Energy University Program. I gratefully recognize Dr. Julie Tucker and Dr. Grace Burke for providing the alloys. I am thankful for the technical support from the staff at the Michigan Center for Materials Characterization and the Michigan Ion Beam Laboratory.

Special thanks to the previous and current members of Marquis Research Group for your friendship. I really enjoyed working and chatting with you all.

Great thanks to my church family members for your kindness every Sunday. Especially, I want to thank Heather and Pete for always taking care of me.

Huge thanks to my roommate, Michael, who helped me a lot over the past four years. I am really glad that I can have such a nice roommate. I am also grateful to my friend, Jia-Hong, for many fruitful discussions.

Lastly, I would not have been able to complete this journey without the encouragement from my parents. Thank you for your unconditional love and your prayers. To my brother, Daniel, and my sister, Esther: I am glad that you two were also in the U.S. during these years so that we can

chat, share our feelings together, and support each other. I would also like to thank my girlfriend, Yu-Shan (Sandy), for your company. Thank you for waiting for me, especially when we were separated across the Pacific Ocean. Finally, thank you God for all the blessings you have given me.

TABLE OF CONTENTS

LIST OF TABLES

LIST OF FIGURES

LIST OF APPENDICES

LIST OF ABBREVIATIONS AND ACRONYMS

AOI: Area of interest

APT: Atom probe tomography

BCO: Body-centered orthorhombic

BCT: Body-centered tetragonal

BWR: Boiling water reactor

CANDU: Canada Deuterium Uranium

DPA: Displacements per atom

EDM: Electrical discharge machining

EDS: Energy-dispersive X-ray spectroscopy

FCC: Face-centered cubic

FIB: Focused ion beam

LWR: Light water reactor

PKA: Primary knock-on atom

PWR: Pressurized water reactor

RED: Radiation-enhanced diffusion

RIP: Radiation-induced precipitation

RIS: Radiation-induced segregation

SEM: Scanning electron microscopy

STEM: Scanning transmission electron microscopy

TEM: Transmission electron microscopy

ABSTRACT

Lifetime extensions of current light water reactors and operational conditions of future advanced reactors involve higher irradiation damage levels, elevated service temperatures, and more aggressive corrosion conditions, and place greater burdens on reactor structural components. Hence, maintaining safe reactor operation requires that selected structural materials should sustain these harsh service conditions, and consequently that we understand microstructure and property changes that might take place during service. Commercial Ni-based superalloys continue to be considered for nuclear applications due to their superior mechanical properties and corrosion resistance at relevant reactor service temperatures. Specifically, Alloy 625, Alloy 625 Plus, and Alloy 690 are proposed for use as in-core reactor components. However, little is known about their precipitation behavior under irradiation.

This study aims to quantify irradiated microstructures developing in three commercial Ni-based alloys (Alloy 625, Alloy 625 Plus, and Alloy 690) after ion and proton irradiations, to clarify the underlying mechanisms controlling microstructural evolution, and to extrapolate the findings to neutron irradiation and reactor conditions. Transmission electron microscopy and atom probe tomography investigations indicated that the irradiated microstructures result from competing cascade mixing and radiation-enhanced diffusion. In addition to irradiation conditions, alloy composition, via thermodynamic driving force and kinetics, plays a significant role in controlling microstructural evolution. While the starting alloy state, i.e. solutionized or aged, may influence phase decomposition pathways, the precipitate microstructures eventually converged to non-

equilibrium steady states with constant averaged size and number density defined by temperature and dose rate. Specifically, precipitation toward a non-equilibrium steady state nanoscale patterning and solute segregation were observed in alloys after lower dose rate proton irradiation, while higher dose rate ion irradiation led to randomization of all solute distributions. In addition, different cavity evolution and phases were observed in these alloys, confirming the importance of chemistry in controlling precipitation driving force and point defect behavior.

Chapter 1

Introduction

1.1 Motivation and background

To continuously provide clean and reliable energy, the United States government has renewed the operating licenses of ~90% (89 out of 97) of the currently existing commercial nuclear reactors as of 2019 [1]. The license renewal would authorize the nuclear power plants to operate for 60 years or beyond [2]. This life extension means that structural materials making up existing nuclear power plants will be subjected to higher radiation damage or doses, extended thermal exposure, and longer corrosion periods. Consequently, significant changes in the microstructures and mechanical properties are also expected. In addition, to meet the increasing energy demand, several types of advanced nuclear reactors combining sustainability, better thermal efficiency, and reduced cost and nuclear waste, have been proposed [3]. These advanced reactors will operate at higher temperatures, to higher radiation doses, and under more corrosive conditions than the current light water reactors (LWRs) [4, 5]. Overall, the structural materials that are either used in the current reactors for life extension, or projected to be used in future reactors, need to have improved resistance to irradiation, thermal exposure, and corrosion. Selected materials need to be qualified for these purposes, requiring we understand how their microstructures change under the relevant service conditions.

To fulfill the requirements of operating in more severe environments, commercial Ni-based alloys continue to be considered for nuclear applications due to their superior mechanical

properties and corrosion resistance at relevant reactor temperatures [6-8]. Alloy X-750 and Alloy 718 are precipitation-hardened alloys that are commonly used as core internals such as fuel assembly hold-down springs, control rod guide tube support pins, structural bolts, and spacer grids in currently operating LWRs [8]. Outside the reactor core, Alloy 690 serves as control rod drive mechanism housing and steam generator tubing [5, 9]. Besides applications in current LWRs, several other Ni-based alloys have been proposed as promising candidate materials for in-core components in LWRs with extended lifetimes and in future advanced reactors [10-12]. These alloys include, but are not limited to Alloy 625, Alloy 625 Plus, and Alloy 690 [10-12]. In-core structural materials are exposed to neutron irradiation. For instance, Alloy 625 used as fastener materials would receive irradiation dose to ~3 dpa in a 60-year service [13]. Alloy 625 and Alloy 690 utilized as fuel cladding in a supercritical water reactor would be subjected to a dose of ~30 dpa after 40 years [12]. Though these alloys are used in current reactors, little is known about their precipitation behavior under irradiation.

Investigating microstructural evolution under reactor conditions is a challenge. In addition to access and uncontrolled experimental conditions, the steep cost, prolonged irradiation time frame, and radioactive concerns associated with neutron irradiation experiments add to the limitations [14]. Alternatively, charged particles (ions and protons) are more feasible for irradiation experiments because of the flexibility to control irradiation conditions, higher dose accumulation rate, and little (for protons) or no (for heavy ions) radioactivity of irradiated samples [15]. Therefore, ions and protons have been used as surrogates for neutrons. However, intrinsic differences between charged particle and neutron irradiations, including damage rate, cascade morphology, and transmutation reactions, can lead to very different irradiated microstructures [16, 17]. Thus, understanding the effect of irradiation conditions on the resulting microstructures

is essential for reasonable interpretation and for further inference of neutron irradiated microstructures.

Focusing on three alloys, Alloy 625, Alloy 625 Plus, and Alloy 690 that were proposed as candidate materials for use as in-core components in LWRs with extended lifetimes and in future advanced reactors, this thesis addresses two aspects:

1. The irradiated microstructures of selected commercial Ni-based alloys at relevant reactor working temperatures, with regard to precipitation behavior as well as cavity and dislocation loop formation, are strongly related to mechanical properties. Therefore, we seek to understand what phases form under irradiation in the three selected alloys, how these phases, cavities, and dislocation loops evolve with irradiation doses, and the mechanisms related to the phase, cavity, and dislocation loop evolution.

2. Since irradiation conditions, in terms of dose rate, temperature, and irradiating particles, and alloy composition play an important role on precipitation, cavity, and dislocation loop evolution, we seek to understand the interplay between dose rate and temperature in controlling precipitate size and number density, the role of alloy composition in the development of the irradiated microstructures, and the mechanisms controlling microstructure development.

1.2 Thesis structure

Following the introduction in **Chapter 1**, **Chapter 2** provides the current microstructural understanding of the three commercial Ni-based alloys, a review of the current literature on the microstructural evolution of relevant Ni-based alloys under irradiation, a summary of some of the

open issues that need to be addressed, and hypotheses. **Chapter 3** analyzes the different precipitation behaviors between Alloy 625 and Alloy 625 Plus under thermal aging, and serves as a basis for further comparisons with the precipitation behavior under irradiation. In **Chapter 4**, the precipitation behavior of Alloy 625 Plus under irradiation is first quantified. The differences between the irradiated microstructures of Alloy 625 Plus and the other two alloys are described and analyzed in **Chapter 5**. **Chapter 6** focuses on the cavity and dislocation loop evolution in the three alloys. Finally, the conclusions and suggested future research directions are presented in **Chapter 7**.

Chapter 2

Literature Review

This chapter first outlines several common classes of structural materials and concerns for these materials in nuclear power plants. Then, the literature on precipitation in Alloy 625, Alloy 625 Plus, Alloy 690, as well as other relevant Ni-based alloys under thermal aging and irradiation is reviewed, focusing on strengthening phases (γ' and γ'') and Pt_2Mo-type ordered phase. Cavity and dislocation loop evolutions in pure Ni and relevant Ni-based alloys are also included.

2.1 Structural alloys in nuclear power systems

Nuclear energy has been considered as one of the reliable and important energy sources with low greenhouse gas emission. About 20% of the U.S. electricity generation was from nuclear energy in 2019 [18]. The safe and reliable operation of nuclear reactors relies considerably on the stable performance of structural materials under aggressive conditions, including elevated temperatures, corrosive environment, and irradiation damage. Nuclear power plants in the U.S. use either a boiling water reactor (BWR) or a pressurized water reactor (PWR), both of which are classified as light water reactors (LWRs), and PWRs account for about 66% of the reactors [19]. In a PWR, water in the primary circuit is kept in high pressure to prevent it from boiling at the operating temperature around 300 °C. This water carries the heat generated from reactor core, and flows through the tubes in a steam generator to heat up the water in the secondary circuit and turn it into steam, which drives the turbines to generate electricity. Thus, structural materials used in the primary circuit are subjected to high temperature pressurized water. Structural materials used

in core internals suffer irradiation damage from neutrons, which can exceed 100 displacements per atom (dpa) as the operating lifetime of reactors extends over 60 years [6]. In addition to currently operating reactors, proposed advanced reactors can have more severe operating conditions, including working temperatures over than 300 °C and up to 1000 °C, corrosive coolant such as molten salts, and irradiation damage up to 200 dpa [5, 12]. Overall, the combination of high operating temperature, corrosive environment, and irradiation damage is the main concern for structural materials in nuclear power systems.

Under the harsh reactor conditions, material degradation is common and includes hardening, embrittlement, volumetric swelling, or stress corrosion cracking, which can lead to component failure or safety issues. Therefore, different structural alloys find their own applications based on their unique properties. In the LWR core, Zr-based alloys are used as fuel cladding due to their low neutron absorption cross section, as well as adequate mechanical properties and high temperature corrosion resistance [20]. Low-alloy ferritic steels serve in pressure vessel of LWRs, while high-Cr ferritic/martensitic steels are candidate materials in advanced reactors [21]. The main advantage of ferritic/martensitic steels is their better swelling resistance over austenitic stainless steels [22]. Austenitic stainless steels are the most common structural alloys in nuclear reactors with broad applications for in-core and out-of-core components due to decent cost, mechanical properties, and corrosion responses [6]. Ni-based alloys are usually used as steam generator tubing materials outside the reactor core, owing to their high temperature corrosion resistance [7, 9]. Precipitation-hardened Ni-based alloys are used as high-strength in-core components, including bolts and springs because of their high temperature mechanical properties [23, 24]. In-core Ni-based alloys are subjected to neutron irradiation. For example, fastener materials would receive irradiation dose to ~3 dpa in a 60-year service [13], and fuel cladding materials would be exposed to a dose of ~30

dpa after 40 years in a supercritical water reactor [12].

The following sections focus on the thermal aging and irradiation responses of the three commercial Ni-based alloys (Alloy 625, Alloy 625 Plus, and Alloy 690) investigated in this thesis, as well as the microstructural changes of other relevant Ni-based alloys under irradiation.

2.2 Commercial Ni-based alloys investigated in this study

2.2.1 Alloy 625

Alloy 625 is a highly alloyed commercial Ni-based alloy with high strength, corrosion resistance, fabricability and weldability [25]. Alloy 625 has been used in aerospace, chemical processing, oil production, and marine industries [26]. The typical composition of Alloy 625 is listed in **Table 2.1**. Although originally designed as a non-age-hardenable and solid-solution strengthened alloy [27], precipitates such as γ″, δ, and Pt_2Mo-type ordered phase form after thermal aging and strongly affect the mechanical properties of Alloy 625 [28]. The details of these three precipitate phases are listed in **Table 2.2** and **Figure 2.1**.

Table 2.1. Nominal compositions (at.%) of the alloys.

Alloy	Ni	Cr	Mo	Fe	Nb	Ti	Al	Si	Co	Mn	P	S	C	Ta
625	61.8	25.6	5.43	3.73	2.28	0.29	0.37	0.17	0.03	0.06	<0.01	<0.01	0.20	<0.01
625 Plus	60.8	23.9	4.94	6.00	2.16	1.58	0.44	0.06	-	0.02	0.02	<0.01	0.04	-
690	56.6	31.7	<0.01	10.4	<0.01	0.41	0.48	0.1	<0.01	0.15	<0.01	<0.01	0.14	-

Table 2.2. Crystal structures and compositions of Pt_2Mo-type ordered phase, γ″, γ′, and δ phases [25, 29, 30].

Phase	Structure (Prototype/ Pearson Symbol/ Strukturbericht Designation/ Space Group)	Lattice parameters	Typical composition
Pt_2Mo-type ordered phase	BCO (Pt_2Mo/ oI6/ $D0_{2h}^{25}$/ Immm)	a = $3a_\gamma/\sqrt{2}$ b = $a_\gamma/\sqrt{2}$ c = a_γ	Ni_2Cr $Ni_{0.63}Cr_{0.30}Mo_{0.07}$
γ″	BCT (Al_3Ti/ tI8/ $D0_{22}$/ I4/mmm)	a = 0.36 nm c = 0.74 nm	Ni_3(Nb, Ti, Al)
γ′	FCC (Cu_3Au/ cP4/ $L1_2$/ $Pm\bar{3}m$)	a = 0.36 nm	Ni_3(Al, Ti)
δ	Orthorhombic (Cu_3Ti/ oP8/ $D0_a$/ Pmmn)	a = 0.51 nm b = 0.42 nm c = 0.45 nm	Ni_3Nb

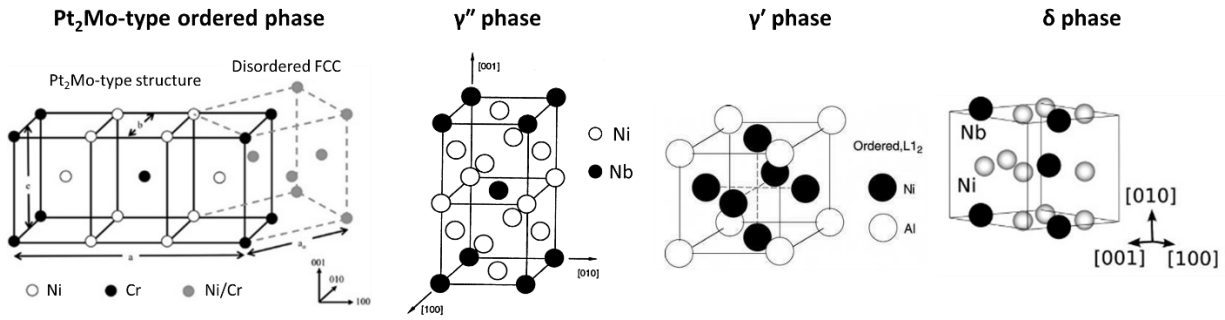

Figure 2.1. Atom arrangements in Pt_2Mo-type ordered phase, γ″, γ′, and δ phases. (Adapted from [29-32])

Rather than the typical face-centered cubic (FCC) γ′ strengthening phase found in other Ni-based alloys, the body-centered tetragonal (BCT) Ni_3(Nb, Ti, Al) γ″ coherent precipitates form in Alloy 625 after thermal aging within 550 to 750 °C [25, 33, 34]. The orientation relationship between the γ″ precipitates and γ matrix is $(0\ 0\ 1)_{\gamma''}$ // $\{1\ 0\ 0\}_\gamma$ and $[0\ 0\ 1]_{\gamma''}$ // $<1\ 0\ 0>_\gamma$, resulting in the formation of three variants. γ″ precipitates were observed to be nearly spherical for small

sizes, and changing to a lens morphology for aging time longer than 100 h at 650 °C [34]. δ phase forms in Alloy 625 after thermal aging between 650 to 900 °C [34, 35]. Below 800 °C, δ precipitation is preceded by γ″ precipitation, and the metastable γ″ phase completely dissolved after longer aging treatment [35]. Above 800 °C, δ phase precipitates directly from the γ matrix [35]. The orientation relationship between δ and γ matrix is $(0\ 1\ 0)_\delta$ // $\{1\ 1\ 1\}_\gamma$ and $[1\ 0\ 0]_\delta$ // $<\bar{1}\ 0>_\gamma$. The morphologies of γ″ precipitates and δ precipitates are shown in **Figure 2.2**.

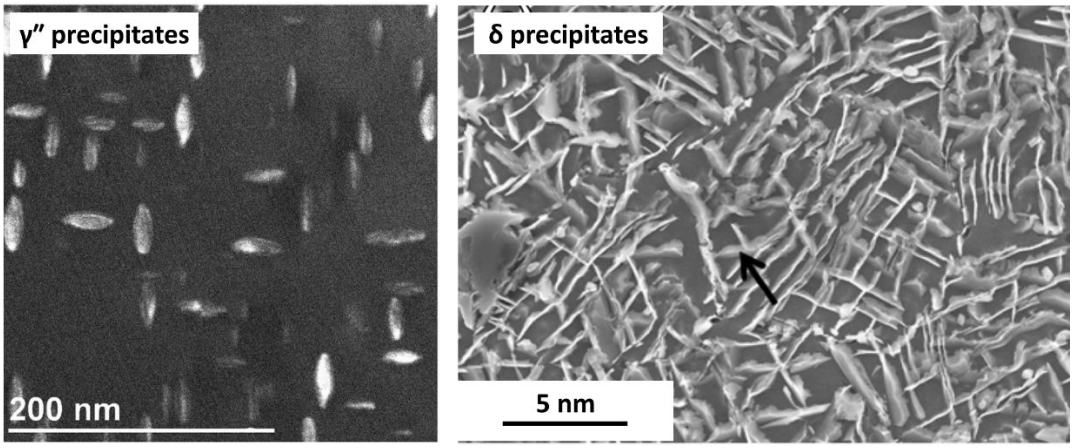

Figure 2.2. (Left) Transmission electron microscopy dark-field (TEM-DF) image of γ″ precipitates in Alloy 625 after thermal aging at 650 °C for 200 h (Adapted from [36]). (Right) Scanning electron microscopy (SEM) image of δ precipitates in Alloy 625 after thermal aging at 750 °C for 1000 h. (Adapted from [34])

Alloy 625 is susceptible to the formation of a body-centered orthorhombic (BCO) Pt_2Mo-type ordered phase. The morphology of the Pt_2Mo-type ordered precipitates is shown in **Figure 2.3**. Generally, in binary Ni-Cr alloys with compositions close to Ni-33Cr (at.%), the disordered solid solution undergoes ordering, forming the Pt_2Mo-type Ni_2Cr ordered phase during thermal aging below the order-disorder transformation temperature. The calculated binary Ni-Cr phase diagram

is shown in **Figure 2.4** [37]. This phase increases strength, decreases ductility, and promotes brittle fracture in Ni-Cr binary alloys [38]. In Ni-Cr-Fe ternary alloys, one study reported Fe has little influence on the ordering rate and decreases the critical temperature of ordering transformation [38]. Conversely, another study claimed Fe reduces the ordering kinetics [39]. In Ni-Cr-Mo ternary alloys, the Pt_2Mo-type ordered phase also forms during thermal aging, and causes the increase in hardness [40]. Since Alloy 625 is a Ni-Cr-Mo based alloy, the formation of this phase is expected. Indeed, the Pt_2Mo-type ordered phase was observed in Alloy 625 after prolonged aging, i.e. 50,000 h at 500 °C [41], 60,000 h at 600 °C [28], and 70,000 h at 600 °C [29]. However, these studies focused on service-exposed alloys, and thus, the onset of the ordering reaction in Alloy 625 was not determined. At temperatures above 650 °C, the ordered phase is no longer stable and dissolves [28, 29].

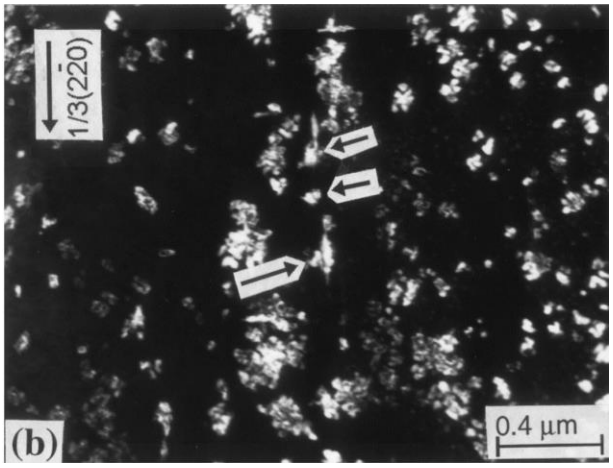

Figure 2.3. TEM-DF image of Pt_2Mo-type ordered precipitates in Alloy 625 after thermal aging at ~600 °C for 70,000 h. (Adapted from [29])

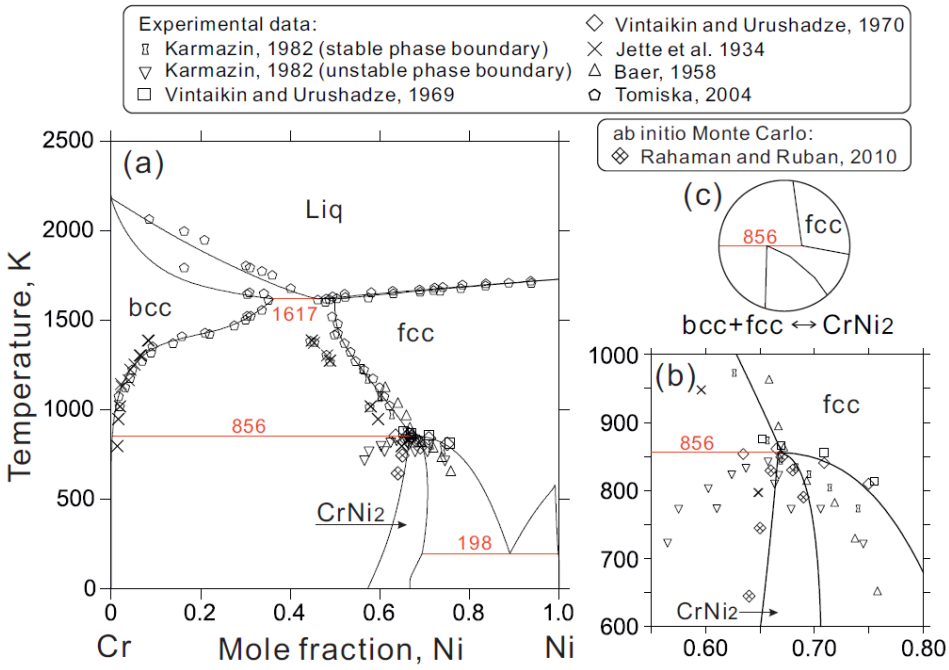

Figure 2.4. Calculated Ni-Cr phase diagram. (Adapted from [37])

2.2.2 Alloy 625 Plus

Alloy 625 Plus is an optimized version of Alloy 625, and has been used in oil field and marine applications [42]. Alloy 625 Plus has lower Ni, Cr, and Mo concentrations yet higher Ti and Fe concentrations compared to Alloy 625. The nominal composition of Alloy 625 Plus is listed in **Table 2.1**. The development and design of Alloy 625 Plus were motivated by a need to improve the age-hardening capability and maintain the corrosion resistance of Alloy 625 [42]. Alloy 625 Plus is also strengthened by γ″ phase [43]. However, phase stability as a function of temperature and formation kinetics of γ″ as well as other possible phases such as γ′, δ or Pt_2Mo-type phase have not been reported in the open literature.

2.2.3 Alloy 690

Alloy 690 is another Ni-Cr-Fe-based commercial Ni-based alloy widely used in LWRs as a steam generator tubing material in replacement of Alloy 600 [9]. Its attractive performance is linked to the good resistance to corrosion in various aqueous environments within temperatures used in nuclear steam generators [44]. Unlike Alloy 625 and Alloy 625 Plus, Alloy 690 is not a precipitation-strengthened alloy. Its simpler composition compared to Alloy 625 and Alloy 625 Plus is listed in **Table 2.1**. Alloy 690 is also susceptible to the formation of Pt_2Mo-type ordered phase. Embryos of long range ordered domains were observed after thermal aging at 475 °C for 32,000 h [45]. The ordered phase was also confirmed by TEM diffraction spots after thermal aging at 420 °C for 70,000 h [46]. However, at lower temperatures, kinetics are very slow and no ordering was observed after aging for up to 90,000 h at ~360 °C [46, 47]. It was also suggested that the critical temperature of order-disorder transformation decreases as Fe content increases in Ni-Cr-Fe based alloys [38].

2.3 Microstructural responses of Ni-based alloys under irradiation

2.3.1 Radiation damage in metals

A radiation damage event in metals starts with the interaction between energetic incident particles and lattice atoms. As an energetic incident particle enters the crystal and collides with a lattice atom, a recoil energy can be transferred to the lattice atom. Once the recoil energy is higher than the threshold displacement energy, the lattice atom can be displaced from its original lattice site, leading to the formation of a displaced atom and a vacant site [48]. The first atom displaced by the incident particle is called the primary knock-on atom (PKA). The creation of a PKA takes

about 10^{-18} s [49]. As long as the PKA has enough energy, it can initiate a series of collisional processes (a displacement cascade) after ~0.1 ps by creating additional knock-on atoms, which can further displace other atoms and so forth. The cascade can further evolve into a thermal spike (heat spike) when multiple collisions occur simultaneously and near each other. The high energy density of a thermal spike can cause a local melting of the lattice, leading to a mixing or disordering of lattice atoms [50]. The thermal spike then quenches down after ~10 ps as the energy in the cascade region dissipates into the surrounding lattice. During the quenching stage, most of the defects (displaced atoms and vacant sites) recombine within the cascade. Hence, the fraction of defects (damage efficiency) that survive during cascade quench is typically less than unity [51]. The surviving defects (freely migrating defects), including point defects (vacancies and interstitials) and defect clusters, start migrating throughout the lattice. A schematic illustration and time scales of the development of a cascade damage event are summarized in **Figure 2.5** [52].

The cascade morphology depends on the type of incident particles [16], as illustrated in **Figure 2.6**. Electron irradiation can only produce isolated vacancy-interstitial pairs without cascades due to the small recoil energy (~60 eV when 1 MeV electrons collide with Ni [16]). Protons have a larger mass compared to electrons, and thus, can generate small and widely spaced cascades. Neutrons and ions tend to impart a higher recoil energy to PKAs (~5 keV and ~35 keV when 1 MeV ions and neutrons collide with Ni, respectively [16]) and create denser cascades. Hence, significant in-cascade annihilation of defects occurs during the cascade quenching under neutron and ion irradiations. Consequently, damage efficiency decreases with increasing recoil energy [53], and neutrons and ions yield lower damage efficiencies (~2% and ~4%, respectively) than protons (~25%) and electrons (~100%) [16].

The production of defects during irradiation gives rise to an increased defect concentration

compared to the thermal equilibrium defect concentration. The defect concentration during irradiation can be estimated by solving the steady state solutions of simple defect balance equations [54]:

$$\frac{dC_v}{dt} = K_0 - K_{iv}C_vC_i - K_{vs}C_vC_s; \quad \frac{dC_i}{dt} = K_0 - K_{iv}C_vC_i - K_{is}C_iC_s$$

where C_v is vacancy concentration, C_i is interstitial concentration, K_0 is defect production rate, K_{iv} is vacancy-interstitial recombination rate coefficient, K_{vs} is vacancy-sink reaction rate coefficient, and K_{is} is interstitial-sink reaction rate coefficient. Defects disappear either by mutual recombination with anti-type defects or by reaction with defect sinks. When defects loss to recombination and loss to sinks are both at play, the steady state defect concentrations are approximate by:

$$C_v = \frac{-K_{is}C_s}{2K_{iv}} + \left[\frac{K_0K_{is}}{K_{iv}K_{vs}} + \frac{K_{is}^2C_s^2}{4K_{iv}^2}\right]^{1/2}; \quad C_i = \frac{-K_{vs}C_s}{2K_{iv}} + \left[\frac{K_0K_{vs}}{K_{iv}K_{is}} + \frac{K_{vs}^2C_s^2}{4K_{iv}^2}\right]^{1/2}$$

When defects loss to recombination is dominated and loss to sinks is negligible, the steady state defect concentrations can be simplified to be:

$$C_v = \left[\frac{K_0K_{is}}{K_{iv}K_{vs}}\right]^{1/2}; \quad C_i = \left[\frac{K_0K_{vs}}{K_{iv}K_{is}}\right]^{1/2}$$

When recombination is negligible and defects are lost by migrating to sinks, the steady state concentrations are:

$$C_v = \frac{K_0}{K_{vs}C_s}; \quad C_i = \frac{K_0}{K_{is}C_s}$$

Once the defect concentrations are known, the radiation-enhanced diffusion coefficient can be estimated. An example of the difference between the radiation-enhanced diffusion coefficient and the thermal diffusion coefficient in a Ni-based alloy under the irradiation dose rate of 10^{-6} dpa/s is shown in **Figure 2.7** [55]. The radiation-enhanced diffusion coefficient can be over 6 orders of magnitude higher than the thermal diffusion coefficient at ~300 °C [55].

The freely migrating defects that survive from the cascade quench can further alter microstructures or local chemical compositions. Microstructural features and phenomena during irradiation include but are not limited to voids (empty cavities), bubbles, dislocation loops, stacking faults, solute segregation or depletion, and induced or enhanced precipitation of phases. The following sections mainly focus on the precipitation behavior as well as cavity and dislocation loop evolutions under irradiation in relevant Ni-based alloys.

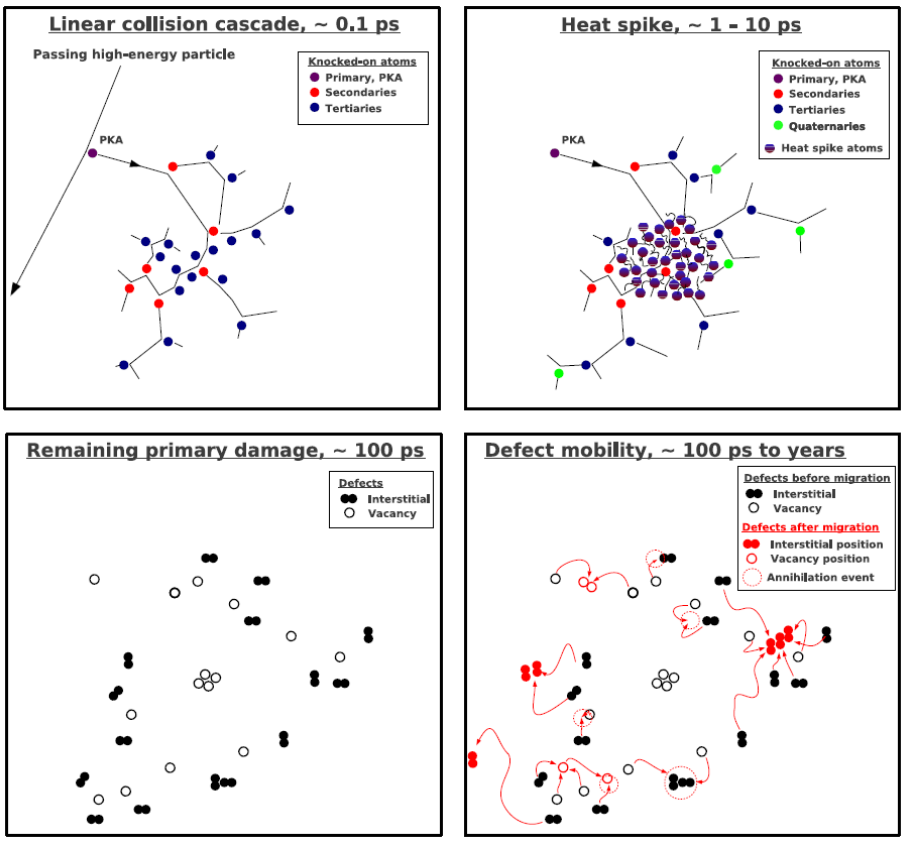

Figure 2.5. Schematic illustration and time scales of the development of a radiation damage event. Top left: collisional processes during the initial displacement cascade; top right: thermal spike (heat spike) formation; bottom left: formation of surviving defects after cascade quenching; bottom right: defects migration. (Adapted from [52])

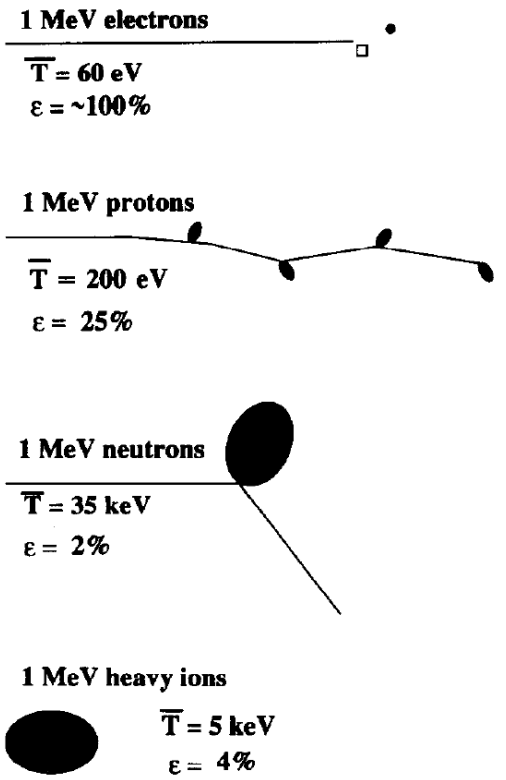

Figure 2.6. Schematic illustration of cascade morphologies generated by 1 MeV incident electrons, protons, neutrons, and ions in pure Ni. $\bar{T}$ is the average recoil energy per PKA, and ε is the displacement efficiency of freely migrating defects. (Adapted from [16])

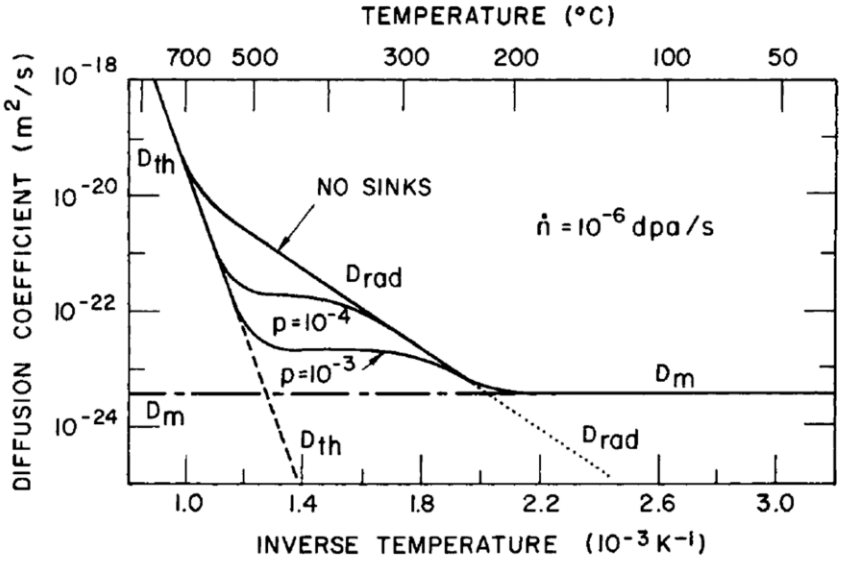

Figure 2.7. Diffusion coefficient as a function of temperature in a Ni-based alloy under

irradiation at the dose rate of 10^{-6} dpa/s. D_{rad} is the radiation-enhanced diffusion coefficient, D_{th} is the thermal diffusion coefficient, D_m is the diffusion coefficient resulting from cascade mixing, and ρ is the probability that a defect is annihilated at a sink. (Adapted from [55])

2.3.2 General precipitation behavior under irradiation

Irradiation can significantly change the precipitation behavior and stability of the precipitated phases through several different mechanisms, including radiation-enhanced diffusion, radiation-induced segregation, and cascade mixing. Under irradiation, the alloy system is away from its thermal equilibrium state as a high defect concentration is maintained. This high defect concentration can result in radiation-enhanced diffusion (RED), as discussed in **2.3.1**, and the formation rate of thermodynamically stable phases that would otherwise be kinetically-limited under thermal conditions, is significantly accelerated under irradiation [56].

Radiation-induced segregation (RIS) can also alter the phase stability under irradiation. RIS is a non-equilibrium process leading to elemental redistribution (segregation or depletion) at defect sinks, such as dislocations, grain boundaries, or free surfaces. The excessive defects produced during irradiation tend to migrate toward defect sinks at temperatures where they are mobile. When a given element is preferentially associated with the defect flux toward defect sinks, segregation/depletion can occur. RIS is typically explained by the inverse Kirkendall effect and/or the formation and migration of solute-defect complexes [57, 58]. During irradiation, defect fluxes toward defect sinks can induce a net flux of elements toward or away from sinks. When vacancy diffusion dominates, elements with the lower vacancy diffusion coefficients might enrich at sinks, while elements with higher vacancy diffusion coefficients deplete at sinks [59]. Additionally, RIS can also occur when a specific solute element binds with point defects to form solute-defect complexes and the complexes migrate toward defect sinks. For example, RIS of Si in Ni-based

alloys under irradiation has been explained by the formation and migration of Si-interstitial complexes [57, 60-62]. Regardless of the mechanisms of RIS, once the local concentration of the segregated element at these sinks exceeds the solubility limit, non-equilibrium precipitation of phases (radiation-induced precipitation, RIP) can take place. In undersaturated solid solution Ni-Si alloys, RIP of Ni_3Si on dislocation loops were observed under both ion (2×10^{-3} and 2×10^{-4} dpa/s up to 10 dpa) [63] and electron (1.5×10^{-3} to 8.7×10^{-5} dpa/s up to 1 dpa) [64] irradiations at ~500 °C. RIS is dependent on temperature and dose rate. RIS typically occurs at temperatures between ~30% and ~60% of the alloy melting temperature [65]. At low temperatures, defects are immobile and mainly annihilate by mutual recombination. At high temperatures, thermal defect concentrations are sufficient to increase back diffusion of solute elements, leading to the suppression of RIS. The dose rate dependence of RIS is mainly related to the competition between defect recombination and defect loss to sinks. At a given temperature, defects are produced slowly and separately at lower dose rates, and thus, are more likely to reach sinks rather than encounter anti-type defects and recombine. Therefore, greater RIS is expected.

In contrast to RED and RIS that enhance or induce the formation of phases, cascade mixing can cause the destruction of precipitates. Atoms can be ejected from precipitates into the matrix when a displacement cascade occur, leading to precipitate dissolution or disordering [66-70]. As mentioned in **2.3.1**, since neutrons and ions produce larger cascades than protons, a stronger mixing effect is expected. The cascade mixing rate scales with damage rate, and thus, precipitates are expected to be further destabilized at higher dose rates.

Overall, the stability of precipitates is dependent on cascade mixing and radiation-enhanced diffusion (RED) [66-70]. Displacement cascade can eject atoms from precipitates into matrix and randomize the spatial distribution of atoms. RED can drive the alloy system toward equilibrium

predicted by thermodynamics. Therefore, the competition between RED and cascade mixing can lead to different microstructural regimes [71], as schematically illustrated in **Figure 2.8**. At low dose rates or high temperatures (but within the solubility limit of the precipitate), where diffusion overcomes the effect of cascade mixing, accelerated coarsening of thermodynamically stable phases can take place [72-75]. At high dose rates or low temperatures, where cascade mixing dominates and diffusion is insignificant to oppose cascade mixing, precipitates can completely disorder and dissolve, and the alloy evolves toward a solid solution [76, 77]. As the rates of cascade mixing and RED become comparable, a non-equilibrium steady state solute distribution, typically characterized by clusters or nanoscale precipitates with stable size and number density, can develop [71, 78, 79]. Precipitate evolution models have predicted that in this steady state precipitation regime, large precipitates shrink and small precipitates grow as dose increases until a stable precipitate size is reached [68, 69]. Furthermore, nucleation of new precipitates is possible once local solute supersaturation is achieved due to the ejection of solute atoms from pre-existing precipitates to the matrix through dissolution [70].

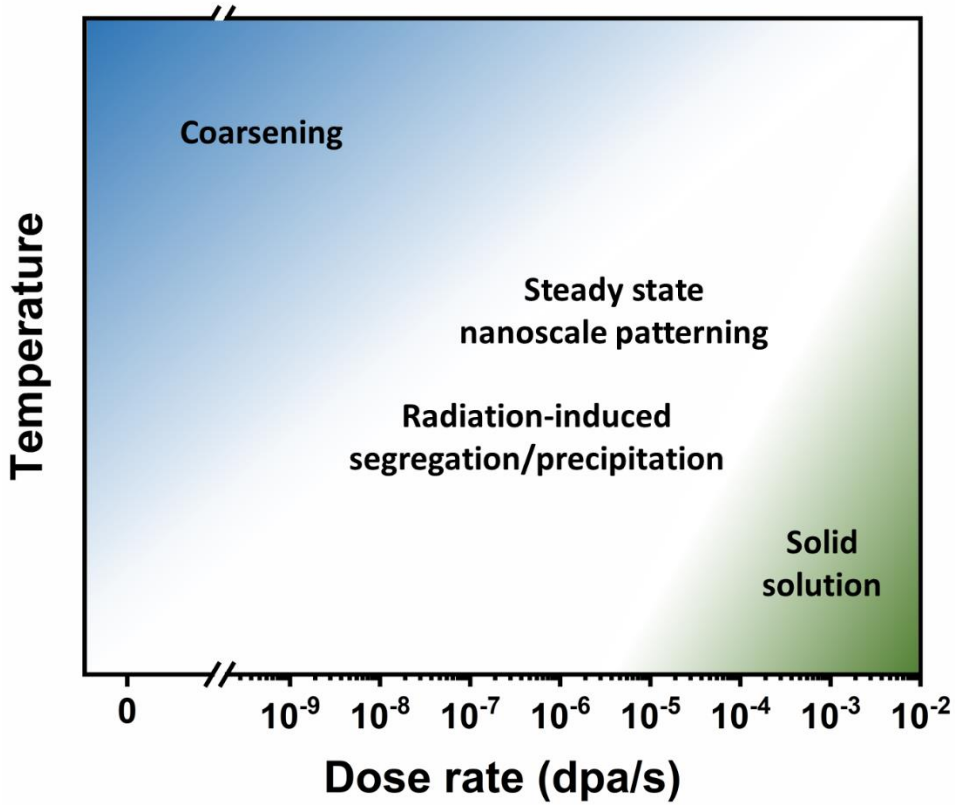

Figure 2.8. Schematic illustration of different precipitation regimes under irradiation.

2.3.3 Behavior of the γ′ phase under irradiation

The γ′ phase (FCC $L1_2$ structure) is a common strengthening phase that forms in Ni-based alloys containing Al and/or Ti during aging. However, γ′ precipitates can be unstable under certain irradiation conditions, which is one of the potential concerns when using precipitation-strengthened alloys in reactors. In Alloy X-750 samples that were removed from Canadian deuterium uranium (CANDU) reactors, the Ni_3(Al, Ti) γ′ precipitates had disordered after neutron irradiation (dose rate ~7×10^{-8} dpa/s) at 180 and 300 °C [80]. The disordering of γ′ precipitates during irradiation is dose rate and temperature dependent. In Nimonic PE16 alloy under ion irradiation at the dose rate of 10^{-3} dpa/s, γ′ precipitates dissolved and disordered below 350 °C [81]. In Alloy X-750, γ′ precipitates completely disordered at very low dose (0.06 dpa) under Kr ion

irradiation at the dose rate of 10^{-3} dpa/s between 60 and 400 °C. In contrast, at temperatures above 500 °C, γ′ precipitates were still present and did not disorder within the applied dose of 5.4 dpa [82]. The observations indicated a critical temperature above which the effect of diffusion is comparable to that of cascade mixing, and the precipitates remain present. The critical temperature of γ′ precipitates in Alloy X-750 is between 400 and 500 °C [82]. However, the critical temperature of a specific phase depends on alloy composition. Alloy X-750, for example, showed a higher γ′ disordering/dissolution critical temperature than Nimonic PE16 alloy [81, 82]. The author speculated that the higher concentration of slower diffuser, Ti, in the alloy caused reordering of the precipitates under irradiation more difficult, leading to a higher critical temperature [82]. The γ′ phase seemed to evolve toward steady state precipitate size and number density under ion irradiation at the dose rate of 10^{-2} dpa/s at 550 °C to ~10 dpa in Ni-13.5Al (at.%) [68]. The γ′ phase exhibited coarsening during irradiation, typically at elevated temperatures or under conditions of insignificant cascade mixing. In binary Ni-16Al (at.%) alloys, Ni_3Al γ′ precipitates coarsened at an enhanced rate under electron irradiation at 500 to 750 °C and the dose rate of ~10^{-3} dpa/s [72]. Even with cascade mixing effects under ion irradiation at the dose rate of ~3×10^{-3} dpa/s, Ni_3Al γ′ precipitates still displayed coarsening at 450 to 700 °C up to 12 dpa in Ni-12.8Al (at.%) [73]. Similarly, Ni_3Al γ′ precipitates coarsened under ion irradiation at the dose rate of ~3×10^{-3} dpa/s at 650 °C in Ni-6.35Al (wt.%) [83]. The conditions favoring the formation of γ′ phase under irradiation are summarized in **Figure 2.9**.

In terms of mechanism, disordering seemed to precede dissolution at low temperatures. In Alloy X-750, γ′ precipitates first disordered at 0.06 dpa and then dissolved at higher doses under ion irradiation between 60 and 400 °C at the dose rate of 10^{-3} dpa/s, as indicated by the blurred precipitate/matrix boundary imaged by energy-dispersive X-ray spectroscopy (EDS) mapping

under scanning transmission electron microscopy (STEM) mode [82]. Similarly, in another commercial Ni-based alloy, Rene N4, the large sized γ′ precipitates (side length ~450 nm) quickly disordered at 0.3 dpa under ion irradiation at the dose rate of ~5×10^{-3} dpa/s at room temperature, and then partially dissolved after irradiation up to 75 dpa [84]. In Nimonic PE16 alloy under ion irradiation at the dose rate of 10^{-3} dpa/s below 267 °C, γ′ precipitates first disordered and then dissolved [81]. On the other hand, disordering and dissolution occurred simultaneously at higher temperatures. In Nimonic PE16 alloy under ion irradiation at the dose rate of 10^{-3} dpa/s between 267 and 350 °C, γ′ precipitates disordered and dissolved simultaneously [81]. Simulations using molecular dynamics also captured this temperature dependence of γ′ precipitates dissolution process and were consistent with the experimental observations [85]. Moreover, the precipitate disordering/dissolution process depends on dose rate. Phase-field simulations suggested that in the case of high dose rates, precipitates quickly disordered and then dissolved, while disordering and dissolution proceeded at the same time at low dose rates [86]. Fine ordered precipitates could also form in the matrix at significantly low dose rates [86].

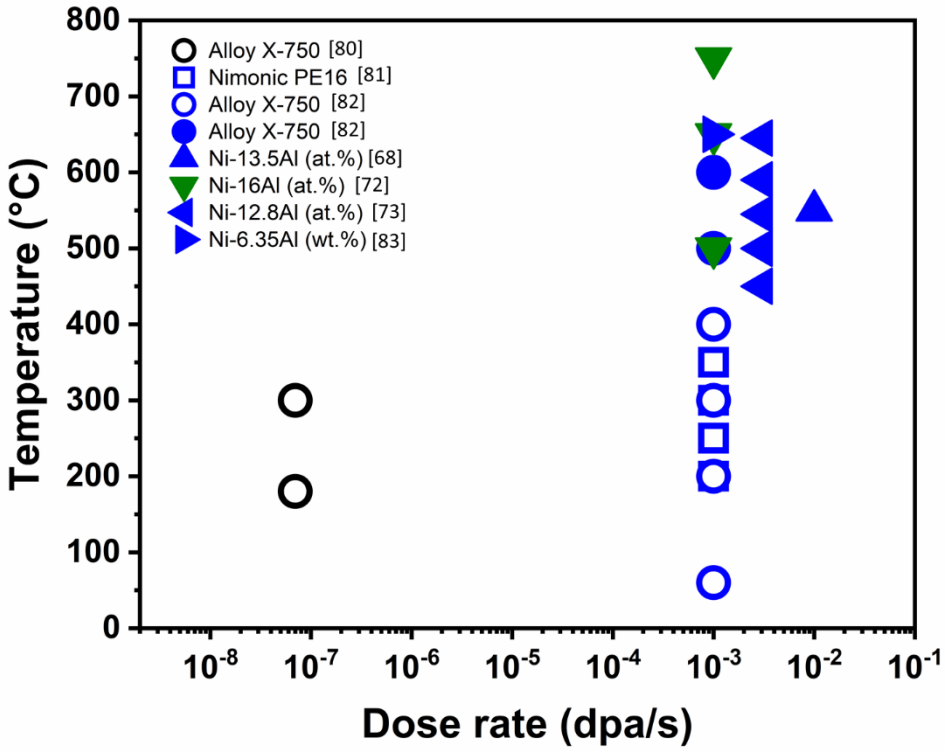

Figure 2.9. Temperature versus dose rate plot showing the conditions favoring the formation of γ′ phase in a variety of alloys under irradiation. Black, blue, and green indicate neutron, ion, and electron irradiations, respectively. Hollow symbols represent the γ′ precipitates dissolved or disordered, and solid symbols represent the γ′ precipitates remained present. (Data from [68, 72, 73, 80-83])

2.3.4 Behavior of the γ″ phase under irradiation

γ″ phase (BCT $D0_{22}$ structure) is another strengthening phase usually formed in Nb-containing commercial Ni-based alloys. Under irradiation, γ″ precipitates are also susceptible to disordering and dissolution. In Alloy 625 under neutron irradiation at ~370 °C, pre-existing γ″ precipitates partially dissolved, as indicated by the decrease in precipitate size [23, 87]. The temperature dependence of γ″ precipitation behavior under irradiation is consistent with the mechanism of the balance between diffusion and cascade mixing, as shown by electron-irradiated (dose rate ~10^{-3} dpa/s) Alloy 718 in which γ″ precipitates totally dissolved at room temperature,

partially dissolved (reduction in the intensity of γ″ superlattice diffraction spots) at 400 and 500 °C, and remained present (enhancement in the intensity of γ″ superlattice diffraction spots) at 650 °C [88]. At similar dose rate (~1.5×10^{-3} dpa/s), ion irradiation caused complete dissolution of γ″ phase in Alloy 718 at 200 °C within 1 dpa [76], possibly because of the strong cascade mixing effect.

In alloys containing both γ′ and γ″ phases, γ′ precipitates seem to stay present longer than γ″ precipitates. In Alloy 718 under neutron irradiation at 288 °C, γ″ precipitates dissolved after 2.5 dpa while γ′ precipitates remained present but spatially redistributed [89]. Similarly, in Alloy 706 under neutron irradiation, pre-existing γ″ precipitates dissolved at 400 to 500 °C and coarsened at 650 °C, while pre-existing γ′ precipitates remained present from 400 to 650 °C. In solutionized Alloy 706 under neutron irradiation, only γ′ precipitated at 400 to 500 °C, while both phases precipitated from the matrix at 650 °C [90].

2.3.5 Behavior of the Pt_2Mo-type ordered phase under irradiation

The embrittling Pt_2Mo-type ordered phase can form in Ni-Cr based alloys, such as Alloy 625 and Alloy 690 during thermal aging with slow ordering kinetics at relevant reactor working temperatures, as already mentioned in **2.2** and in Ref. [38]. Under irradiation, the formation rate of this phase is accelerated. In binary Ni-33Cr (at.%) alloy, and ternary Ni-34Cr-5Fe and Ni-31Cr-10Fe (at.%) alloys, the Pt_2Mo-type ordered phase formed under electron irradiation at 300 to 500 °C within several minutes, suggesting a radiation-enhanced mechanism [91]. Similarly, this phase formed in Alloy 625 under neutron irradiation at ~370 °C within ~1000 h, but did not precipitate under thermal aging at the same temperature for the same duration [23, 87, 92]. Proton irradiation

at 360 °C also caused the formation of Pt_2Mo-type ordered phase in several commercial Ni-based alloys, including Alloy 625, Alloy 625 Plus, and Alloy 690. However, this ordered phase was not observed in Alloy 718 and Alloy 706, which is possibly attributed to the higher Fe content that tends to decrease the volume fraction of this ordered phase and stabilize the disordered FCC matrix [93].

2.3.6 Cavity evolution

The bombardment of energetic particles on the crystal lattice during radiation damage events causes a supersaturation of point defects. The supersaturation of vacancies is the main driving force for cavity nucleation. Once the number of vacancies in a vacancy cluster reaches a critical value, the vacancy cluster will be stable to grow into a cavity [94]. The preferential attraction of interstitials to dislocations (dislocation bias) can lead to extra vacancies migrate to cavities, which is the fundamental cause of cavity growth [95, 96]. Significant number and continued growth of cavities can lead to volumetric swelling and dimensional instability of materials [97].

Typically, as dose increases, the formation of other types of defects provides additional sinks for vacancies, leading to the decrease in vacancy supersaturation and cavity nucleation rate [98]. Excessive vacancies created at this stage would reach the existing cavities and result in cavity growth rather than nucleation of new cavities. The swelling evolution as a function of dose has been described by a rate theory model [99]. The relative impact of dislocation sink strength and cavity sink strength determines the swelling evolution behavior. Generally, swelling gradually increases as dose increases, and reaches a steady state swelling rate. As cavities become dominant sinks, where both vacancies and interstitials are captured by cavities, swelling slows down due to

the little net absorption of vacancies by cavities. At even higher doses, where cavities are significantly large and numerous, cavity coalescence would occur [100-102].

Cavity formation and evolution under irradiations have been observed in Ni and Ni alloys. Cavity density in Ni saturates within 1 dpa under neutron irradiations at temperatures around 450 °C [103]. Cavity formation is temperature dependent. The temperature regime for cavity formation in Ni under neutron irradiation lies within ~250 to 750 °C (**Figure 2.10**) [104]. The bell-shaped curve in **Figure 2.10** can be rationalized by the simple cavity nucleation and growth mechanism. At low temperatures, vacancies are immobile and more likely to recombine with interstitials, resulting in limited cavity growth. At high temperatures, thermal emission of vacancies by cavities is non-negligible. Also, vacancy supersaturation is suppressed as defect concentrations are close to thermal equilibrium, leading to low cavity nucleation rates [105]. Hence, the cavity number density typically decreases with increasing temperature. The cavity number densities in irradiated Ni and Ni-based alloys as a function of irradiation temperature are summarized in **Figure 2.11**.

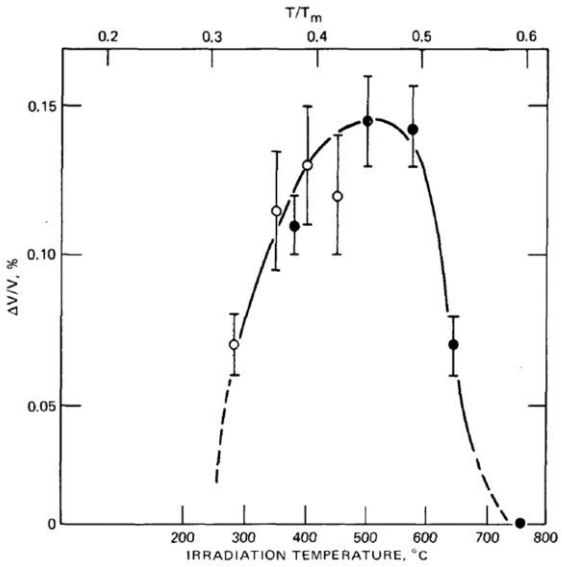

Figure 2.10. Temperature dependence of swelling in pure Ni after neutron irradiation to a

fluence of 5×10^{19} n/cm^2. (Adapted from [104])

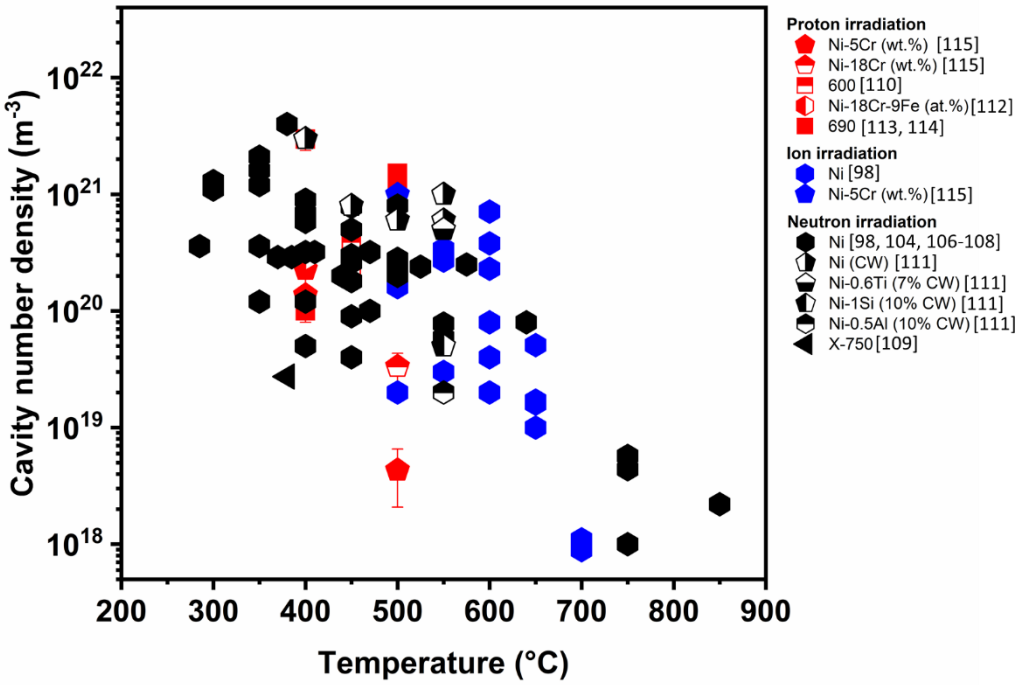

Figure 2.11. Cavity number densities in Ni-based alloys as a function of temperature. (Data from [98, 104, 106-115])

A temperature shift for cavity swelling is observed when comparing the neutron irradiated and ion irradiated Ni data, indicating a dose rate dependence of cavity swelling [98]. As dose rate increases, equivalent cavity swelling requires higher temperatures. At a given temperature, the mutual recombination rate of vacancies and interstitials increases when increasing dose rate. Thus, the net absorption of vacancies by cavities is reduced, leading to a depression of cavity swelling. By increasing the temperature, the migration velocity of defects to sinks increases. Therefore, more vacancies can reach to cavities instead of recombining in the matrix [116]. The temperature shift that keeps the swelling rate invariant in the defect recombination dominated regime [117] is:

$$T_2 - T_1 = \frac{\frac{kT_1^2}{E_v^m + 2E_v^f} \ln\left(\frac{K_{02}}{K_{01}}\right)}{1 - \frac{kT_1}{E_v^m + 2E_v^f} \ln\left(\frac{K_{02}}{K_{01}}\right)}$$

where T is temperature, k is Boltzmann constant, K_0 is dose rate, E_v^m is vacancy migration energy, and E_v^f is vacancy formation energy. Using E_v^m = 1.08 eV in Ni [118], E_v^f = 1.63 eV in Ni [118], and assuming the peak swelling in Ni under neutron irradiation at the dose rate of 10^{-7} dpa/s is ~500 °C [104] (**Figure 2.10**), the temperature shift at the dose rate of 10^{-3} dpa/s is calculated to be ~130 °C. The experimentally observed temperature shift of peak swelling was ~200 °C in Ni when comparing ion-irradiated (at ~3 ×10^3 dpa/s) results with neutron-irradiated (at ~10^{-7} dpa/s) results [98].

Cavity number density seems to be higher in neutron-irradiated Ni than in ion-irradiated Ni [98]. Specimens with pre-injection of He also exhibit higher cavity number density [98, 119]. These were attributed to the effect of He on cavity nucleation. He can be generated in Ni-containing alloys under neutron irradiation due to the two-step ^{58}Ni (n, γ) ^{59}Ni (n, α) ^{56}Fe transmutation reactions [120]. The produced He can reduce the cavity nucleation barrier and promote the nucleation rate [121].

Alloy composition also appears to affect cavity evolution. Comparing different commercial alloys, a minimum in cavity swelling was observed in alloys with Ni content at ~40 to 50 wt.% [122]. In binary Ni alloys, the average cavity size is smaller in alloys containing larger-sized solute atoms [123]. This was explained by the stronger binding energy of large-sized solute atoms with vacancies, which reduces the vacancy mobility. Similarly, cavities are in smaller sizes and higher number densities in commercial alloys with minor addition (~0.4 at.%) of larger-sized solute atoms [124].

2.3.7 Dislocation loop evolution

Another common type of defects formed during irradiation is dislocation loop. Typically, once interstitials that formed in a damage cascade condense on certain crystallographic planes, faulted dislocation loops form [125]. The formation of dislocation loops usually causes hardening of irradiated materials [126]. In FCC materials, both faulted loops with Burgers vector of 1/3<1 1 1>, and perfect loops with Burgers vector of 1/2<1 1 0> can be observed [127].

The evolution of dislocation structures as a function of dose can be categorized into several different temperature regimes [128, 129]. For neutron-irradiated austenitic steels, black spots (very small defect clusters) dominate the microstructures at temperatures below 300 °C. Their number density quickly reaches to a steady state value within 1 dpa. Near 300 °C, dislocation structure is mostly dominated by faulted dislocation loops. In the temperature regime of 300 to 700 °C, dislocation structure primarily consists of faulted loops and network dislocations. Faulted dislocation loop number density decreases with increasing temperature, mainly due to the un-faulting of large-sized loops that interact with other dislocations. A steady state dislocation number density can establish around 10 dpa, depending on the interaction of defects with other microstructural components formed during irradiation, such as precipitates and cavities. Similarly, for Ni-based alloys, faulted dislocation loops and network dislocations were observed below 700 °C. The dislocation loop densities in irradiated Ni and several Ni-based alloys as a function of irradiation temperature are summarized in **Figure 2.12**.

The dislocation structures developed under irradiation seem to be altered by solute atoms. Dislocation loops are in smaller sizes and higher number densities in binary Ni alloys containing

larger solute atoms, which is mainly attributed to the trapping of interstitials by large-sized solute atoms, leading to a higher migration barrier for interstitials [123].

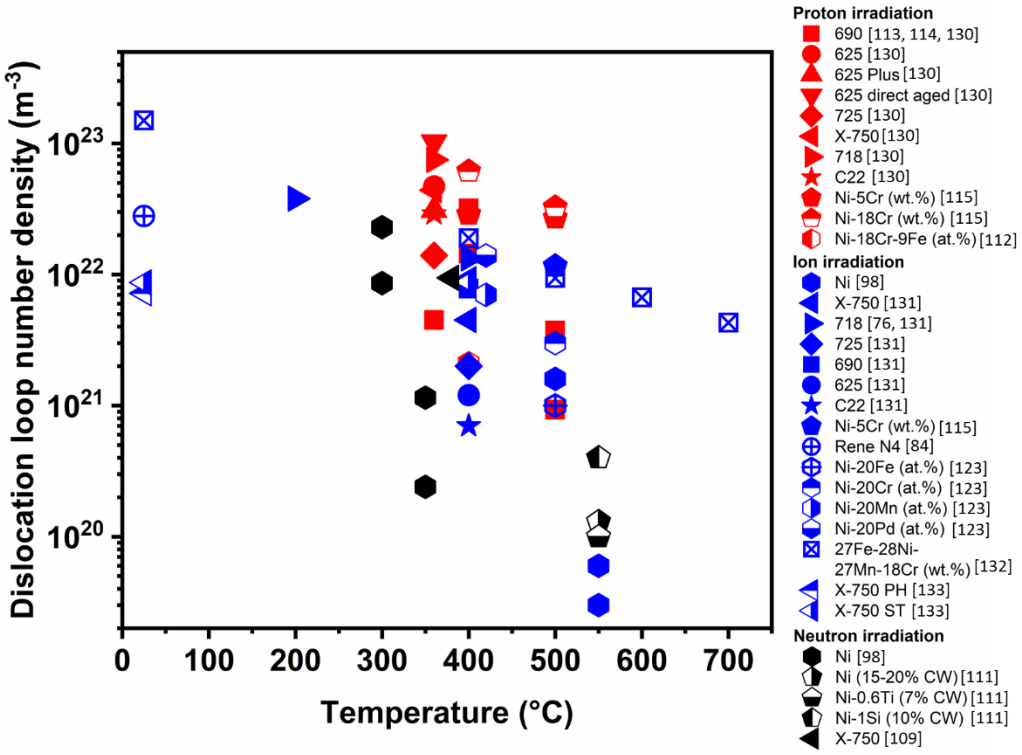

Figure 2.12. Dislocation loop number densities in Ni-based alloys as a function of temperature for a range of irradiation conditions. (Data from [76, 84, 98, 109, 111-115, 123, 130-133])

2.4 Summary and hypotheses

Previous research reviewed in this chapter suggested a strong influence of irradiation conditions (dose, dose rate, and temperature etc.) on the precipitation behavior as well as cavity and dislocation loop evolutions in Ni-based alloys. However, the different alloy compositions and consequently phases forming, and different precipitation behaviors imply that an alloy's

microstructural response has its unique dependence on irradiation conditions. Based on the findings in the literature, the following hypotheses are formulated:

1. The Pt_2Mo-type ordered phase will form in Alloy 625, Alloy 625 Plus, and Alloy 690 under proton irradiation at 300 to 400 °C. Ion irradiation at higher dose rates will prevent it from forming due to higher cascade mixing rates.

2. Since more long range diffusion is needed for the precipitation of γ″ phase, whose composition largely deviates from the matrix composition, unlike the Pt_2Mo-type phase, γ″ phase is more easily destroyed by cascade mixing under irradiation than the Pt_2Mo-type phase.

3. Alloy 625 and Alloy 625 Plus will exhibit smaller and more cavities and dislocation loops than Alloy 690 under irradiation due to higher larges-sized solute concentrations, such as Mo and Nb.

4. The phases that form in Alloy 625, Alloy 625 Plus, and Alloy 690 (γ″ and Pt_2Mo-type phases) will remain present and even coarsen under neutron irradiation.

Since information on the precipitation behavior of Alloy 625 Plus under both thermal aging and irradiation is not available in the open literature, the next chapter first focuses on establishing the aging behavior of Alloy 625 Plus and comparing it to that of Alloy 625. The following chapters analyze irradiated microstructures and comparisons among the three alloys.

Chapter 3

Thermal Aging Behavior of Alloy 625 and Alloy 625 Plus

3.1 Introduction

Ni-based superalloys are widely used in power plants due to their good high-temperature strength and corrosion resistance, achieved via alloying [30, 134]. Cr and Mo are typically added for corrosion resistance [135, 136], Fe reduces cost [136], Mo and Nb are solid-solution strengtheners [137], and Nb, Ti, and Al facilitate precipitation hardening [137]. Among commercial Ni-based alloys, Alloy 625 was originally designed as a solid-solution strengthened and corrosion resistant steam-line piping material mainly through its high Cr (~25 at.%) and Mo (~6 at.%) concentrations [27]. It was also found to be precipitation-hardened by the BCT Ni_3(Nb, Ti, Al) γ″ phase ($D0_{22}$ structure) after thermal aging within 550 to 750 °C [25, 34]. The limited strength of Alloy 625 is an issue. Hardening via precipitation requires aging times that are too long for an industrial process and cold working is limited to small enough parts [42, 138]. In contrast, Alloy 718 that is used in gas turbine engines [139, 140], can be age-hardened via the precipitation of both the BCT Ni_3(Nb, Ti, Al) γ″ phase and the Ni_3(Al, Ti, Nb) FCC γ′ phase ($L1_2$ structure) [141]. Alloy 718 exhibits better strength but insufficient corrosion resistance against the environment containing chloride and sulfide at high pressures and temperatures up to 230 °C [42]. Therefore, a modified version of Alloy 625, named Alloy 625 Plus, was developed to combine the corrosion resistance of Alloy 625 and age-hardening capability of Alloy 718 [42]. Alloy 625 Plus can be age-hardened to yield strengths above 800 MPa without cold-working [142]. Compared to

Alloy 625, Alloy 625 Plus has lower Ni, Cr, and Mo concentrations yet Ti and Fe concentrations are slightly increased (**Table 2.1**). The higher Ti concentration in Alloy 625 Plus is expected to yield higher strength than Alloy 625. However, there is no available data enabling direct evidence or comparison. The reported mechanical properties of Alloy 625, Alloy 625 Plus, and Alloy 718 were measured after different aging conditions [42, 143]. Moreover, the microstructure – property relationship for Alloy 625 Plus is not well characterized. Vander *et al.* found only the γ″ precipitates as strengthening phase after thermal aging at 732 to 802 °C for 20 to 1800 minutes [43]. Frank *et al.* investigated its mechanical properties after various heat treatments without linking the observations to the alloy microstructures [142]. Hence, to provide a more complete description of the evolution of the microstructures, this chapter focuses on characterizing and comparing the precipitation behavior of Alloy 625 and Alloy 625 Plus under the same aging conditions (solution treatment at 1100 °C for 1 h followed by thermal aging at 650 °C up to 1000 h), and linking them to possible differences in the compositions of Alloy 625 and Alloy 625 Plus.

3.2 Materials and methods

Alloy 625 (heat number: 602051) and Alloy 625 Plus (heat number: 215846) were provided by Carpenter Technology Corporation. The chemical compositions measured from atom probe tomography (APT) are listed in **Table 3.1**. Both alloys were solution treated at 1100 °C for 1 h, followed by water quenching, and aged at 650 °C for 8, 25, and 100 h in order to investigate the evolution of γ″ precipitates. Longer aging times (300, 400, and 1000 h) were applied to Alloy 625 Plus in order to capture the precipitation of the γ′ phase. All samples were ground using silicon carbide paper and polished using 1 μm diamond suspension solution, followed by further surface preparation methods including polishing using SiO_2 colloidal suspension or electropolishing at 30

V using a 10% perchloric acid + 90% methanol electrolyte at -30 °C.

Table 3.1. APT measured chemical compositions (at.%) of Alloy 625 and Alloy 625 Plus.

Alloy	Ni	Cr	Mo	Fe	Nb	Ti	Al	Si	Co	Mn	P	S	C	Ta
625	61.6	26.1	5.48	3.77	2.16	0.29	0.33	0.15	0.01	0.06	<0.01	-	0.03	-
625 Plus	61.1	23.9	5.12	5.51	2.18	1.59	0.37	0.09	0.01	0.02	-	-	0.03	-

A background subtraction was applied and peak decomposition of Ti and Cr, Cr and Fe, Fe and Ni, Ni and Mo, and Ni and Nb was performed based on isotopic natural abundances.

APT and transmission electron microscopy (TEM) specimens were prepared using a standard lift-out and Ga ion beam thinning process on both FEI Nova 200 and FEI Helios 650 Nanolab dual scanning electron microscope (SEM)/focused ion beam (FIB) instruments. TEM specimens were characterized on a JEOL 3011 transmission electron microscope. APT data were collected on CAMECA LEAP 4000X HR and 5000 XR instruments operated in laser mode using a pulse energy of 50 pJ, 200 kHz pulse rate, and a target detection rate of 0.5% at 50 K, in order to obtain large datasets and avoid early specimen fracture. APT data were analyzed using the IVAS 3.8.2 software, and the radius evolution of the reconstructed dataset was based on voltage evolution using the evaporation field of Ni (35 nm/V [144]). The reconstruction parameters (image compression factor and field factor k_f) were adjusted to minimize the matrix atomic density variations along the longitudinal and radial directions. The image compression factor and k_f value ranged between 1.3 and 1.8, and between 2.9 and 3.5, respectively.

The γ″ precipitates were delineated using Cr iso-concentration surfaces. The concentration

gradient across the matrix/precipitates interface was fitted using error function:

$$C_i = A\,\mathrm{erf}(ax - b) + C_{threshold}$$

where C_i is the concentration of element i, A, a, and b are fitting constants. erf is the error function defined as $\mathrm{erf}(z) = \frac{2}{\sqrt{\pi}}\int_0^z e^{-t^2}dt$. $C_{threshold}$ is the inflection point and its value is defined here as the concentration threshold used to create the iso-concentration surfaces (Cr = 16 at.% in this study). In the case of Alloy 625 Plus where both γ″ and γ′ precipitates formed, Al iso-concentration surfaces (5 at.%) were used to define the γ′ precipitates.

The precipitate number density was calculated from APT results using the number of precipitates divided by the total volume of the dataset. The contribution of precipitates partially contained within the APT dataset, was set at ½ and the γ″ precipitates that appeared to have coalesced were divided into multiple particles. The volume of the dataset was calculated using the atomic density of Alloy 625 (8.4 g/cm^3) and detector efficiencies of 36% for CAMECA LEAP 4000X HR or 52% for CAMECA LEAP 5000 XR instrument. The volume-equivalent precipitate radius was calculated from precipitate volumes defined by the iso-concentration surfaces, and the radius measurements included full precipitates only. The precipitate volume fractions were calculated using the ratio between the volume of precipitates and the whole dataset, and the concentration balance of elements following the relation of $C_i = C_{i,\gamma''}V_{\gamma''} + C_{i,\gamma}(1 - V_{\gamma''})$, where C_i is the concentration of i element in the alloy, $C_{i,\gamma''}$ is the concentration of i element in the γ″ phase, $C_{i,\gamma}$ is the concentration of i element in the γ matrix, and $V_{\gamma''}$ is the volume fraction of the γ″ phase. The two methods for volume fraction calculation showed consistent results.

Compositions of γ matrix, γ″, and γ′ precipitates were calculated within the portions of proximity histograms [145] (proxigrams) where the solute concentrations were spatially uniform. For Alloy 625, more than 30 γ″ precipitates were measured for each aging condition, and for Alloy

625 Plus, more than 90 γ″ precipitates were measured for each aging condition. Due to the low number density of γ′ precipitates in Alloy 625 Plus, only 3 to 10 precipitates were measured for each aging condition. In the case of Alloy 625 Plus, Cr iso-concentration surfaces that contained both γ″ and γ′ precipitates were removed when calculating the γ″ precipitate compositions. A background subtraction was applied and peak decomposition of the Ti and Cr, Cr and Fe, Fe and Ni, Ni and Mo, and Ni and Nb isotope overlap was performed using isotopic natural abundances for all the composition measurements.

3.3 Results

3.3.1 Precipitation behavior of Alloy 625

APT reconstructions collected after increasing aging time highlight the development of γ″ precipitates in Alloy 625 during aging at 650 °C, as shown in **Figure 3.1**. After aging for 8 h, nanoscale precipitates (revealed by the depletion of Cr in **Figure 3.1b**) were observed and their sizes increased with increasing aging time. After aging for 25 h, it became clear that Ni, Nb, and Ti partitioned to the precipitates, whereas Cr and Fe partitioned to the γ matrix (**Figure 3.1c**). Mo appeared neutral with comparable concentrations in both γ and γ″ phases, and Al slightly partitioned to the γ″ phase (**Figure 3.2**). The compositions of γ matrix and precipitates as a function of aging time are listed in **Table 3.2**. The measured precipitate compositions are consistent with the stoichiometry of the Ni_3(Nb, Mo, Ti, Al) γ″ phase. The presence of γ″ precipitates was also confirmed by the superlattice diffraction spots at {1 0 0}, {1 1/2 0}, and {1 1 0} positions in the <0 0 1>-zone TEM diffraction pattern (**Figure 3.3a**), which are consistent with the $D0_{22}$ structure [29]. The sizes of γ″ precipitates in TEM dark-field (TEM-DF) image (**Figure 3.3b**) are consistent

with the observation in APT results.

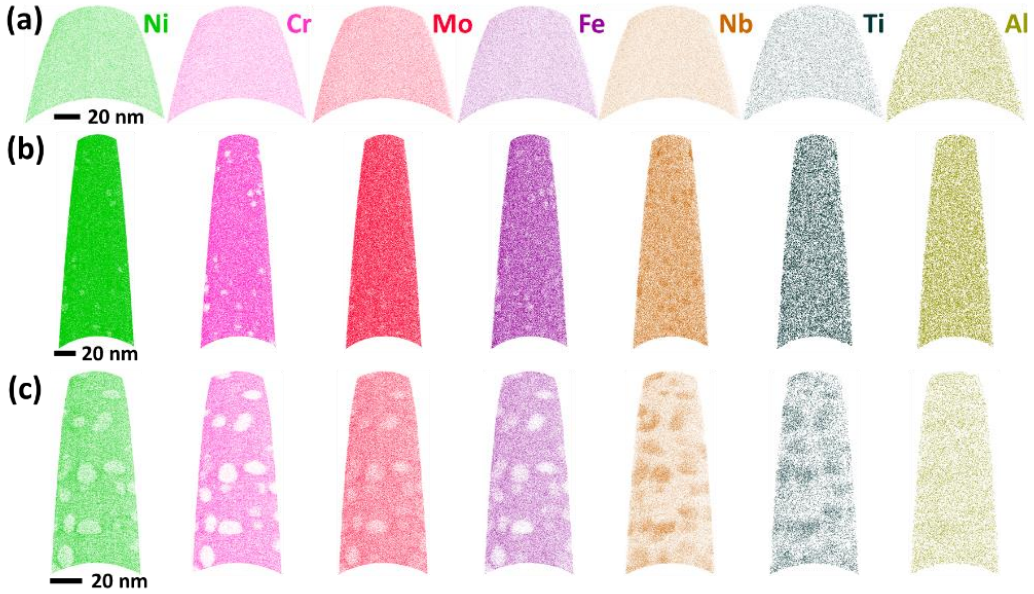

Figure 3.1. APT ion maps of Alloy 625 after (a) solution treatment and thermal aging at 650 °C aging for (b) 8 h and (c) 25 h. The thicknesses of ion map slices are 1, 2, 10, 10, 20, 20, and 20 nm for Ni, Cr, Mo, Fe, Nb, Ti, and Al, respectively, and the same thicknesses will be used in this chapter.

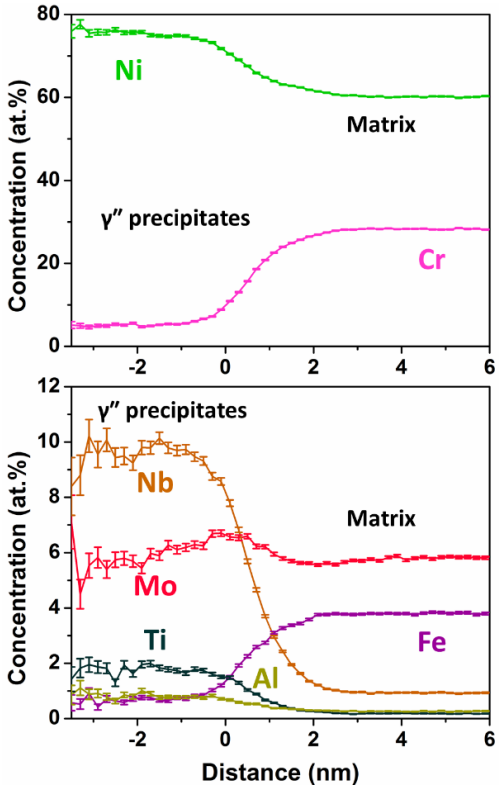

Figure 3.2. Proximity histograms, generated from Cr = 16 at.% iso-concentration surfaces, of γ″ precipitates in Alloy 625 after 650 °C aging for 25 h. The error bars are based on the counting error $\sqrt{c_i(1-c_i)/N_{bin}}$, where c_i is the atomic fraction of element i and N_{bin} is the total number of atoms in the bin.

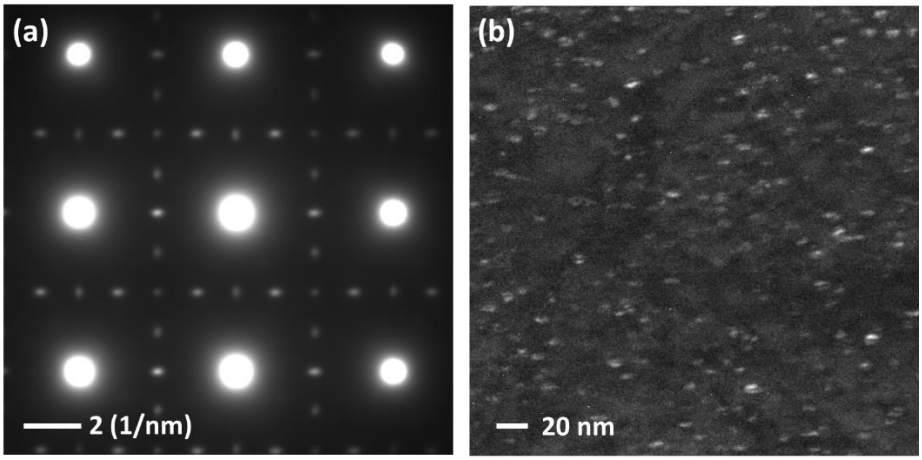

Figure 3.3. (a) <0 0 1>-zone TEM diffraction pattern showing the corresponding superlattice diffraction spots of γ″ precipitates, and (b) TEM-DF image using (1 0 0) superlattice diffraction spot to show γ″ precipitates in Alloy 625 after thermal aging at 650 °C for 25 h.

Table 3.2. Chemical compositions (at.%) of the γ matrix and γ″ precipitates in Alloy 625.

Phase	Aging time (h)	Ni	Cr	Mo	Fe	Nb	Ti	Al
γ matrix	8	59.9 ± 0.02	28.5 ± 0.02	5.19 ± 0.01	3.77 ± 0.01	1.85 ± 0.01	0.25 ± 0.01	0.31 ± 0.01
	25	58.5 ± 0.03	30.4 ± 0.03	5.35 ± 0.01	4.00 ± 0.01	1.16 ± 0.01	0.14 ± 0.01	0.24 ± 0.01
	100	57.8 ± 0.03	29.9 ± 0.02	5.88 ± 0.01	3.96 ± 0.01	1.48 ± 0.01	0.15 ± 0.01	0.09 ± 0.01
γ″ precipitates	8	73.7 ± 0.90	4.77 ± 0.39	6.24 ± 0.47	0.59 ± 0.18	12.3 ± 0.73	1.16 ± 0.23	0.79 ± 0.17
	25	74.3 ± 0.23	3.65 ± 0.10	5.27 ± 0.12	0.60 ± 0.06	13.2 ± 0.20	1.87 ± 0.07	0.89 ± 0.04
	100	73.0 ± 0.29	3.67 ± 0.13	6.07 ± 0.15	0.75 ± 0.08	13.5 ± 0.25	1.52 ± 0.08	0.55 ± 0.05

3.3.2 Precipitation behavior of Alloy 625 Plus

The evolution of γ″ and γ′ precipitates in Alloy 625 Plus during aging at 650 °C was characterized by APT, as illustrated in **Figure 3.4**. The formation of γ″ precipitates was first captured after aging at 650 °C for 8 h, as shown by the very faint depletion of Cr in **Figure 3.4b**, and the γ″ precipitates became larger with increasing aging time. For aging periods shorter than 300 h, only γ″ precipitates were observed, as shown in **Figure 3.4a-d**. However, as aging time exceeded 300 h, Ti and Al-rich γ′ precipitates were observed with a much lower number density compared to γ″ precipitates (**Figure 3.4e-g**). For both γ″ and γ′ phases, Ni, Nb, and Ti partitioned to the precipitates, while Cr and Fe partitioned to the γ matrix. As opposed to the γ″ phase that exhibited slight Al enrichment and no Mo partitioning, Al strongly partitioned to the γ′ phase, while Mo was significantly depleted (**Figure 3.5**). The compositions of the γ matrix, γ″, and γ′ precipitates as a function of aging time are listed in **Table 3.3**. The measured matrix compositions became stable after 300-h aging. The measured γ″ composition was close to Ni_3(Nb, Ti, Mo, Al), and the γ′ composition was measured to be $Ni_3(Ti_{0.4}Al_{0.4}Nb_{0.2})$.

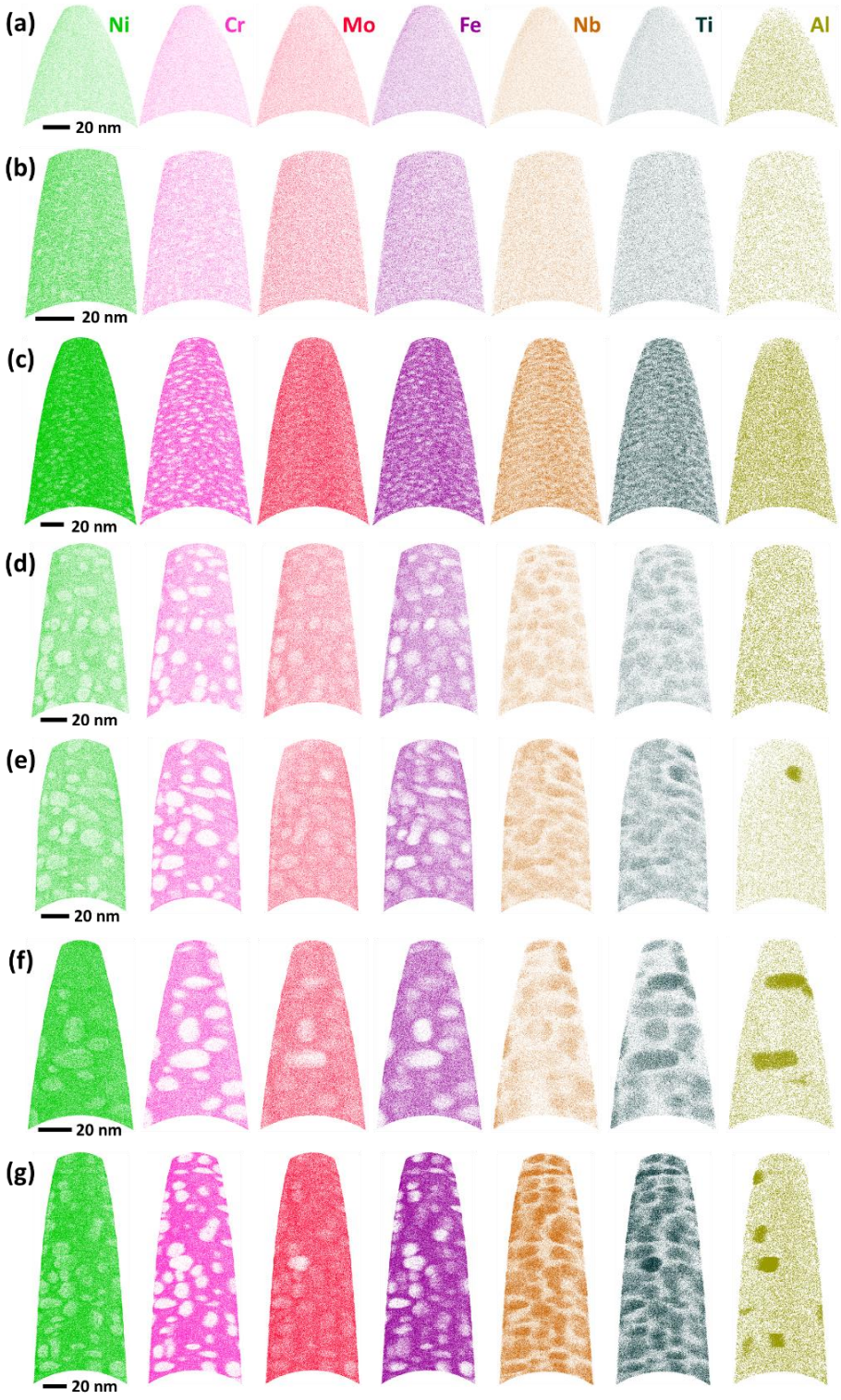

Figure 3.4. APT ion maps of Alloy 625 Plus after (a) solution treatment and thermal aging at 650 °C aging for (b) 8 h, (c) 25 h, (d) 100 h, (e) 300 h, (f) 400 h, and (g) 1000 h, respectively.

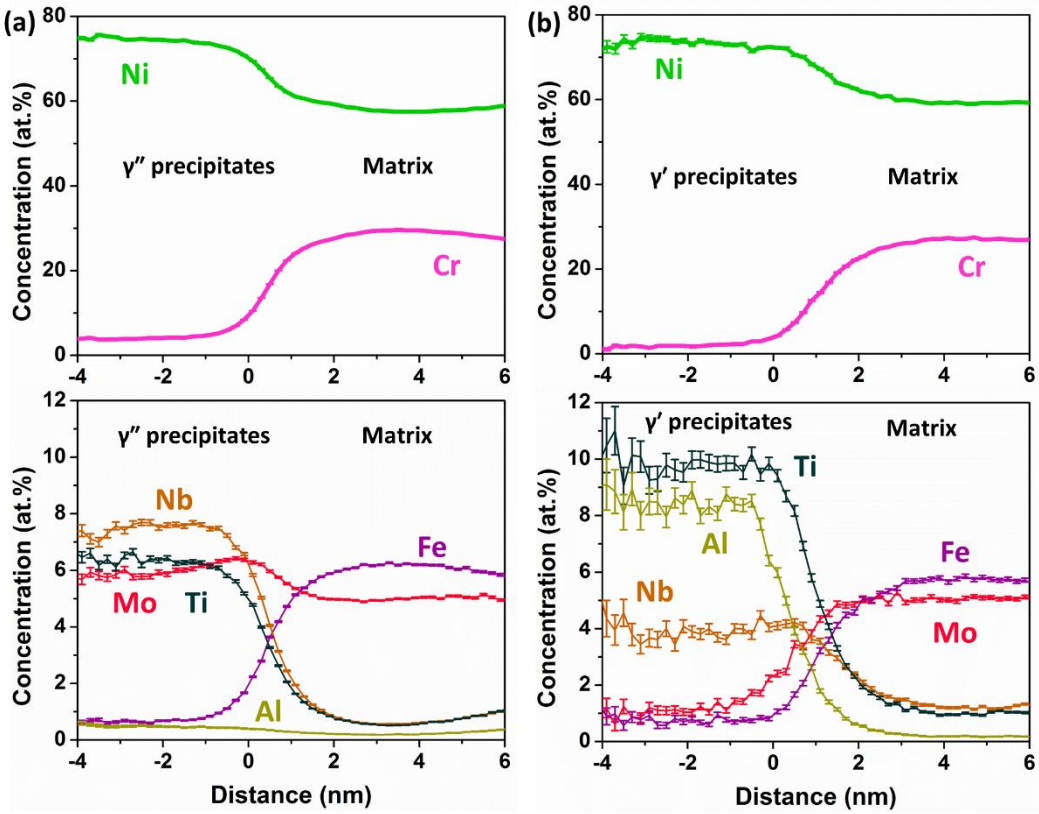

Figure 3.5. (a) Proximity histograms, generated from Cr = 16 at.% iso-concentration surfaces, of γ″ precipitates in Alloy 625 Plus after 650 °C aging for 1000 h. (b) Proximity histograms, generated from Al = 5 at.% iso-concentration surfaces, of γ′ precipitates in Alloy 625 Plus after 650 °C aging for 1000 h.

Table 3.3. Chemical compositions (at.%) of the γ matrix, γ″, and γ′ precipitates in Alloy 625 Plus.

Phase	Aging time (h)	Ni	Cr	Mo	Fe	Nb	Ti	Al
	25	57.6 ± 0.02	29.1 ± 0.02	4.71 ± 0.01	6.08 ± 0.01	1.10 ± 0.01	0.84 ± 0.01	0.37 ± 0.01
	100	57.7 ± 0.03	29.5 ± 0.03	4.92 ± 0.01	6.24 ± 0.02	0.72 ± 0.01	0.54 ± 0.01	0.24 ± 0.01
γ matrix	300	55.6 ± 0.03	31.4 ± 0.03	4.84 ± 0.01	6.59 ± 0.02	0.67 ± 0.01	0.48 ± 0.01	0.18 ± 0.01
	400	56.1 ± 0.04	31.0 ± 0.03	4.90 ± 0.02	6.48 ± 0.02	0.61 ± 0.01	0.43 ± 0.01	0.22 ± 0.01
	1000	55.9 ± 0.02	31.1 ± 0.02	4.89 ± 0.01	6.67 ± 0.01	0.61 ± 0.01	0.43 ± 0.01	0.14 ± 0.01
γ″	25	74.7 ± 0.92	3.16 ± 0.37	4.94 ± 0.46	0.79 ± 0.21	9.42 ± 0.71	5.99 ± 0.53	0.70 ± 0.16
precipitates	100	74.9 ± 0.21	2.38 ± 0.06	5.51 ± 0.10	0.61 ± 0.06	9.44 ± 0.13	6.41 ± 0.10	0.46 ± 0.03

	300	74.9 ± 0.26	1.79 ± 0.07	5.61 ± 0.13	0.67 ± 0.07	9.34 ± 0.18	6.96 ± 0.14	0.48 ± 0.01
	400	74.8 ± 0.16	2.04 ± 0.05	5.45 ± 0.08	0.63 ± 0.04	9.76 ± 0.12	6.59 ± 0.09	0.49 ± 0.03
	1000	74.7 ± 0.10	1.96 ± 0.03	5.44 ± 0.05	0.60 ± 0.02	9.65 ± 0.06	6.88 ± 0.05	0.51 ± 0.01
γ′ precipitates	300	70.6 ± 0.63	0.93 ± 0.12	0.63 ± 0.12	0.90 ± 0.12	5.42 ± 0.38	10.5 ± 0.41	10.5 ± 0.39
	400	71.1 ± 0.71	0.63 ± 0.11	0.96 ± 0.16	0.72 ± 0.15	4.60 ± 0.38	11.1 ± 0.45	10.5 ± 0.40
	1000	71.5 ± 0.23	0.78 ± 0.04	0.80 ± 0.05	1.01 ± 0.05	4.82 ± 0.13	10.5 ± 0.16	10.1 ± 0.16

The γ″ phase precipitated with a disk shape, while γ′ precipitates formed with a cuboid morphology and faces orthogonal to the <1 0 0> directions of the FCC γ matrix (**Figure 3.6**). All the observed γ′ precipitates were attached to the flat surface of the disk-shaped γ″ precipitates (**Figure 3.6**). The most common combined precipitate configuration was one γ′ precipitate attached to a γ″ precipitate. These γ″-γ′ duplets were more frequently observed than the other configuration, a sandwich structure composed of two γ″ precipitates on opposite faces of a γ′ precipitate. The TEM bright-field (TEM-BF) image displayed comparable sizes of precipitates as observed in APT results after 1000-h aging (**Figure 3.7a**), and the <0 0 1>-TEM diffraction pattern confirmed the presence of precipitates (**Figure 3.7b**). The TEM-DF images illustrated the different variants of γ″ precipitates [141] (**Figure 3.7c**, **d**). The morphology of γ″-γ′-γ″ triplets, as highlighted by the yellow circle in **Figure 3.7c**, was also observed in TEM-DF image taken by selecting (0 1 0) superlattice diffraction spot.

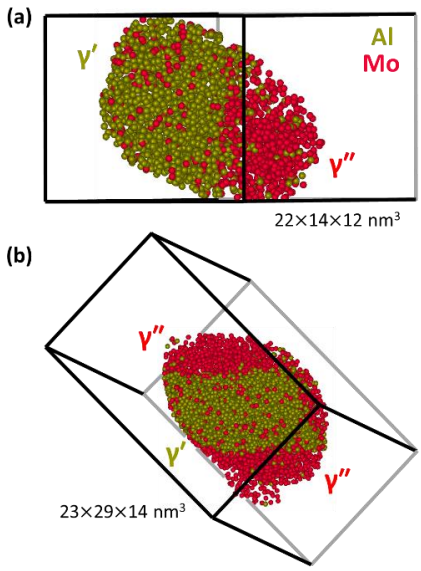

Figure 3.6. APT ion maps showing (a) a γ″-γ′ duplet and (b) a γ″-γ′-γ″ triplet. Only Al and Mo were displayed for clarity.

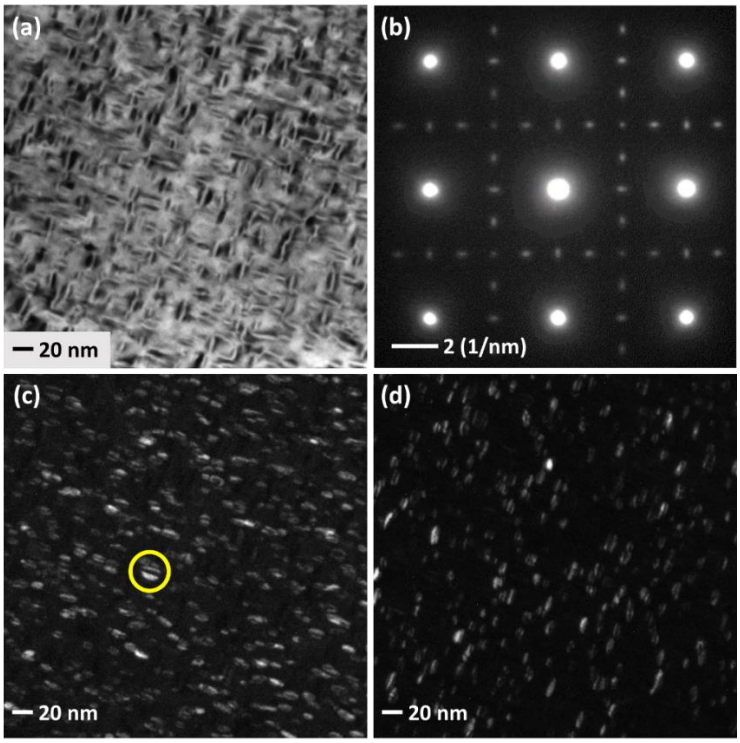

Figure 3.7. (a) TEM-BF image showing γ″ and γ′ precipitates in Alloy 625 Plus after thermal aging for 1000 h and corresponding (b) <0 0 1>-zone TEM diffraction pattern. (c) and (d) TEM-DF images taken using the (0 1 0), and (1 0 0) superlattice diffraction spot, respectively. The γ″-γ′-γ″ triplet structure is highlighted by the yellow circle in (c).

3.4 Discussion

The aging behavior at 650 °C of Alloy 625 and Alloy 625 Plus revealed significant differences in terms of the nature of precipitating phases, precipitate number densities, sizes, and coarsening rates. In addition to the γ″ phase forming in both Alloy 625 and Alloy 625 Plus, the γ′ phase also formed in Alloy 625 Plus. The phase equilibrium predictions using Thermocalc (the CALPHAD method) with the Ni-based Superalloys database version 8.1 (TCNI8), are qualitatively consistent with our observations, as shown in **Figure 3.8**. In Alloy 625, the expected equilibrium phases are the δ phase (orthorhombic crystal structure and composition Ni_3Nb), the γ matrix, and a small amount of $M_{23}C_6$ carbide. The γ″ phase is metastable and would be expected to transform to δ phase after longer aging treatments [34, 35, 146, 147]. Indeed, Suave *et al*. observed the γ″ to δ phase transformation in Alloy 625 after aging at 650 °C for 2000 h [34]. In Alloy 625 Plus, the δ, γ, $M_{23}C_6$ carbide, and γ′ phases are stable at 650 °C. An increase in the concentration ratio of (Al+Ti) to Nb has been shown to promote the formation of γ′ phase in Alloy 718 [148, 149]. Hence, the higher (Al+Ti)/Nb ratio in Alloy 625 Plus (0.9) compared to Alloy 625 (0.3) may stabilize the γ′ phase.

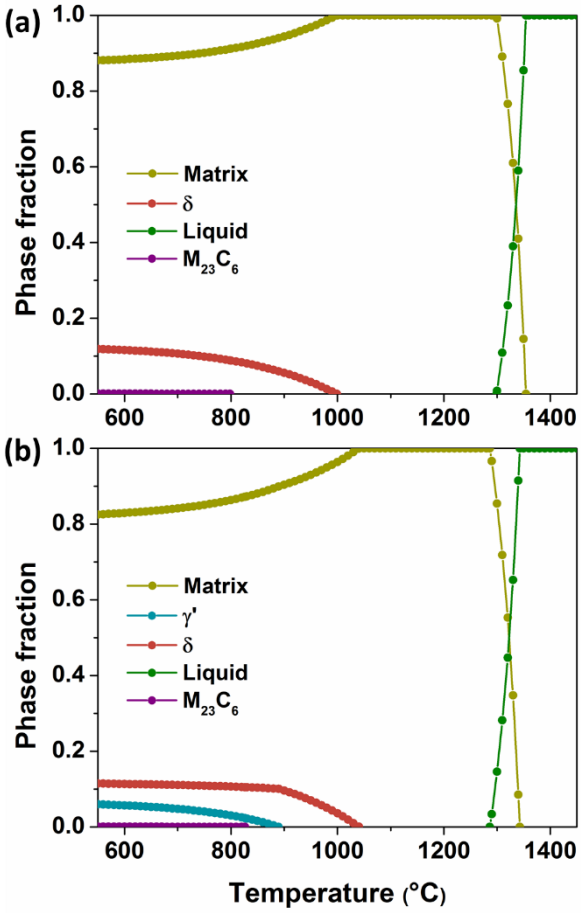

Figure 3.8. Equilibrium phase fraction in (a) Alloy 625 and (b) Alloy 625 Plus, calculated using Thermocalc software with TCNI8 database.

Regarding the γ″ phase, the measured compositions were constant with increasing aging time for both Alloy 625 and Alloy 625 Plus (**Table 3.2** and **Table 3.3**). The analysis revealed partitioning of Ni, Nb, Ti, and Al to γ″ phase, and the concentrations of these elements are within the previously reported compositional range of $Ni_3(Nb_{>0.5}Ti_{<0.5}Al_{<0.5})$ [25]. Mo and some Cr were also observed in γ″ phase. Mo appears neutral and its concentration (~6 at.%) in the γ″ phase is similar to that in the matrix, in agreement with a previous report [150]. Cr tends to partition to the γ matrix, but is also present in the γ″ phase at ~4 at.% (Alloy 625) and ~2 at.% (Alloy 625 Plus). A longer aging time (1000 h) used in a previous work [150], yielded a similar Cr concentration

value. The main difference in the γ″ phase composition between the two alloys is the Nb and Ti concentrations. The present APT measurements suggest that the higher Ti content in Alloy 625 Plus leads to stronger Ti partitioning to γ″ phase.

Regarding the γ′ phase in Alloy 625 Plus, the measured composition is close to $Ni_3(Ti_{0.4}Al_{0.4}Nb_{0.2})$. The partitioning of Ni, Ti, Al, and Nb to γ′ is in agreement with prior observations in Alloy 718 [151-153]. Compared to the APT-measured γ′ composition in Alloy 718 ($Ni_3(Ti_{0.24\sim0.36}Al_{0.36\sim0.43}Nb_{0.22\sim0.36})$) [151-153], slightly more Ti but less Nb partition to γ′ in Alloy 625 Plus.

In addition to compositional differences, the γ″ phase also exhibits different precipitation behavior. Alloy 625 Plus has a higher γ″ phase volume fraction (**Figure 3.9a**) and a number density of γ″ precipitates that is nearly an order of magnitude higher than that of Alloy 625 for the same aging conditions (**Figure 3.9b**). Considering that the γ″ phase forms as coherent precipitates in both alloys, the larger thermodynamic driving force in Alloy 625 Plus is most likely responsible for the higher number density. The evolution of the matrix compositions with aging time (**Figure 3.10**) suggests that Alloy 625 Plus started with larger supersaturations of Nb and Ti, which are the main solute elements partitioning to γ″ precipitates. Here, the extent of supersaturation was estimated using the differences in solute concentrations after solution treatment and after long-term thermal aging.

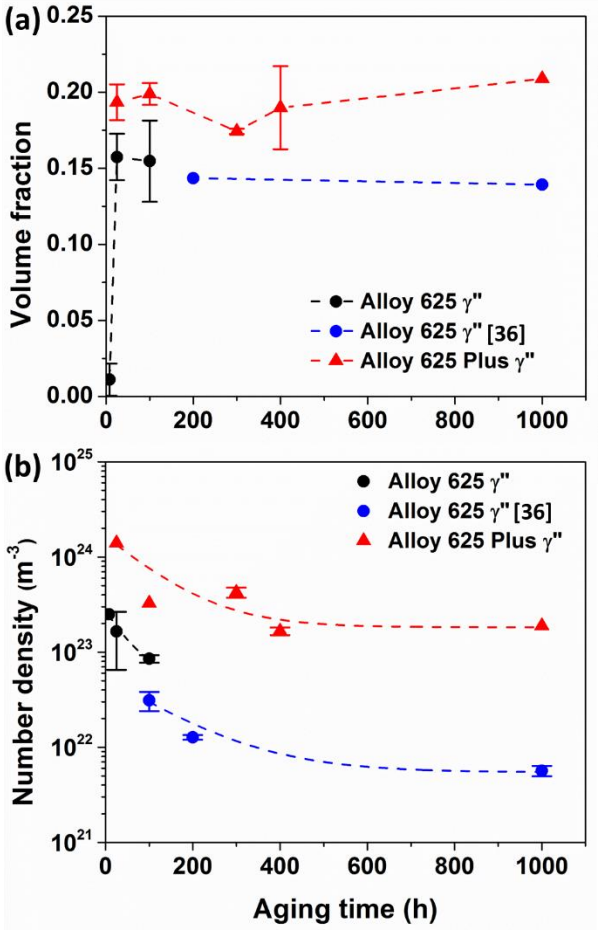

Figure 3.9. (a) Volume fraction and (b) number density of γ″ precipitates in Alloy 625 (black circles from APT results in this study, and blue circles calculated from [36]) and Alloy 625 Plus (red triangles from APT results in this study) as a function of aging time.

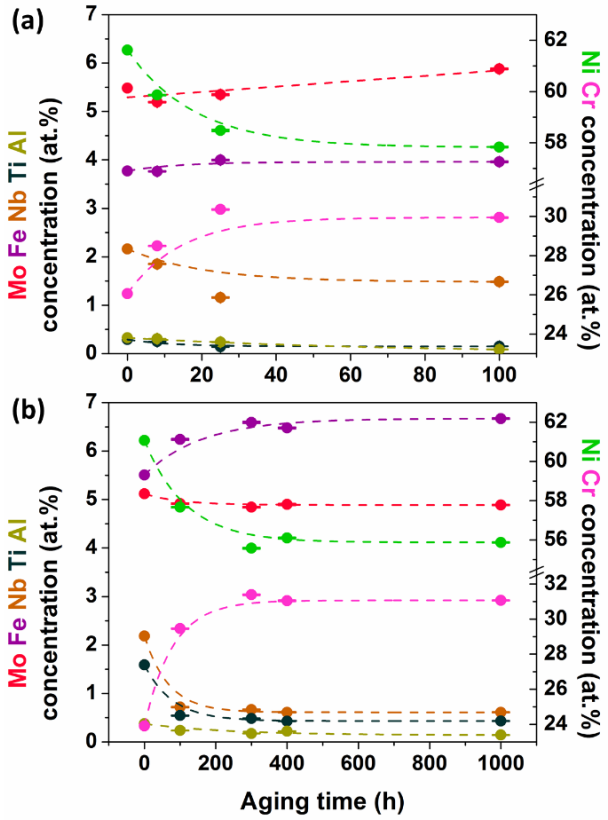

Figure 3.10. The matrix composition of (a) Alloy 625 and (b) Alloy 625 Plus as a function of aging time.

In addition to differences in γ″ nucleation rates, Alloy 625 and Alloy 625 Plus also exhibited different γ″ coarsening rates. The evolution of precipitate radius at longer aging times when the precipitate volume fractions are nearly constant, follows a relationship of $r^3 - r_o^3 = kt$ for both alloys (**Figure 3.11a**), suggesting the continued evolution is driven by minimization of interfacial energy [154, 155]. However, the coarsening rate of γ″ precipitates in Alloy 625 is faster than Alloy 625 Plus, as illustrated by the larger slope in **Figure 3.11b**. Although γ′ precipitates also formed in Alloy 625 Plus after 300 h, the low number density of γ′ precipitates may not significantly influence the coarsening kinetics of γ″ precipitates. Coarsening rate can be affected by a number of factors that include the thermodynamic properties of the phases, mobility in γ matrix of the

elements partitioning to precipitates, and interfacial energy. Knowledge of the diffusion rates of solute elements in complex superalloys is limited in the current literature. The only readily accessible quantities experimentally are the solute partitioning coefficients, defined as the ratio of the solute concentration in the precipitates and in matrix. The larger partition coefficient, the slower coarsening rate [156]. Although the compositional difference between the two alloys is only within 3 at.% for each element (**Table 2.1**), the different compositions of γ″ precipitates showed a non-trivial change in the partitioning coefficients. We only consider Nb and Ti that are the main solute elements partitioning to γ″ precipitates. The concentration of Nb is much higher than Ti in the γ″ phase of Alloy 625, whereas in Alloy 625 Plus, the concentrations of Nb and Ti are comparable (**Figure 3.2** and **Figure 3.5a**). This compositional difference results in larger partition coefficients of both Nb and Ti in Alloy 625 Plus (**Figure 3.12**), which could contribute to the slower coarsening rate of γ″ precipitates.

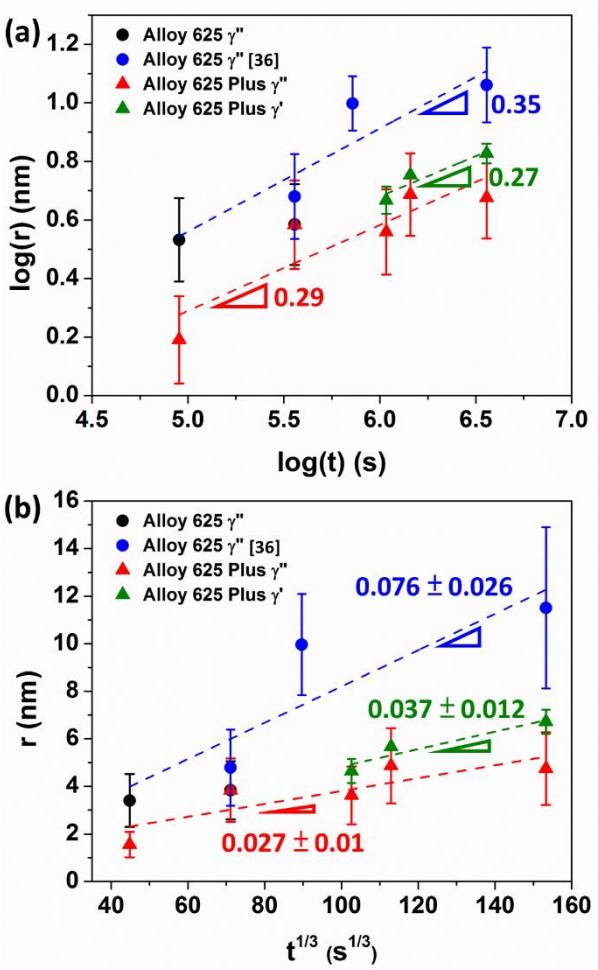

Figure 3.11. (a) log(r) versus log(t) plot (r: precipitate radius, t: aging time) showing the precipitation behavior of γ″ phase (black circles from APT results in this study, and blue circles from [36]) in Alloy 625, γ′ phase (green triangles from APT results in this study) in Alloy 625 Plus, and γ″ phase (red triangles from APT results in this study) in Alloy 625 Plus. (b) Precipitate radius (r) versus (aging time)$^{1/3}$ ($t^{1/3}$) plot showing the coarsening behavior of γ″ precipitates in Alloy 625 (black circles and blue circles), γ′ precipitates in Alloy 625 Plus (green triangles), and γ″ precipitates in Alloy 625 Plus (red triangles).

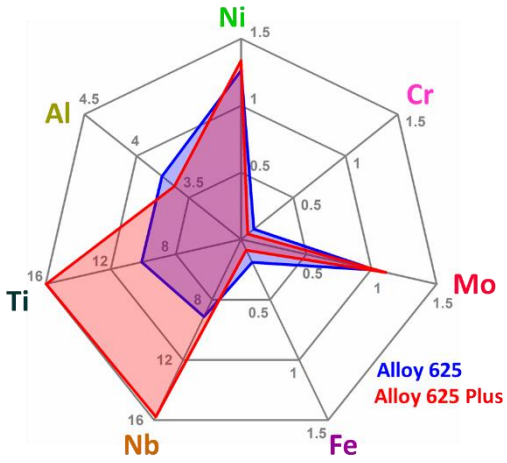

Figure 3.12. Radar chart showing the partition coefficients of each element between γ″ precipitates and γ matrix in Alloy 625 (blue) and Alloy 625 Plus (red).

In Alloy 625 Plus, γ″ phase first nucleates, and all the observed γ′ precipitates after 300-h aging are attached to γ″ precipitates, suggesting heterogeneous precipitation where interfacial and elastic strain minimization drive such precipitate arrangements. The precipitate arrangements of γ″-γ′ duplets and γ″-γ′-γ″ triplets have been reported in Alloy 718 [148, 149, 151, 157-159]. In some cases, the nucleation of γ′ occurs first and is followed by heterogeneous nucleation of γ″ on pre-existing γ′ [148, 149, 158]. Cozar and Pineau [148] suggested that the γ′/γ″ interface is coherent and is associated with low energy due to the atomic matching between the {1 0 0} planes of the $L1_2$ structure of γ′ and the (1 0 0) plane of the $D0_{22}$ structure of γ″. Heterogeneous nucleation is favored since the γ″/γ′ interface has a smaller lattice misfit than the γ″/γ interface [148]. Other researchers found that the γ″ phase can precede the γ′ phase, as observed in [151, 159]. Miller postulated that the Al rejection from pre-existing γ″ precipitates favors the nucleation of γ′ precipitates [151]. However, Al was found to only slightly partition to the γ″ precipitates in Alloy 625 Plus (**Figure 3.5a**). Alternatively, Sundararaman *et al.* suggested that the duplet or triplet arrangements could occur through the encountering of independently nucleated neighboring γ″ and

γ′ precipitates [159]. Notably, Theska *et al.* observed not only the γ″-γ′-γ″ but also γ′-γ″-γ′ triplets depending on the aging conditions used. However the precipitation sequences were not specified [157]. It remains unclear what controls the sequence and arrangements of these precipitates and further observations during the onset of γ′ nucleation (between 100 and 300 h at 650 °C) in Alloy 625 Plus are needed to rationalize formation process of the less intuitive γ″-γ′-γ″ triplet arrangements.

Finally, further clarification on the mechanical properties of these two similar Ni-based alloys after the same aging condition would be valuable to shed light on how minor change in composition affects alloy properties, and this preliminary microstructural study would be beneficial for explaining the outcomes.

3.5 Conclusions

In this study, the precipitation behavior of two similar commercial Ni-based alloys, Alloy 625 and Alloy 625 Plus, under the same aging conditions (solution treatment at 1100 °C for 1 h followed by thermal aging at 650 °C up to 1000 h) were quantitatively compared. The following conclusions were drawn:

- γ″ precipitates were observed in Alloy 625 and Alloy 625 Plus after aging for 8 h and longer, and γ′ phase precipitated in Alloy 625 Plus when aged for 300 h and longer.
- The APT-measured compositions of γ″ phase in Alloy 625 and Alloy 625 Plus are close to Ni_3(Nb, Mo, Ti, Al). The higher Ti content in Alloy 625 Plus leads to stronger Ti partitioning to γ″ phase compared to Alloy 625.
- The APT-measured composition of γ′ phase in Alloy 625 Plus is close to $Ni_3(Ti_{0.4}Al_{0.4}Nb_{0.2})$.

- In Alloy 625 Plus, all the observed γ′ precipitates are attached to pre-existing γ″ precipitates in γ″-γ′ duplet or γ″-γ′-γ″ triplet arrangements.
- The larger supersaturations of Nb and Ti in Alloy 625 Plus may result in the higher number density and higher volume fraction of γ″ precipitates.
- Alloy 625 Plus has higher Nb and Ti partition coefficients than Alloy 625, which may contribute to the slower coarsening rate of the γ″ precipitates.

Chapter 4

Microstructural Evolution in Alloy 625 Plus under Irradiation

4.1 Introduction

The license renewal of commercial nuclear power reactors authorized the nuclear power plants to extend their operating lifetimes from the original 40 years to 60 years or beyond [2]. Consequently, structural materials used in nuclear reactors have to withstand higher radiation damage, extended thermal exposure, and longer corrosion period than before. Accordingly, it is important to test and qualify materials with improved irradiation resistance, and understand how microstructures and mechanical properties change under relevant irradiation conditions.

Commercial Ni-based superalloys continue to be considered for nuclear applications due to their excellent mechanical properties and corrosion resistance at relevant reactor temperatures [6-8]. Ni-based alloys serve as control rod drive mechanism assemblies, bolts, springs, and steam generator tubing materials in light water reactors [9, 13, 23, 24]. Among commercial Ni-based alloys, Alloy 625 Plus, a modified alloy based on Alloy 625 with improved age-hardening capability and comparable corrosion resistance [42], was proposed for use as candidate core internal components in light water reactors [10, 11]. However, little is known about Alloy 625 Plus's behavior during thermal aging and irradiation.

Prior research showed that a high volume fraction (~20%) of the body-centered tetragonal Ni_3(Nb, Mo, Ti, Al) γ'' precipitates form in Alloy 625 Plus after thermal aging at temperatures

between 650 and 800 °C (**Chapter 3** and [43]), and act as a strengthening phase [43]. A lower density of FCC $L1_2$ $Ni_3(Ti_{0.4}Al_{0.4}Nb_{0.2})$ γ′ precipitates also form (**Chapter 3**). Under proton irradiation, the body-centered orthorhombic Pt_2Mo-type ordered phase was observed after irradiation at 360 °C [93, 130]. To further confirm the precipitation paths under irradiation, role of cascade mixing, and interactions between precipitate phases, we carried out long term thermal aging, as well as proton and ion irradiations at 300 and 400 °C. Solutionized samples and aged samples (with pre-existing γ″ precipitates) were irradiated to verify the influence of pre-existing γ″ precipitates on microstructural evolution during irradiation.

4.2 Materials and method

Alloy 625 Plus (Heat number: 215846) was supplied by Carpenter Technology Corporation in as-received condition (solutionized at 1038 °C for 2 h, fan cooled, aged at 735 °C for 8 h, cooled at 56 °C/h to 621 °C and aged for 8 h, air cooled), and its chemical composition measured by atom probe tomography (APT) can be found in **Table 3.1**. Some samples in as-received condition were thermally aged at 330 and 418 °C for 10,000 h without irradiation in order to explore the low-temperature precipitation behavior. Other samples that were prepared for irradiation were sectioned into small pieces with the dimension of $12 \times 2 \times 3$ mm^3, and solution treated at 1100 °C for 1 h in Ar filled quartz tubes, followed by water quenching (hereafter called solutionized samples). Several samples were also thermally aged at 650 °C for 100 h after solution treatment to form γ″ precipitates (hereafter called aged samples). Sample surfaces for irradiation were electropolished at 30 V in a 10% perchloric acid + 90% methanol electrolyte at -30 °C.

Solutionized and aged samples were proton or ion irradiated at the Michigan Ion Beam

Laboratory. The irradiation conditions are summarized in **Table 4.1**. Stopping and Range of Ions in Matter (SRIM) calculation [160] was performed to estimate the damage level using Kinchin–Pease model [48, 161] with the displacement energy of 25 eV [162]. Proton irradiations were conducted using a 2 MeV proton beam at 300 and 400 °C at an approximate dose rate of 10^{-5} dpa/s. Transmission electron microscopy (TEM) and APT specimen preparation and characterization were performed on regions about 3 μm below the sample surface. Ion irradiations were performed using a 5 MeV Ni ion beam at 300 and 400 °C. Characterization was conducted at ~700 nm below the sample surface, which corresponds to an approximate dose rate of 10^{-4} dpa/s. Ion irradiations at 300 °C at the dose rate of 10^{-3} dpa/s were also conducted using the same method.

TEM and APT specimens were prepared using a standard lift-out process on both Thermo Fisher Nova 200 and Thermo Fisher Helios 650 Nanolab dual scanning electron microscope (SEM)/focused ion beam (FIB) instruments. JEOL 3011 TEM and Thermo Fisher Talos F200X G2 TEM were used for TEM specimen characterization. APT specimens were run on both CAMECA LEAP 4000X HR and 5000 XR instruments in laser mode at 50 K, using a pulse energy of 40 to 50 pJ, 200 kHz pulse rate, and a target detection rate of 0.5%. The collected APT data were analyzed using the IVAS 3.8.4 software. Datasets were reconstructed based on voltage evolution using the evaporation field of Ni (35 nm/V [144]). The image compression factor (adjusted between 1.2 and 1.8) and field factor k_f (adjusted between 2.8 and 3.9) were modified to minimize the atomic density variations of datasets along longitudinal and radial directions

Table 4.1. Summary of the irradiation conditions.

	Proton irradiation		Ion irradiation		
Temperature (°C)	300	400	300	400	300
Dose rate (dpa/s)	10^{-5}	10^{-5}	10^{-4}	10^{-4}	10^{-3}
Dose (dpa)	1.5, 6, 11* 5*	3	1.5	3	1.5

* 1.5, 6, and 11 dpa are for solutionized samples; 5 dpa is for aged samples.

4.3 Results

4.3.1 Microstructures after thermal treatments

We first report on the microstructures of the thermally treated samples. The as-received samples contained γ″ precipitates due to a prior heat treatment history, and were unfortunately not annealed prior to low temperature thermal aging. The superlattice diffraction spots at {1 0 0}, {1 1/2 0}, and {1 1 0} positions in the <0 0 1>-zone TEM diffraction pattern (DP) confirmed the presence of the γ″ phase (**Figure 4.1a**). The average diameter of γ″ precipitates was 15.8 ± 3.1 nm, which was measured from the dark-field (DF) images taken under g = [2 0 0] condition using the (-1 0 0) superlattice diffraction spot (**Figure 4.1a**).

The γ″ precipitates remained largely unchanged after aging at both 330 and 418 °C for 10,000 h (**Figure 4.1b, c**). The average diameters of γ″ precipitates were 18.1 ± 3.6 and 19.5 ± 4.3 nm in the samples aged at 330 and 418 °C, respectively. The size distributions of γ″ precipitates after each thermal treatment condition are shown in **Figure 4.2**. The Pt_2Mo-type ordered phase formed in the samples aged at 418 °C for 10,000 h, as evidenced by the corresponding superlattice diffraction spots at {2/3 2/3 0}, {4/3 4/3 0}, and {2/3 4/3 0} positions in the <0 0 1>-zone TEM DP (**Figure 4.1c**).

A solution treatment at 1100 °C for 1 h successfully dissolved all existing precipitates, as shown in **Figure 4.3a**. APT ion maps of these solutionized samples showed uniform distribution of each element, and the TEM DP displayed only the γ matrix spots. After subsequent thermal aging at 650 °C for 100 h, precipitation of a high volume fraction (~20%) of dense γ″ precipitates is illustrated via APT ion maps (**Figure 4.3b**). Nb and Ti partitioned to the γ″ phase, and the analysis of the γ″ precipitate composition can be found in **3.3.2**. Electron diffraction also confirmed the presence of γ″ phase.

The APT measured compositions of γ matrix and γ″ precipitates after 650 °C aging for 100 h, and the composition of γ′ precipitates that had been previously observed after aging at 650 °C for longer than 300 h can be found in **Table 3.3**.

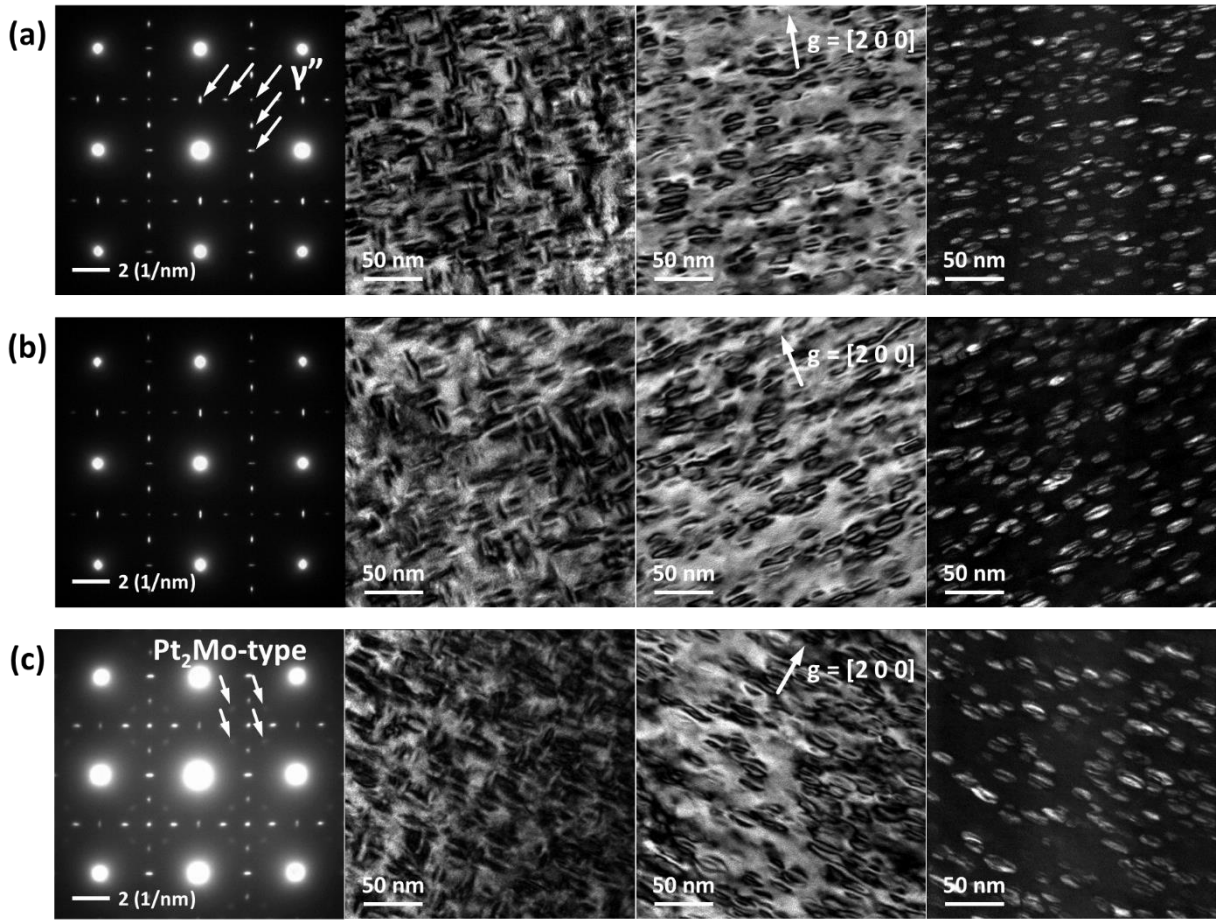

Figure 4.1. (From left to right) <001>-zone TEM DPs, <001>-zone TEM bright-field (BF) images, TEM BF images taken under g = [2 0 0] diffraction condition, and TEM DF images taken under g = [2 0 0] diffraction condition using (-1 0 0) superlattice diffraction spot of Alloy 625 Plus (a) in as-received condition, (b) after 330 °C aging for 10,000 h, and (c) after 418 °C aging for 10,000 h. The TEM DF images show one of the three variants of γ″ precipitates.

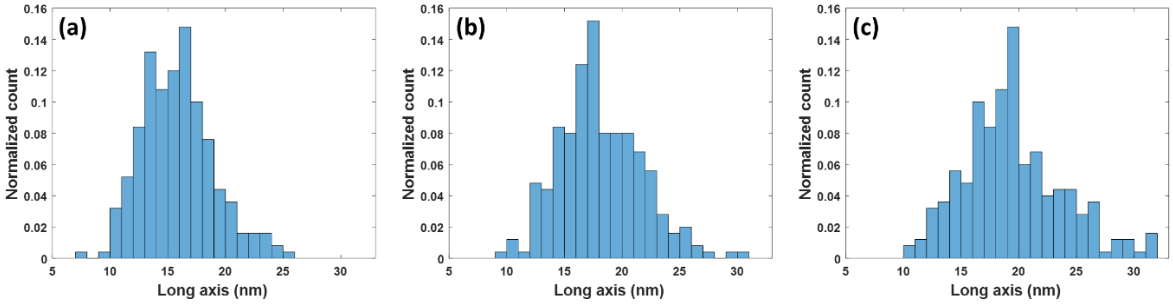

Figure 4.2. Diameter distributions of γ″ precipitates in Alloy 625 Plus (a) in as-received, (b) after 330 °C aging for 10,000 h, and (c) after 418 °C aging for 10,000 h.

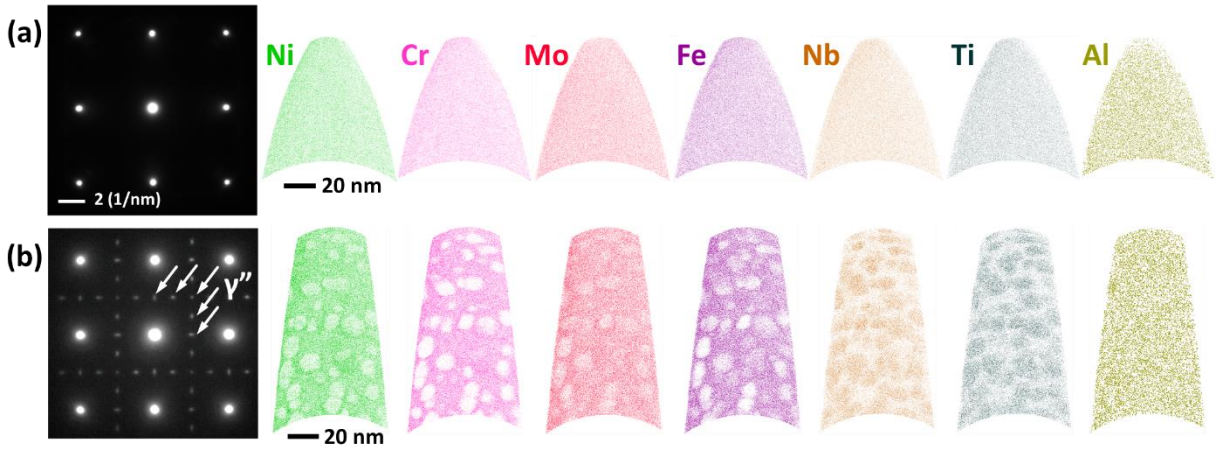

Figure 4.3. <0 0 1>-zone TEM DPs and APT ion maps of Alloy 625 Plus after (a) solution treatment at 1100 °C for 1 h and (b) solution treatment + thermal aging at 650 °C for 100 h. The thicknesses of ion map slices are 1, 2, 10, 10, 20, 20, and 20 nm for Ni, Cr, Mo, Fe, Nb, Ti, and Al, respectively, and the same thicknesses will be used in this chapter.

4.3.2 Proton-irradiated microstructures

Proton irradiation at 300 °C caused phase separation in solutionized samples, with the formation of Pt_2Mo-type ordered phase and γ″ phase, and solute clustering of Nb, Ti, Al, and Si. After 1.5 dpa, the presence of the Pt_2Mo-type ordered phase was evidenced by electron diffraction (**Figure 4.4a**). This phase remained as dose increased to 11 dpa, as shown in **Figure 4.4c**. At 6 and 11 dpa, the γ″ phase superlattice spots were also observed (**Figure 4.4b, c**). The APT ion maps also revealed the presence of uniformly distributed Nb-rich clusters. These Nb-rich clusters, delineated by Nb iso-concentration surfaces (**Figure 4.5a**), were enriched in Ni, Nb, and Ti, and slightly in Al while depleted in Cr and Fe (**Figure 4.5b**, **c**). The Mo concentration was nearly the same in the matrix and Nb-rich clusters (**Figure 4.5c**). Al-rich clusters also developed, mostly visible in the Al atom distributions. The locations of Al-rich clusters did not match those of the

Nb-rich clusters (**Figure 4.5a**, **d**). The Al-rich clusters were enriched in Ni, Al, Ti, and Nb while depleted in Cr, Fe, and Mo (**Figure 4.5e**, **f**). The different Mo partition behaviors of Al-rich clusters and Nb-rich clusters were consistent with the observations in thermally aged Alloy 625 Plus containing both γ′ and γ″ precipitates (**3.3.2**). Thus, the Al-rich clusters and Nb-rich clusters were precursors of γ′ Ni_3(Ti, Al, Nb) and γ″ Ni_3(Nb, Mo, Ti, Al) precipitates, respectively. Si-rich clusters were observed at all three doses (**Figure 4.4**). Composition measurements revealed the enrichment of Ni and Si (**Figure 4.6**).

The microstructures observed in the aged samples proton-irradiated to 5 dpa were reported in **Figure 4.7**. The Pt_2Mo-type ordered phase formed and pre-existing γ″ precipitates that formed during aging at 650 °C exhibited diffuse compositional interfaces and lower solute partitioning behavior. However, ordering was still visible by electron diffraction.

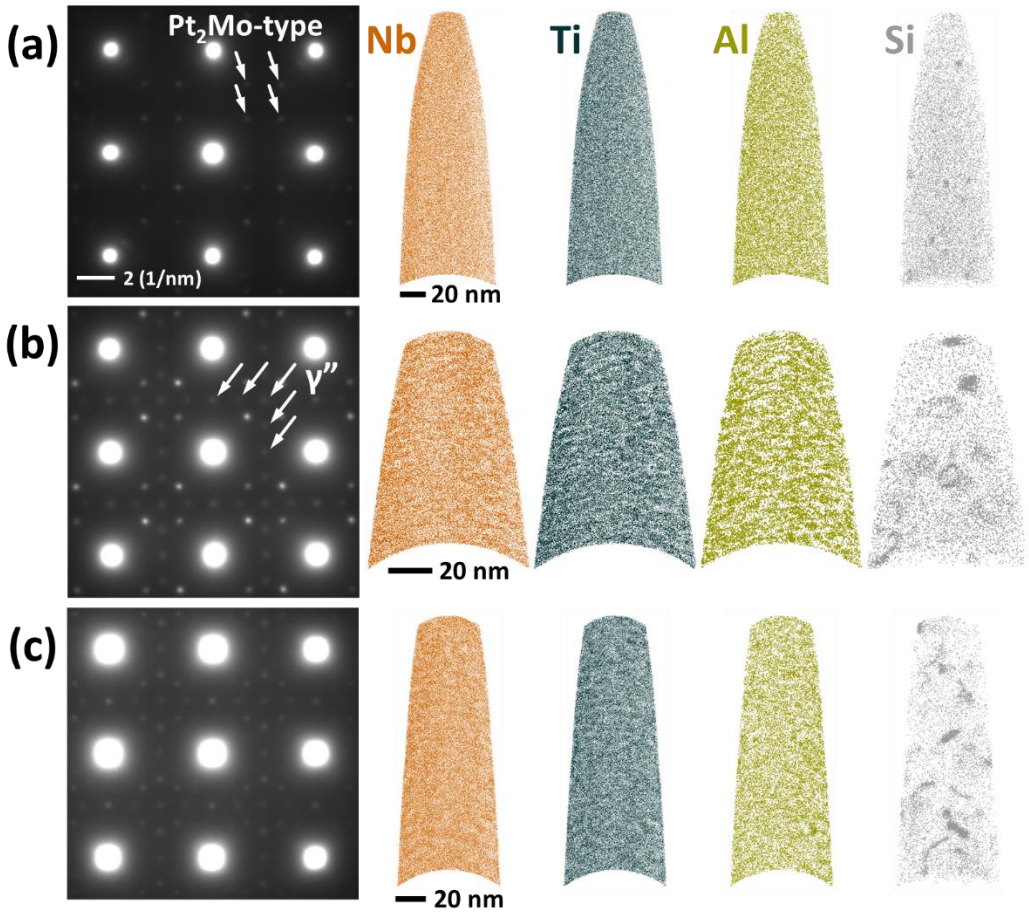

Figure 4.4. <0 0 1>-zone TEM DPs and APT ion maps after proton irradiation at 300 °C to (a) 1.5, (b) 6, and (c) 11 dpa.

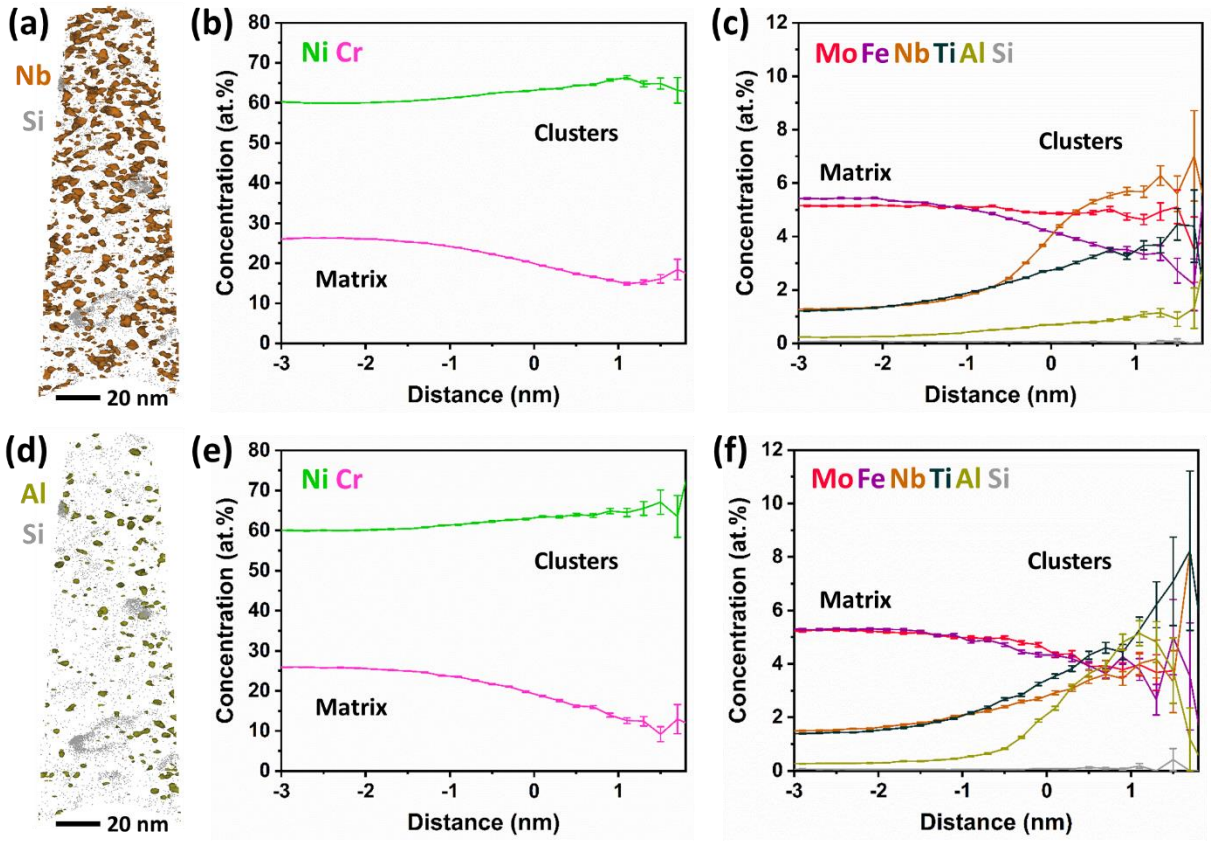

Figure 4.5. 20-nm slices of APT ion maps of (a) Nb-rich clusters and (b)-(c) their corresponding proximity histogram (proxigrams) calculated from Nb = 2.8 at.% iso-concentration surfaces, and (d) Al-rich clusters and (e)-(f) their corresponding proxigrams calculated from Al = 1.2 at.% iso-concentration surfaces. The error bars are based on the counting error $\sqrt{c_i(1-c_i)/N_{bin}}$, where c_i is the atomic fraction of element i and N_{bin} is the total number of atoms in the bin.

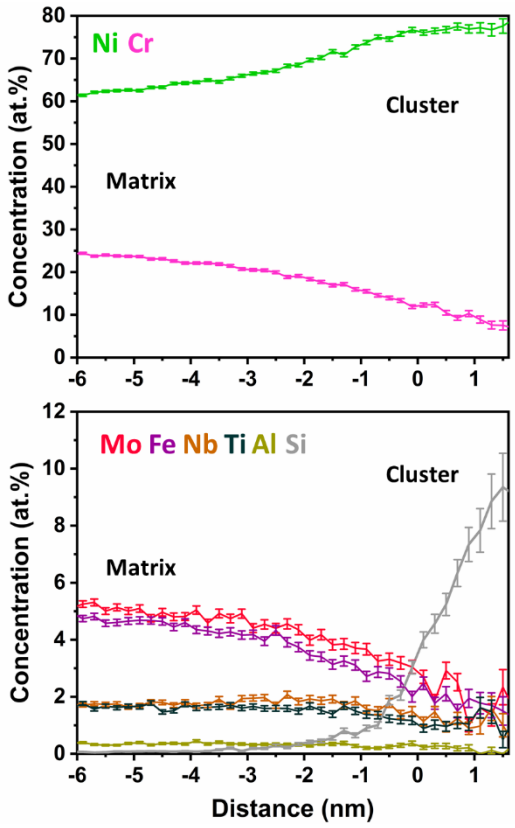

Figure 4.6. Proxigrams of Si-rich clusters, generated from Si = 2.8 at.% iso-concentration surfaces in Alloy 625 Plus after proton irradiation at 300 °C to 11 dpa.

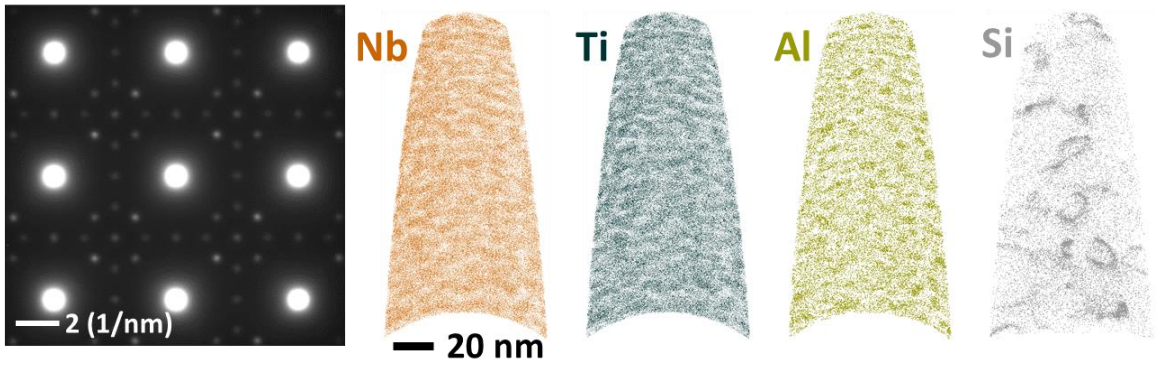

Figure 4.7. <0 0 1>-zone TEM DP and APT ion maps of Alloy 625 Plus after 650 °C aging for 100 h + proton irradiation at 300 °C to 5 dpa.

As highlighted by both APT and electron diffraction observations (**Figure 4.8**), γ″, γ′, and Ni_3Si precipitates were observed in the solutionized samples that were proton irradiated at 400 °C for 3 dpa. APT ion maps revealed a high density of uniformly distributed Nb-rich clusters, whose composition was consistent with that of the γ″ phase (**Figure 4.9**). Similarly, the compositions of the Al-rich clusters and the Si-rich particle matched those of the γ′ and the Ni_3Si phases, respectively. Electron diffraction did not reveal the presence of the Pt_2Mo-type ordered phase. In the irradiated aged samples, γ″, γ′, and Ni_3Si were also observed. In addition, the Pt_2Mo-type ordered phase formed, as revealed by electron diffraction (**Figure 4.8**).

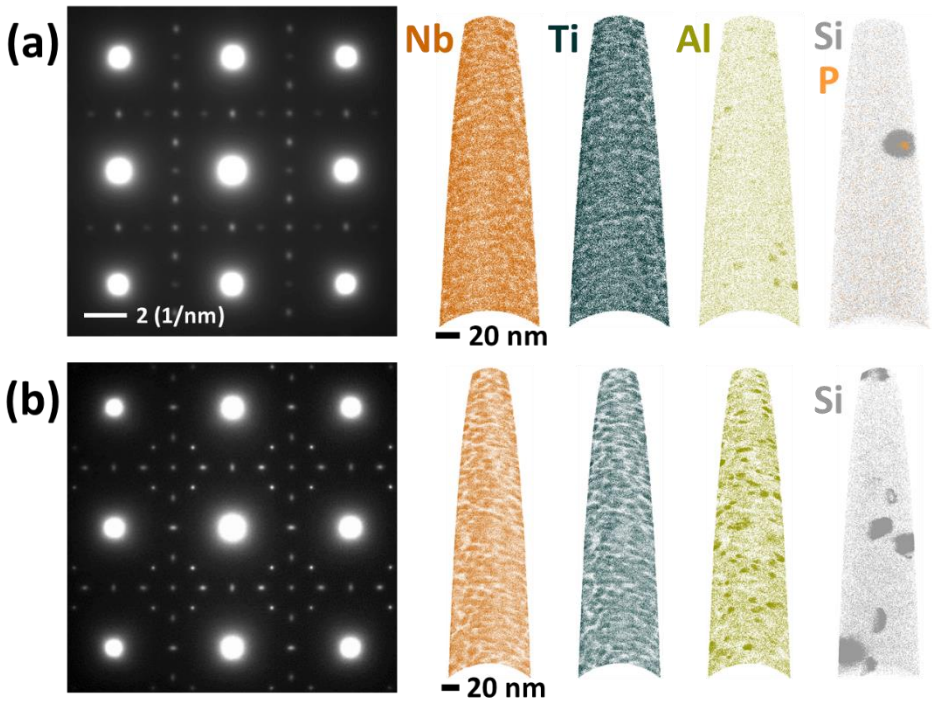

Figure 4.8. <0 0 1>-zone TEM DPs and APT ion maps of (a) solutionized and (b) aged samples after proton irradiation at 400 °C to 3 dpa.

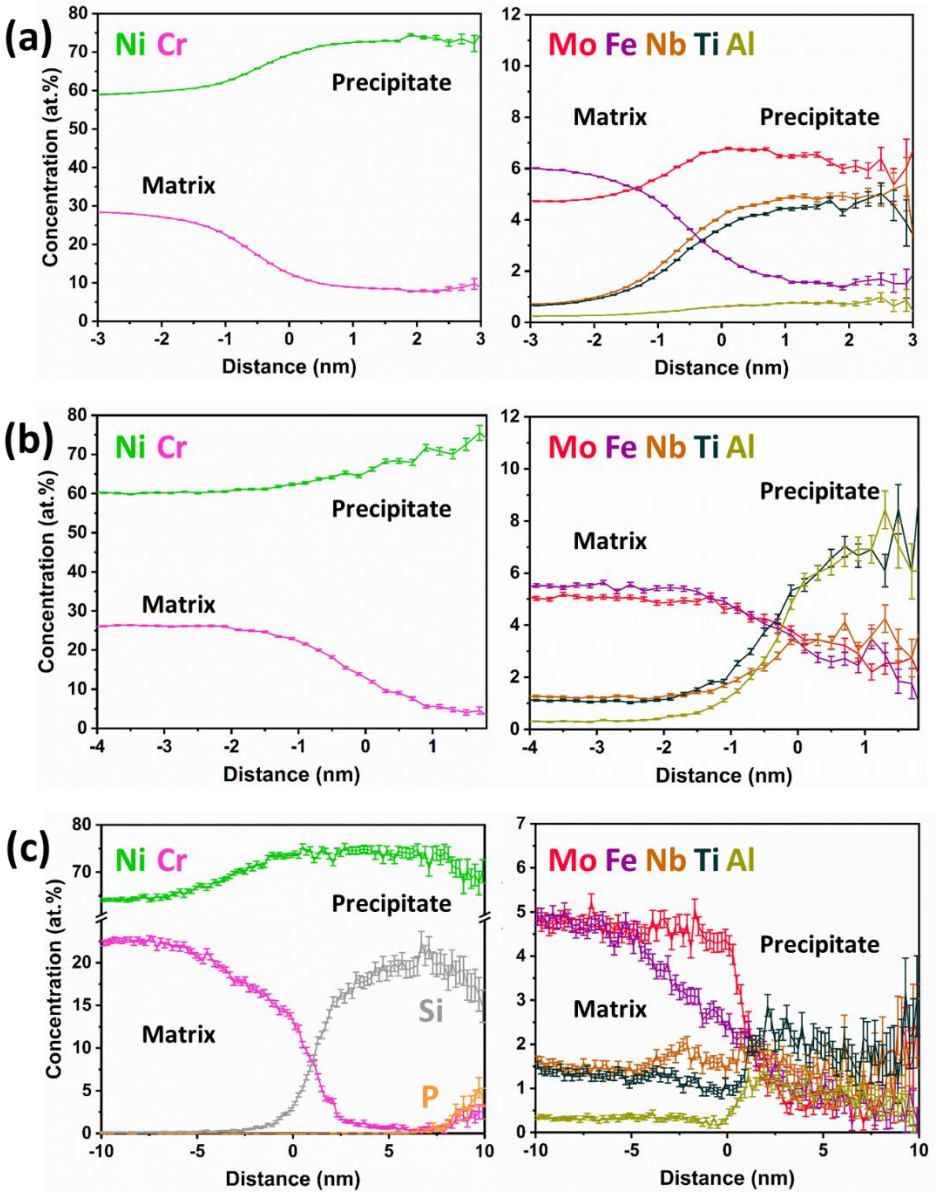

Figure 4.9. Proxigrams of (a) γ″ precipitates, generated from Cr = 18 at.% iso-concentration surfaces, (b) γ′ precipitates, generated from Al = 3 at.% iso-concentration surfaces, and (c) Ni_3Si precipitates, generated from Si = 4 at.% iso-concentration surfaces in Alloy 625 Plus after proton irradiation at 400 °C to 3 dpa.

Radial distribution function (RDF) analyses of the Nb and Al distributions were performed on the APT datasets of the irradiated samples (**Figure 4.10**). The normalized concentration fluctuation curves were fitted using the equation [163]:

$$\frac{C_i(r)}{C_i^0} = A\,cos\left(\frac{2\pi r}{\lambda}\right) exp\left(-\frac{r}{\xi}\right) + 1$$

where $C_i(r)$ is the average concentration of element i at the distance of r from an i atom, C_i^0 is the bulk concentration of element i in the analyzed volume, A is the amplitude of the normalized concentration fluctuations and is a surrogate for the cluster concentration, λ is the wavelength of the fluctuation and a measure of interparticle spacing, and ξ is the correlation length that describes the attenuation of the fluctuation and the size of the clusters. The number density of the clusters is approximated by λ^{-3}. Nb and Al were selected to quantify solute clusters consistent with the γ″ and γ′ phases, respectively. The correlation lengths and wavelengths of the Nb and Al clusters in the solutionized and aged samples appeared to converge toward the same values as dose increased. After proton irradiation at 300 °C, the correlation length for Nb reached to ~2.3 nm at 11 dpa in the solutionized samples, while it decreased from ~4.7 nm to ~2.7 nm at 5 dpa in the aged samples (**Figure 4.10a**). Similarly, the correlation lengths of the Al clusters were comparable in the solutionized (~1.9 nm at 11 dpa) and aged (~2.0 nm at 5 dpa) samples (**Figure 4.10b**). The (wavelength)$^{-3}$ of the Nb clusters reached similar values in the solutionized (~1.6 × 10^{23} m^{-3} at 11 dpa) and aged (~1.3 × 10^{23} m^{-3} at 5 dpa) samples. Likewise, the (wavelength)$^{-3}$ of the Al clusters reached a similar value in the solutionized (~1.8 × 10^{23} m^{-3} at 11 dpa) and aged (~1.8 × 10^{23} m^{-3} at 5 dpa) samples. At 400 °C and 3 dpa, the correlation length of the Nb clusters in the solutionized increased to ~2.5 nm while it decreased to ~3.2 nm in the aged samples (**Figure 4.10a**). The (wavelength)$^{-3}$ of the Nb clusters remained slightly larger in the solutionized (~1.2 × 10^{23} m^{-3}) than in the aged (~0.6 × 10^{23} m^{-3}) samples (**Figure 4.10c**). For the Al clusters, comparable correlation lengths in the solutionized (~3.1 nm) and aged (~3.0 nm) samples were observed (**Figure 4.10b**). The (wavelength)$^{-3}$ remained larger in the solutionized (~0.5 × 10^{23} m^{-3}) than in the aged (~0.3 × 10^{23} m^{-3}) samples (**Figure 4.10c**).

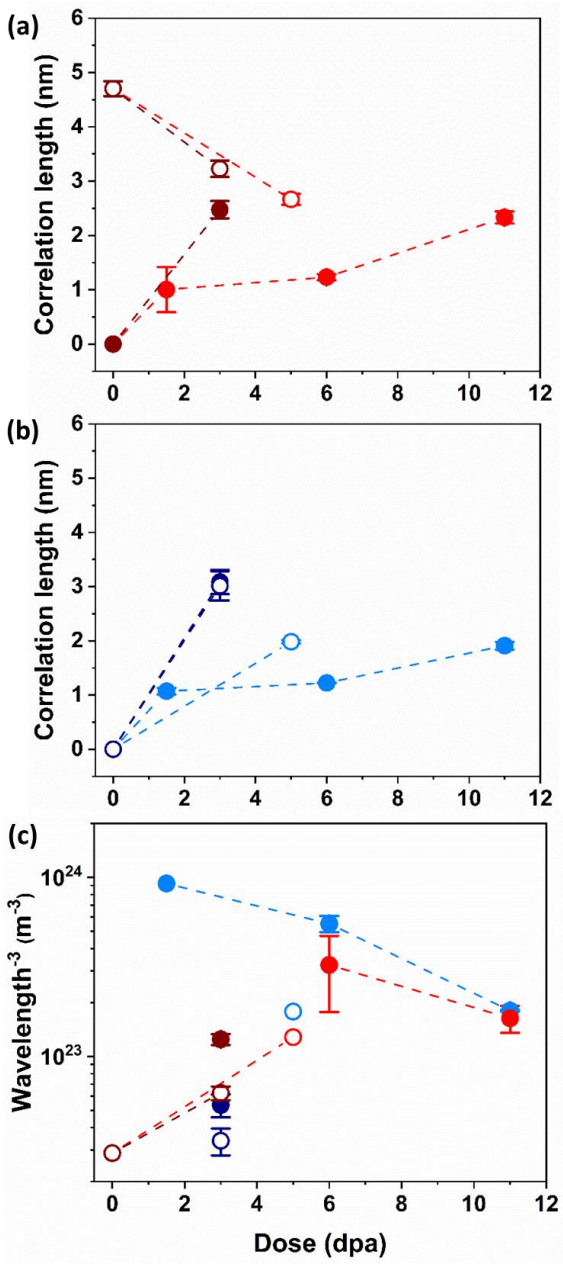

Figure 4.10. (a) The evolution of correlation length of Nb-rich clusters/γ″ precipitates after proton irradiation at 300 (red) and 400 °C (dark red) for solutionized (solid symbols) and aged (hollow symbols) conditions. (b) The evolution of correlation length of Al-rich clusters/γ′ precipitates after proton irradiation at 300 (blue) and 400 °C (dark blue) for solutionized (solid symbols) and aged (hollow symbols) conditions. (c) The evolution of (wavelength)$^{-3}$ of Nb-rich clusters/γ″ precipitates (red for 300 °C and dark red for 400 °C) and Al-rich clusters/γ′ precipitates (blue for 300 °C and dark blue for 400 °C) after proton irradiation for solutionized (solid symbols) and aged (hollow symbols) conditions.

4.3.3 Ion-irradiated microstructures

After ion irradiation at 300 °C for 1.5 dpa at the dose rate of 10^{-4} dpa/s, the spatial distribution of solute atoms in the solutionized samples remained uniform (**Figure 4.11a**). Pre-existing γ″ precipitates in the aged samples disordered, as evidenced by the absence of superlattice spots in **Figure 4.11b**. Compositionally, dissolution is also evident (**Figure 4.11b**), with the γ″ precipitates/matrix interface becoming wider, as illustrated by the proxigrams in **Figure 4.12**.

After ion irradiation at 400 °C for 3 dpa at the dose rate of 10^{-4} dpa/s, the solutionized samples remained as solid solution (**Figure 4.13a**). In the aged samples, the γ″ phase remained ordered (as evidenced by the superlattice reflections in the TEM DP) but with significantly smaller precipitate size as shown by the nanoscale clustering of Nb and Ti in the APT maps (**Figure 4.13b**). The Pt_2Mo-type ordered phase (**Figure 4.13b**) and Al clusters also formed during irradiation (**Figure 4.14**). Ion irradiations were also conducted at 300 °C to 1.5 dpa using a higher dose rate (10^{-3} dpa/s), after which the alloy also exhibited random distributions of all elements.

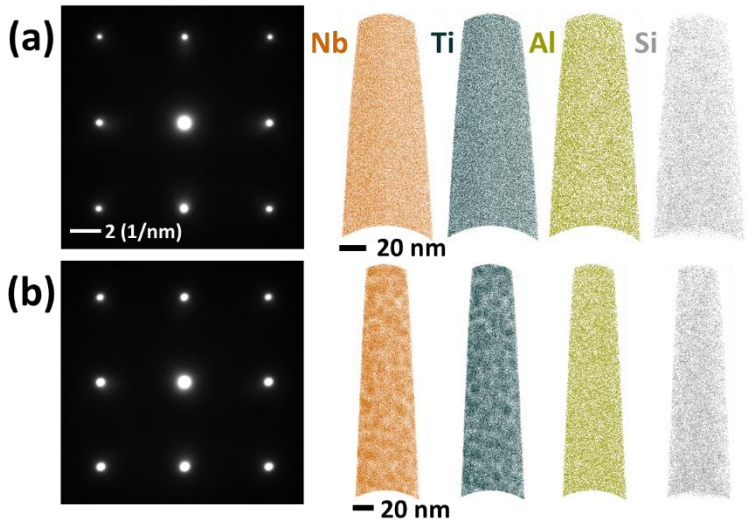

Figure 4.11. <0 0 1>-zone TEM DPs and APT ion maps of Alloy 625 Plus after (a) solution treatment + Ni ion irradiation to 1.5 dpa, (b) 650 °C aging for 100 h + Ni ion irradiation to 1.5 dpa at the dose rate of 10^{-4} dpa/s at 300 °C.

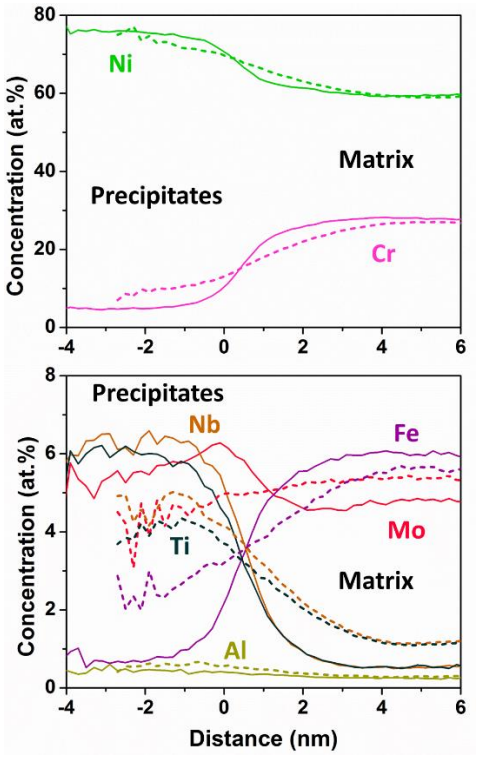

Figure 4.12. Proxigrams of γ″ precipitates, generated from Cr = 16 at.% iso-concentration surfaces, in Alloy 625 Plus after 650 °C aging for 100 h (solid lines) and post-aging ion irradiation to 1.5 dpa (dashed lines). Error bars are removed for clarity.

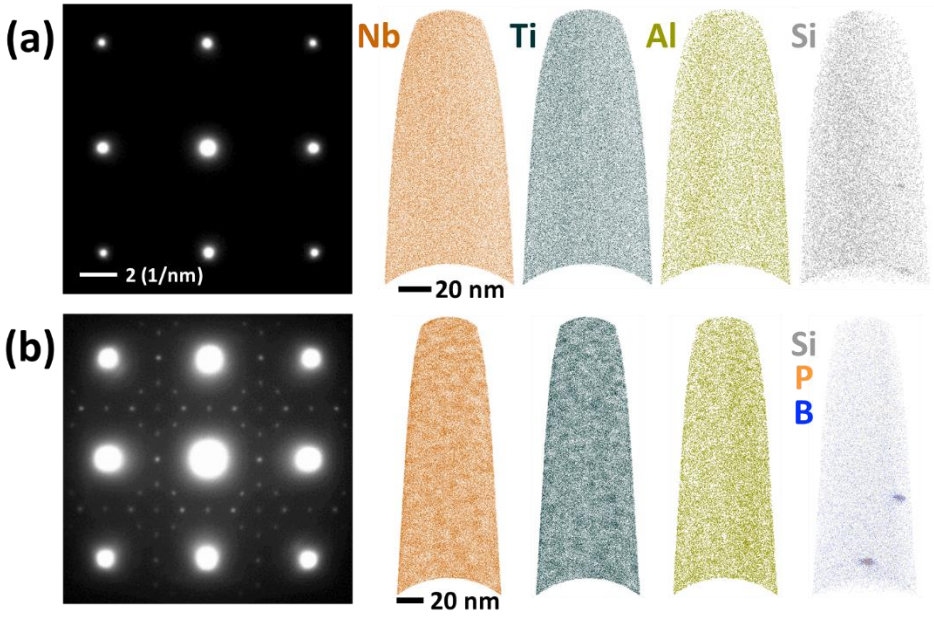

Figure 4.13. <0 0 1>-zone TEM DPs and APT ion maps of (a) solutionized and (b) aged samples after ion irradiation at 400 °C to 3 dpa at the dose rate of 10^{-4} dpa/s.

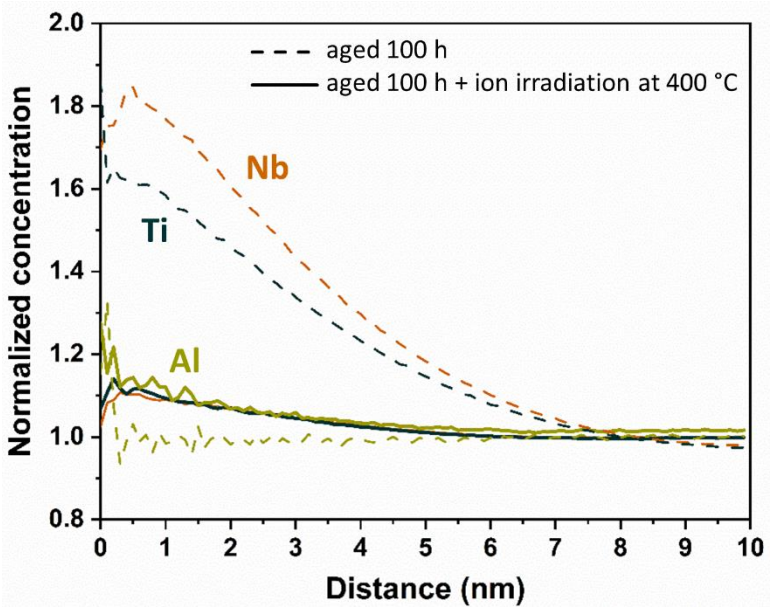

Figure 4.14. RDF plot of normalized concentration of Nb, Ti, and Al atoms in aged samples (dashed lines) and aged samples after ion irradiation at 400 °C to 3 dpa at the dose rate of 10^{-4} dpa/s (solid lines).

4.4 Discussion

The microstructure evolution of Alloy 625 Plus during thermal aging involves the precipitation of γ′, γ″, and Pt_2Mo-type ordered phases. Equilibrium predictions using Thermocalc (the CALPHAD method) suggest that the γ′ phase and δ phase are stable phases while the γ″ phase is metastable (**Chapter 3**). The precipitation of the γ′ and γ″ phases has only been experimentally observed during thermal aging above 650 °C (**Chapter 3** and [43]). γ″ precipitates first, followed by γ′ precipitation (**Chapter 3**). Eventually, the δ phase forms at the expense of γ″ and γ′ after longer aging treatments [34, 35, 146, 147]. Our long-term aging results show that the γ″ precipitates evolve extremely slowly at 330 and 418 °C, suggesting that metastability is favored by slow diffusion kinetics. The Pt_2Mo-type ordered phase is also expected at temperatures below 418 °C (**Figure 4.1c**) and the absence of Pt_2Mo-type phase after aging at 330 °C for 10,000 h (**Figure 4.1b**) may also be attributed to the sluggish ordering rate [38]. Under irradiation, phase decomposition involves not only the γ′, γ″, and Pt_2Mo-type phases but the Ni_3Si phase. We now discuss the role of irradiation conditions and matrix composition on the formation mechanism of each phase.

While slow diffusion kinetics hinder the formation of γ′ and γ″ precipitates at lower temperatures, both phases were readily observed after proton irradiation at 300 and 400 °C, pointing to a radiation-enhanced diffusion mechanism whereby the increased point defect concentration accelerates the precipitation process [54]. However, cascade mixing also plays a role in controlling the extent of phase separation. Indeed, the microstructures of the solution annealed and aged samples during proton irradiation converged toward the same steady state microstructural state, characterized by higher number densities and smaller cluster sizes than in the aged state.

While higher dose experiments would be necessary to confirm the establishment of a steady state non-equilibrium microstructure at 400 °C, our experiments nonetheless suggest that the steady state microstructure is a function of temperature, confirming the balancing effects of radiation accelerated diffusion and cascade mixing. The larger precipitate sizes and lower number densities observed after irradiation at 400 °C compared to those at 300 °C are consistent with the increase rate of solute diffusion at the higher temperature when the rate of cascade mixing is kept constant. In contrast to proton irradiations, ion irradiation at 300 °C led to solid solution for both solutionized and aged samples, which is mainly attributed to the higher cascade damage rate. However, the extent of influence of different cascade efficiencies between proton and ion irradiations may need further clarification. For ion irradiation at 400 °C, the longer survival of pre-existing γ″ precipitates after 3 dpa (**Figure 4.13b**), and Al clustering (**Figure 4.14**) are again consistent with faster rates of diffusion at the higher temperature that mitigate the effects of cascade mixing.

The Pt_2Mo-type ordered phase precipitated at temperatures near 300 °C under proton irradiation after ~40 h (1.5 dpa) but not under thermal aging after 10,000 h. Thus, the precipitation of this phase also follows a diffusion-accelerated mechanism, as previously reported [93]. However, the Pt_2Mo-type phase was not always observed and we hypothesize that γ″ precipitation influences the formation of the Pt_2Mo-type phase by altering the matrix Ni/Cr value through different Ni and Cr partitioning behaviors. The Ni/Cr concentration ratios in the matrix under all the irradiation conditions are summarized in **Figure 4.15**. We hypothesize that the Pt_2Mo-type ordered phase tends to precipitate when the matrix Ni/Cr ratio is near the stoichiometric value for Ni_2Cr. Thus, the Pt_2Mo-type phase may precipitate at lower doses in the aged samples than in the solutionized samples, as observed in both ion and proton irradiations at 400 °C, since γ″ precipitates have to form first to decrease the matrix Ni/Cr ratio of the solutionized samples. In the

absence of imaging, whether the Pt_2Mo-type phase remained a constant size and number density or coarsened is currently unknown. The absence of Pt_2Mo-type ordered phase under ion irradiations at 300 °C may be attributed to the strong cascade mixing effect disordering the matrix even though the matrix Ni/Cr value in aged samples after irradiation is close to 2.

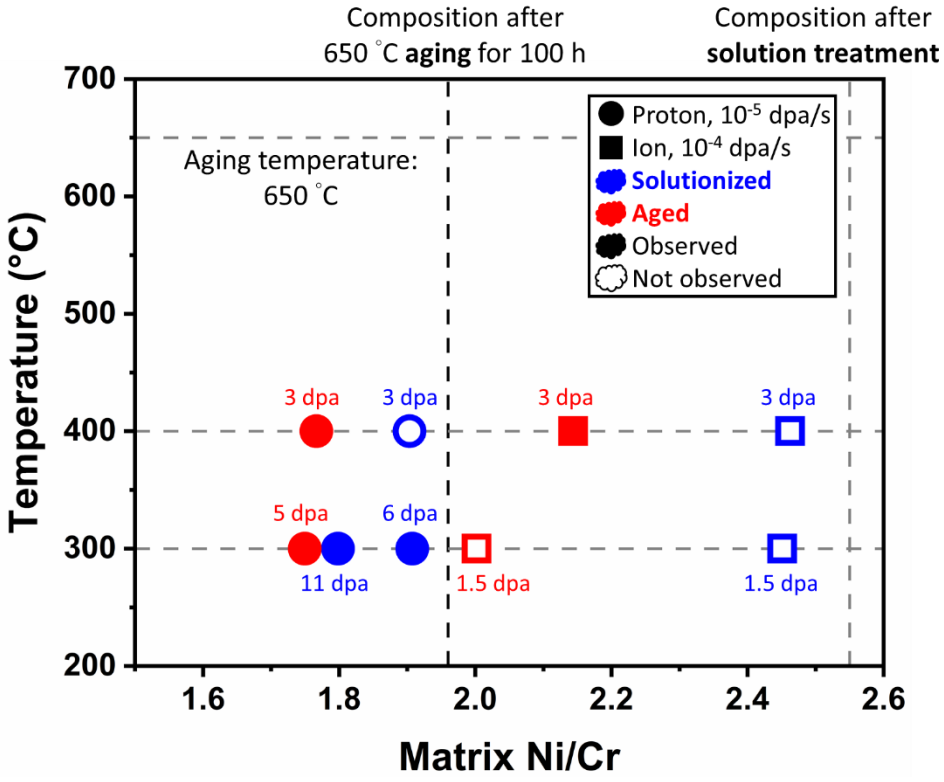

Figure 4.15. Matrix Ni to Cr concentration ratio (Ni/Cr) of solutionized (blue) and aged (red) samples after proton (circles) and ion (squares) irradiations at 300 and 400 °C. Solid symbols indicate that Pt_2Mo-type ordered phase was observed after irradiation while hollow symbols indicate that this phase was not observed.

The fourth phase that formed upon irradiation was identified as Ni_3Si with embryos in the form of Si-rich clusters. Their formation is consistent with radiation-induced segregation enabling precipitation, since the low Si concentration (<0.1 at.%) compared to the theoretical equilibrium

solubility of Si in Ni-Cr, Ni-Fe, and Ni-Mo alloy systems at 300 °C [164] excludes a thermodynamic driving force for precipitation. Generally, radiation-induced precipitation of Ni_3Si occurs near defect sinks, following the migration of interstitial-Si complexes toward defect sinks [57, 60-62]. While Si-rich clusters/Ni_3Si precipitates appeared to form homogeneously in the matrix (**Figure 4.8**), the presence of pre-existing defects cannot be ruled out. P and Cr appeared to enrich at some Ni_3Si precipitate cores (**Figure 4.9c**), possibly because of the strong binding of P with self-interstitial clusters (mostly Ni and Cr in this alloy since they are major elements) [165, 166] before the growth of Ni_3Si precipitates.

In summary, our experiments strongly suggest that within the irradiation conditions tested here, while the starting microstructures (annealed versus aged) may influence the phase decomposition pathways, the high dose microstructures developing in Alloy 625 Plus are independent from the alloy initial microstructure, but are strongly dependent on irradiation dose rate and temperature. The conditions favoring the formation of the Pt_2Mo-type and γ″ phases are summarized in **Figure 4.16**. Both phases were observed at 300 and 400 °C at and below the dose rate of 10^{-5} dpa/s. Thus, considering the significantly lower cascade mixing rates under neutron irradiation, both phases may also be expected under operating reaction conditions. In addition, due to the significantly lower cascade mixing rate, precipitate coarsening, rather than a steady state regime, may be expected.

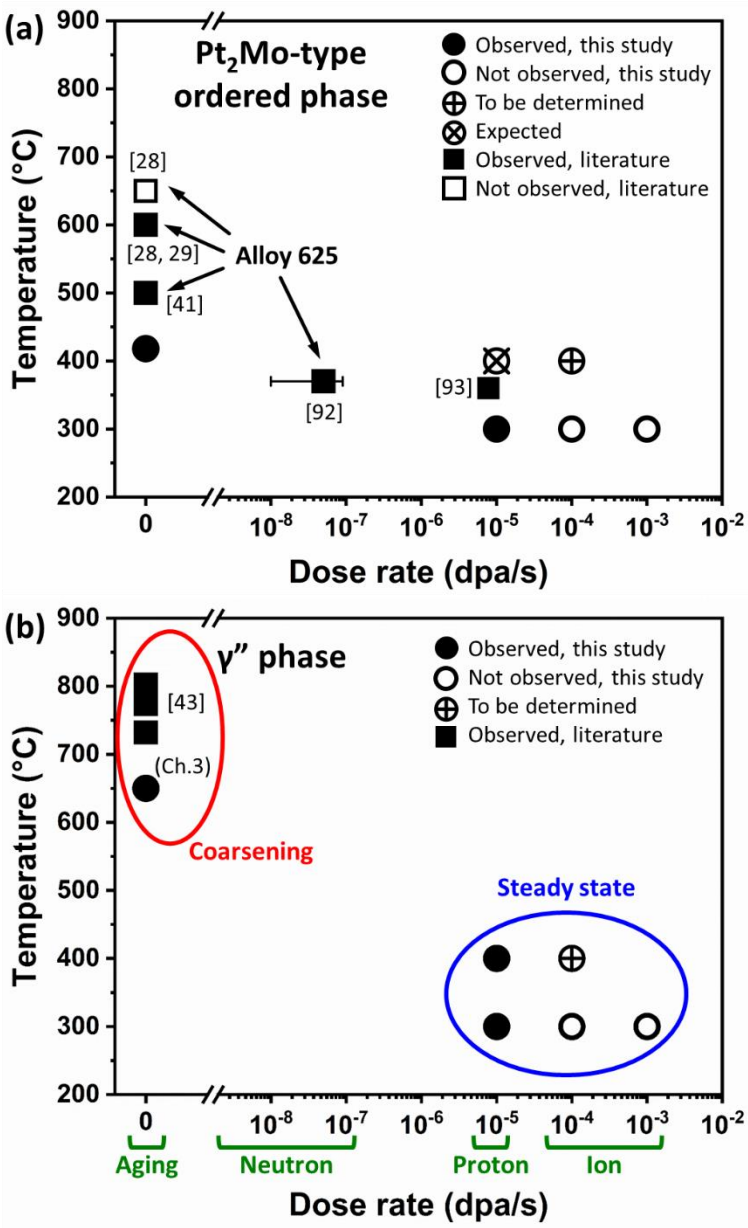

Figure 4.16. Temperature versus dose rate plots showing the conditions favoring the formation of (a) Pt_2Mo-type ordered phase, and (b) γ″ phase in Alloy 625 Plus under irradiations and thermal aging conditions. Alloy 625 data points were added in (a) for comparison. Circles indicate the data points from this study and squares represent the data points from the literature.

4.5 Conclusions

The precipitation behavior of Alloy 625 Plus under proton (dose rate: 10^{-5} dpa/s) and ion

(dose rate: 10^{-4} dpa/s) irradiations at 300 and 400 °C using solutionized and aged samples was quantified using TEM and APT. The main findings are summarized as follow:

- Precipitation of the γ″, γ′, and Pt_2Mo-type ordered phases is controlled by the interplay between cascade mixing and radiation-enhanced diffusion.
- Cascade mixing dominates under ion irradiation at dose rates above 10^{-4} dpa/s at 300 °C, leading to complete dissolution of precipitates in the aged samples.
- Under proton irradiations within 300 to 400 °C, the alloy microstructures develop non-equilibrium steady state nanoscale patterning that is a function of temperature.
- Diffusion dominated coarsening is expected to occur at dose rates below 10^{-5} dpa/s and temperatures above 400 °C.
- The formation of γ″ precipitates favors the formation of Pt_2Mo-type ordered phase, by lowering the matrix Ni/Cr ratio.

Chapter 5

Microstructural Evolution in Alloy 625 and Alloy 690 under Irradiation

5.1 Introduction

The service lifetime extension of current light water reactors (LWRs) and the operational conditions of future advanced reactors that include higher irradiation damage level, higher temperature thermal exposure, and more aggressive corrosion, place greater burdens on reactor structural components [5, 6]. Thus, materials that can endure these harsh service conditions are indispensable for maintaining safe reactor operation. Several commercial Ni-based alloys have been selected as candidate materials owing to their high temperature mechanical properties and corrosion resistance [7, 10, 12]. Particularly, Alloy 625 and Alloy 690 are in consideration for use as core internals in LWRs with extended lifetime, and for use as cladding materials in supercritical water reactors [10, 12].

The thermal aging behavior of Alloy 625 and Alloy 690 is already documented. As described in **Chapter 3** and in [25, 34], Alloy 625 can be strengthened by the precipitation of the body-centered tetragonal γ″ Ni_3(Nb, Mo, Ti, Al) phase after thermal aging within 550 to 750 °C. The body-centered orthorhombic Pt_2Mo-type ordered phase was also observed after prolonged thermal aging (longer than 50,000 h) at 500 to 600 °C [28, 29, 41]. Above 650 °C, this phase was unstable and dissolved [28, 29]. Alternatively, Alloy 690 is not a precipitation-strengthened alloy. However,

it is also susceptible to the formation of Pt_2Mo-type ordered phase that was reported after thermal aging at 420 °C for 70,000 h [46]. At lower temperatures (~360 °C), kinetics are very slow and no ordering was observed after aging for up to 90,000 h [46, 47].

Few studies reported the precipitation behavior of these two alloys under irradiation. Under neutron irradiation at ~370 °C, pre-existing γ″ precipitates partially dissolved [23, 87], and the Pt_2Mo-type ordered phase formed in Alloy 625 [23, 87, 92]. Under proton irradiation at the dose rate of ~9×10^{-6} at 360 °C, the Pt_2Mo-type phase was also observed [93]. In Alloy 690, proton irradiation at 360 °C enhanced the formation of Pt_2Mo-typd ordered phase [93], and Al clusters, Ti clusters, and Si clusters were also observed [130].

In **Chapter 3**, we compared the thermal aging behavior of Alloy 625 with Alloy 625 Plus, whose composition is similar to that of Alloy 625, and reported different precipitation behaviors. To further elaborate the potential effects of alloy composition on irradiated microstructures, this chapter clarifies and compares the precipitation behavior of Alloy 625 and Alloy 690 under irradiation with that of Alloy 625 Plus, as already described in **Chapter 4**, and suggests possible mechanisms.

5.2 Materials and methods

Alloy 625 (heat number 602051) was provided by Carpenter Technology Corporation with the heat treatment of annealing at 955 °C for 0.5 h and then water quenching. Alloy 690 (heat number NX7075HK) was obtained from Huntington Alloy Corporation with the heat treatment of annealing at 1038 °C for 2 h 40 min and then air cooling. The compositions measured by atom probe tomography (APT) are listed in **Table 5.1**. Subsequent heat treatments on both as-received

Alloy 625 and Alloy 690 at both 330 and 418 °C for 10,000 h were conducted in order to investigate their long-term aged microstructures.

Table 5.1. APT measured chemical compositions (at.%) of Alloy 625 and Alloy 690.

	Ni	Cr	Mo	Fe	Nb	Ti	Al	Si	Co	Mn	P	S	C
Alloy 625	61.6	26.1	5.48	3.77	2.16	0.29	0.33	0.15	0.01	0.06	<0.01	-	0.03
Alloy 690	56.6	31.9	-	10.4	-	0.33	0.45	0.12	0.02	0.17	<0.01	-	0.04

Alloy 625 and Alloy 690 samples for irradiation were sectioned into small pieces, and solution treated at 1100 °C for 1 h in Ar filled quartz tubes, followed by water quenching. Sample surfaces were electropolished at -30 °C in a 10% perchloric acid + 90% methanol electrolyte at 30 V. Stopping and Range of Ions in Matter (SRIM) calculation [160] was performed to estimate the damage level using Kinchin–Pease model [48, 161] using the displacement energy of 25 eV [162]. Proton irradiations were performed at the Michigan Ion Beam Laboratory using a 2 MeV proton beam at the approximate dose rate of 10^{-5} dpa/s at 300 °C to 1.5, 6, and 11 dpa for both Alloy 625 and Alloy 690, and at 400 °C to 3 dpa for Alloy 690. Some Alloy 625 samples were aged at 650 °C for 25 h after solution treatment, and subsequently proton irradiated at 300 °C to 5 dpa in order to investigate the γ″ precipitate evolution under irradiation. The depth of around 2 to 3 μm below the irradiated sample surfaces was chosen for transmission electron microscopy (TEM) and APT specimen preparation and analysis.

TEM and APT specimens were prepared using a standard lift-out process on both Thermo Fisher Nova 200 and Thermo Fisher Helios 650 Nanolab dual scanning electron microscope

(SEM)/focused ion beam (FIB) instruments. TEM specimens were characterized using both JEOL 3011 TEM and Thermo Fisher Talos F200X G2 TEM. APT data were collected on both CAMECA LEAP 4000X HR and 5000 XR instruments operated in laser mode using a pulse energy range of 30 to 50 pJ, 200 kHz pulse rate, and target detection rate of 0.5% at 50 K. APT data were reconstructed and analyzed using the IVAS 3.8.4 software. The radius evolution of the reconstructed datasets was based on voltage evolution using the evaporation field of Ni (35 nm/V [144]). The image compression factor (ranged between 1.4 and 1.8) and field factor k_f (ranged between 2.7 and 3.4) were adjusted to ensure uniform atomic density throughout a dataset.

5.3 Results

5.3.1 Microstructures of Alloy 625 after thermal treatments

In the as-received condition, Alloy 625 exhibited solid solution, as evidenced by the TEM diffraction pattern (DP) showing only the face-centered cubic (FCC) γ matrix spots (**Figure 5.1a**). No precipitates were observed in the matrix even after aging at 330 °C for 10,000 h (**Figure 5.1b**). However, after aging at 418 °C for 10,000 h, the Pt_2Mo-type phase precipitated, as indicated by the corresponding superlattice diffraction spots at {2/3 2/3 0}, {4/3 4/3 0}, and {2/3 4/3 0} positions in the <0 0 1>-zone TEM DP and the TEM dark-field (DF) image (**Figure 5.1c**). A solution treatment at 1100 °C for 1 h was sufficient to create a solid solution, as indicated by APT ion maps showing elemental uniform distributions, and by the TEM DP showing only the γ matrix spots (**Figure 5.1d**). As already discussed in **Chapter 3**, following thermal aging at 650 °C for 25 h, γ″ precipitates formed, as illustrated by the superlattice spots at {1 0 0}, {1 1/2 0}, and {1 1 0} positions in the < 0 0 1 > -zone TEM DP, and by the Nb and Ti partitioning in the APT ion maps

(**Figure 5.1e**).

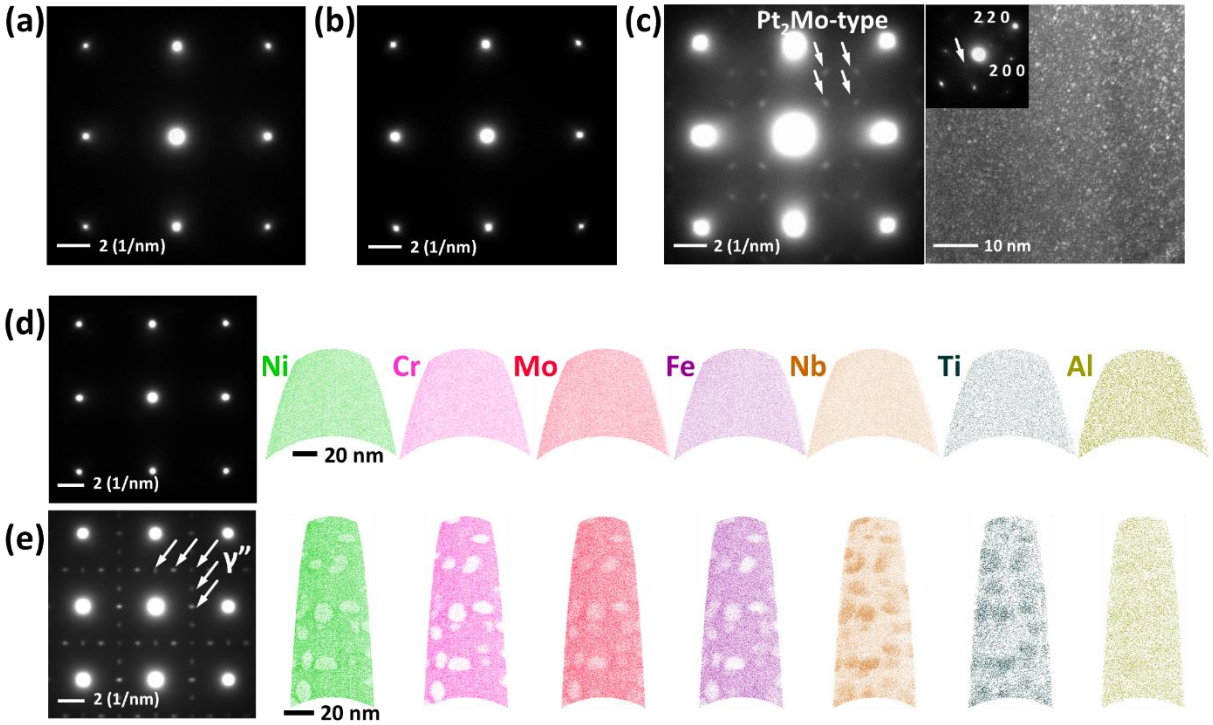

Figure 5.1. <0 0 1>-zone TEM DPs of Alloy 625 (a) in as-received condition, and (b) after aging at 330 °C for 10,000 h. (c) TEM DP (left) and TEM DF image (right) showing the Pt_2Mo-type ordered precipitates in Alloy 625 after aging at 418 °C for 10,000 h. The inset DP indicates the diffraction condition, and (-2/3 -2/3 0) superlattice diffraction spot (indicated by the white arrow) is selected for DF imaging. <0 0 1>-zone TEM DP and APT ion maps and of Alloy 625 after (d) solution treatment at 1100 °C for 1 h, and (e) after aging at 650 °C aging for 25 h. The thicknesses of ion map slices are 1, 2, 10, 10, 20, 20, and 20 nm for Ni, Cr, Mo, Fe, Nb, Ti, and Al, respectively, and the same thicknesses will be used in this chapter.

5.3.2 Proton-irradiated microstructures of Alloy 625

Pt_2Mo-type precipitates, Al-rich clusters, Si-rich clusters, and Si segregation were observed in solutionized Alloy 625 samples after proton irradiation at 300 °C (**Figure 5.2**). Electron

diffraction revealed the formation of the Pt_2Mo-type phase at all three doses (1.5, 6, and 11 dpa). No evidence for γ″ superlattice diffraction spots could be found through the analysis of the intensity of the TEM DPs. After 6 and 11 dpa, the spatial distribution of Al-rich clusters was non-uniform. Regions depleted of Al-rich clusters were observed near the Si-rich regions, as illustrated in **Figure 5.3a**. The Al-rich clusters were enriched in Ni, Al, Nb, and Ti and depleted in Cr, Mo, and Fe, as shown by the composition measurements obtained from APT datasets (**Figure 5.3b, c**). The quantitative analysis of the evolution of Al-rich clusters with irradiation dose is shown in **Figure 5.4**. A few Nb-rich regions were also noticed in the APT ion maps (**Figure 5.2b, c**). By comparing with the distribution of the other elements, these regions appeared to correspond to the locations of small cavities (indicated by the black arrows in **Figure 5.2b, c** and discussed below) or Al-rich clusters that are enriched in Nb (indicated by the blue arrows in **Figure 5.2c**). Other than the sparse Nb-rich regions, clustering of Nb and Ti remained faint, as indicated by the low amplitudes of the Nb and Ti RDFs (**Figure 5.4a**).

High atomic density regions were revealed by 2D density plots of APT ion maps (**Figure 5.5**), and by iso-density surfaces in **Figure 5.6a**. Note that the measured density in these regions, i.e. ~146 atom/nm^3 is unphysical – the atomic density of Alloy 625 is expected to be about 83 atom/nm^3. Although perhaps counter-intuitively, these high density regions reflect the presence of nanoscale cavities that formed during irradiation. Significant ion trajectory aberrations caused by a focusing electric field above the cavities can explain the accumulation of ions in the reconstructions [167-169]. Detailed cavity size and number density information quantified by TEM will be summarized in **Chapter 6**.

The distribution of Si revealed Si-rich clusters and segregation along linear features, assumed to be dislocations. The Si-rich clusters had an average radius of ~1.6 ± 0.6 nm at 1.5 dpa, and

became slightly larger as dose increased with an average radius ~2.0 ± 0.9 nm at 11 dpa (**Figure 5.2**). At 1.5 dpa, the Si-rich features are too small to be identified as Si-rich clusters or small dislocation loops decorated with Si. At 6 and 11 dpa, the Si-rich clusters were either near Si-decorated line features or isolated (**Figure 5.2** and **Figure 5.6a**), and their average composition was close to that of the Ni_3Si (**Figure 5.6b**). Dislocation loops are enriched in Ni and Si but depleted in Cr, Mo, and Fe (**Figure 5.6c**).

Aged Alloy 625 samples also exhibited precipitation of the Pt_2Mo-type ordered phase, Al clustering, Si clustering, and Si segregation after proton irradiation at 300 °C to 5 dpa (**Figure 5.7**). The absence of γ″ superlattice spots in the TEM DP indicated the disordering of pre-existing γ″ precipitates. RDF analysis showed the decrease of the Nb and Ti amplitudes (**Figure 5.4**), which is consistent with the dissolution of pre-existing γ″ precipitates.

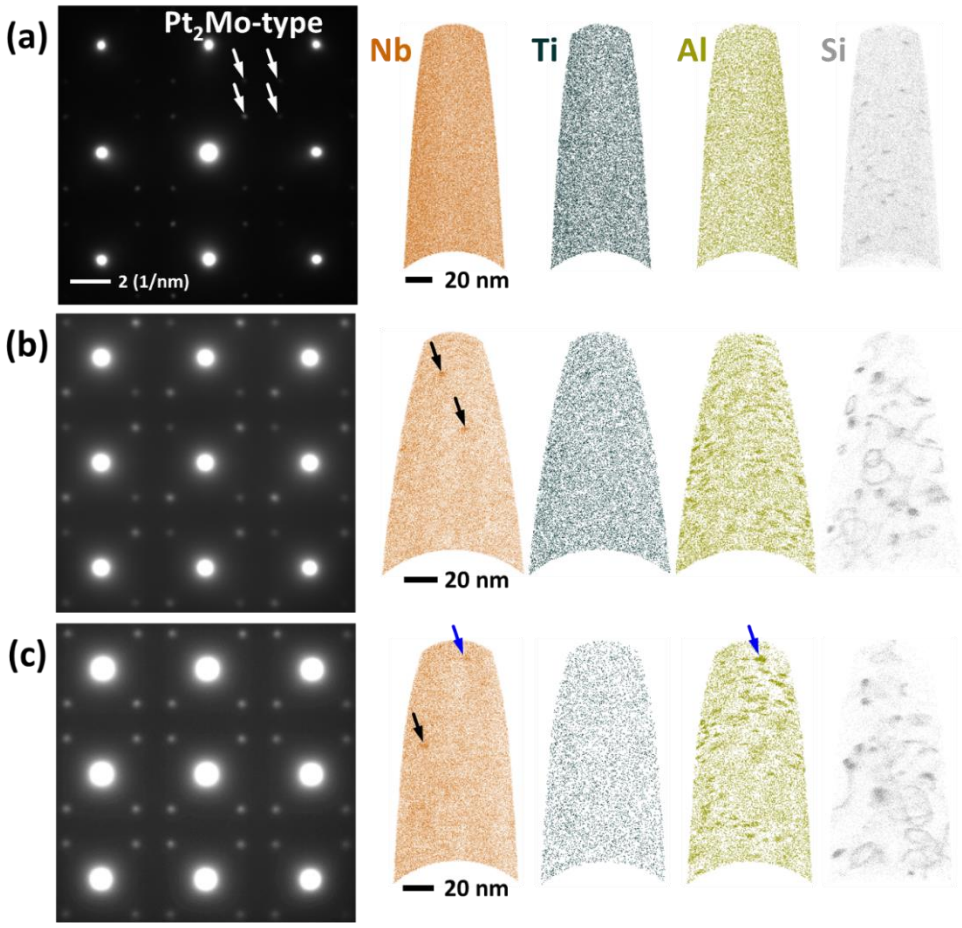

Figure 5.2. <0 0 1>-zone TEM DPs and APT ion maps of Alloy 625 after proton irradiation at 300 °C to (a) 1.5, (b) 6, and (c) 11 dpa. Si ion maps correspond to the entire datasets rather than slices. The black arrows indicate high atomic density regions, and the blue arrow indicate an Al-rich cluster.

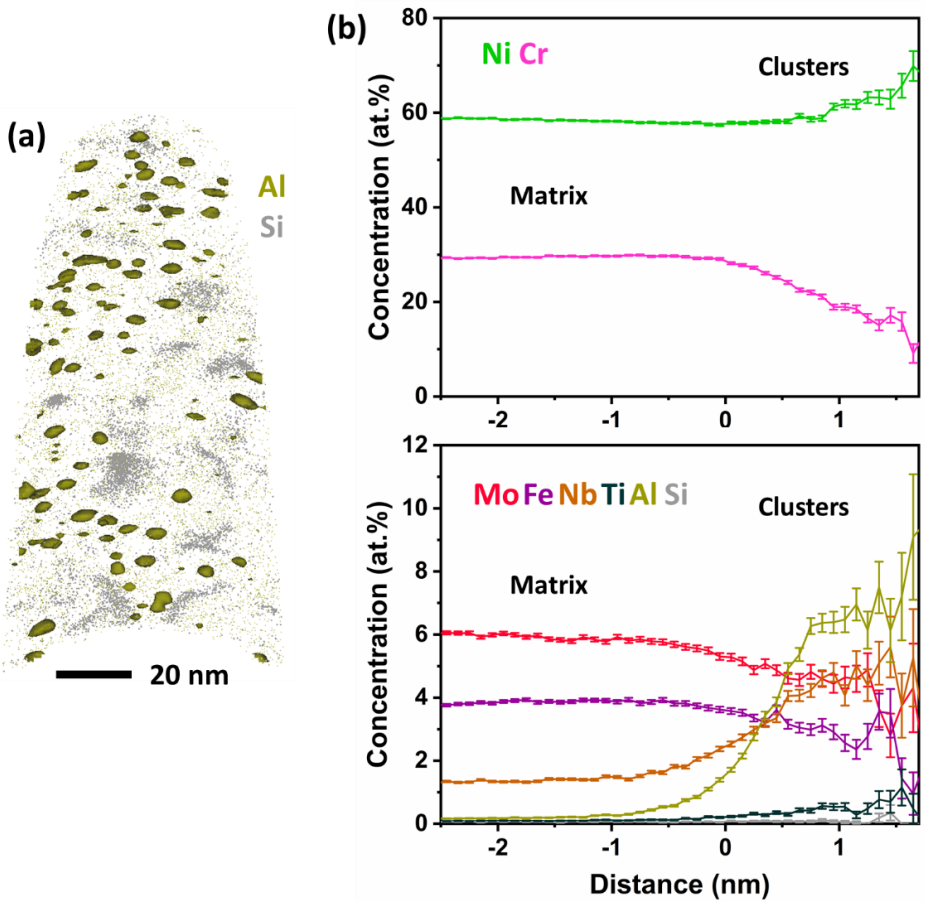

Figure 5.3. (a) 15-nm slice APT ion map of proton-irradiated Alloy 625 at 300 °C to 11 dpa, showing the spatial distribution of Al-rich clusters. (b)-(c) Proxigrams of Al-rich clusters calculated from Al = 1.2 at.% iso-concentration surfaces.

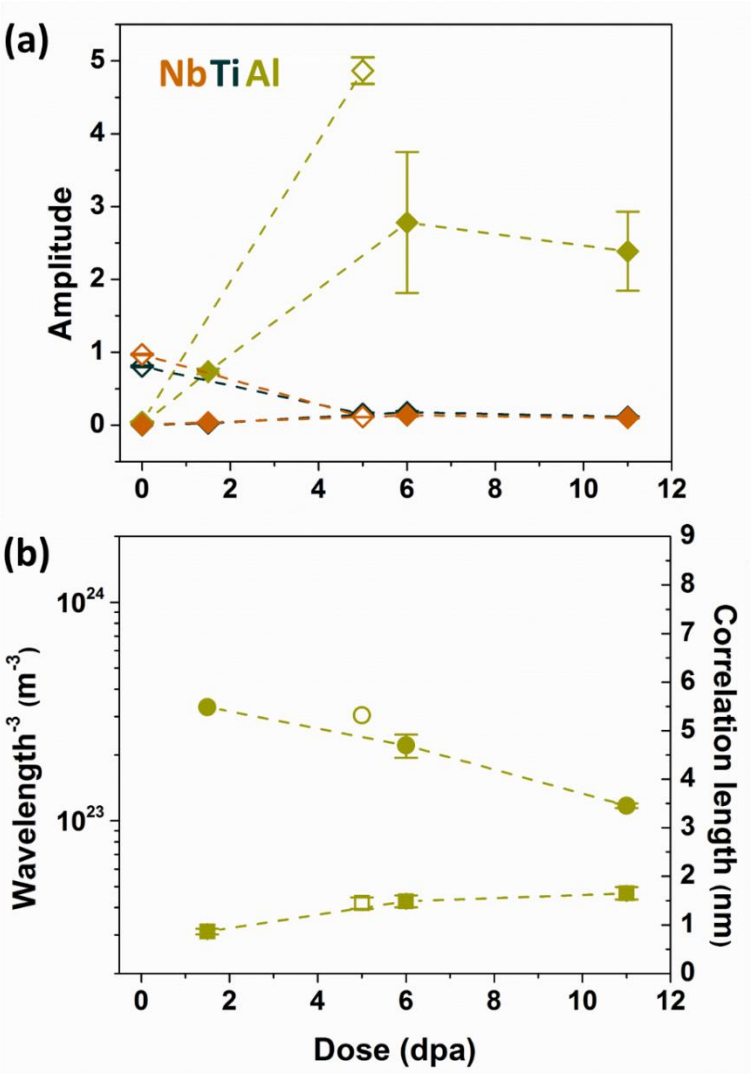

Figure 5.4. (a) The evolution of concentration fluctuation amplitude (diamonds) of Nb, Ti, and Al in Alloy 625 after proton irradiation for solutionized (solid symbols) and aged (hollow symbols) conditions. (b) The evolution of wavelength (disks) and correlation length (squares) of Al in Alloy 625 after proton irradiation for solutionized (solid symbols) and aged (hollow symbols) conditions.

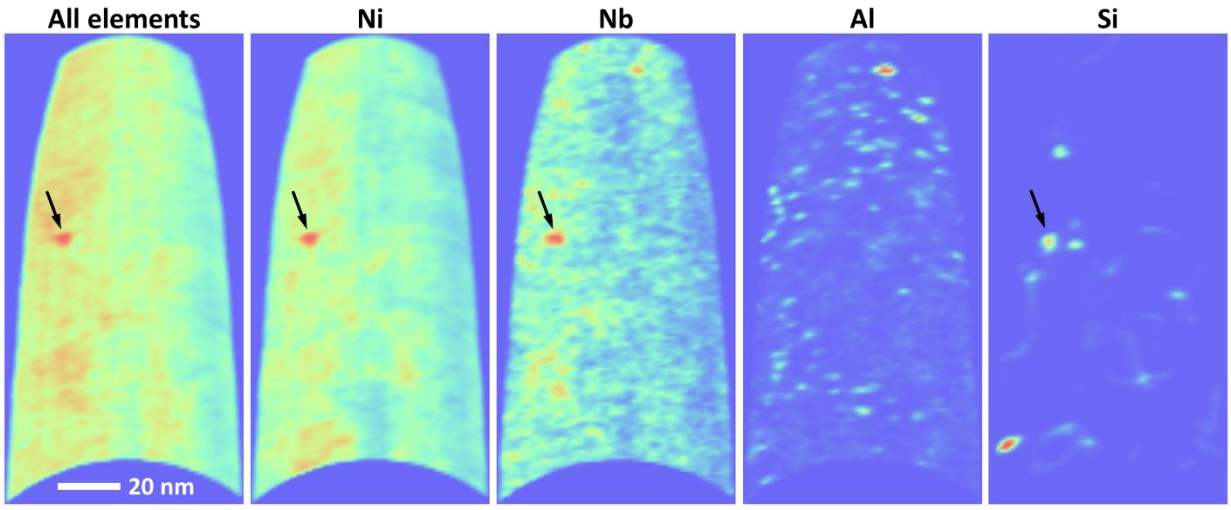

Figure 5.5. 2D density plots of 20-nm slices APT ion maps of (a) all elements, (b) Ni, (c) Nb, and (d) Si in Alloy 625 after proton irradiation at 300 °C to 11 dpa, showing the locally high atomic density regions (indicated by the black arrows).

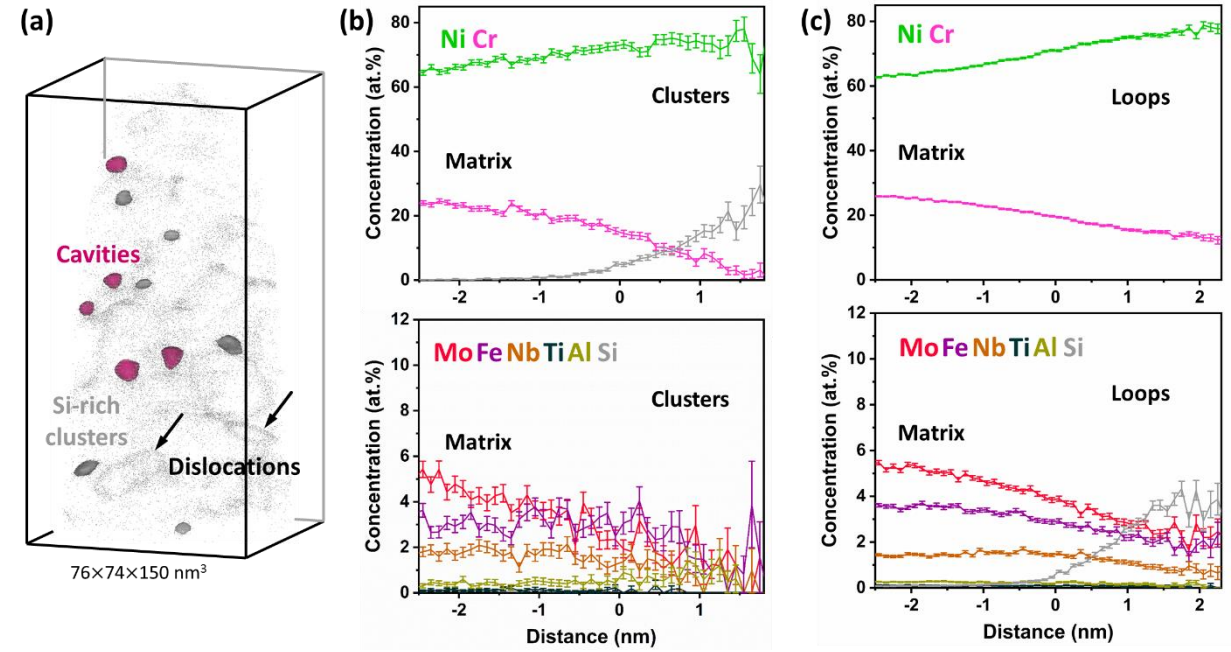

Figure 5.6. (a) APT ion map of proton-irradiated Alloy 625 at 300 °C to 11 dpa, showing the spatial distribution of Si-rich clusters, delineated by the gray Si = 3.9 at.% iso-concentration surfaces. Cavities are presented by the dark pink 76 atom/nm^3 iso-density surfaces to distinguish from Si-rich clusters. Dislocations are pointed out by the black arrows. (b) Proxigrams of Si-rich clusters calculated from Si = 3.9 at.% iso-concentration surfaces. (c) Proxigrams of dislocation loops calculated from Si = 0.8 at.% iso-concentration surfaces.

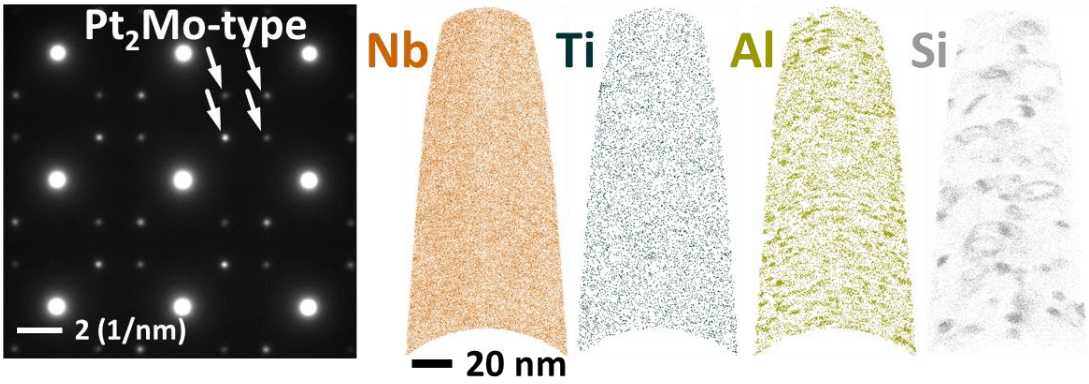

Figure 5.7. <001>-zone TEM DP and APT ion maps of Alloy 625 after 650 °C aging for 25 h + proton irradiation at 300 °C to 5 dpa.

5.3.3 Microstructures of Alloy 690 after thermal treatments

The as-received Alloy 690 was a solid solution (**Figure 5.8a**). After thermal aging at both 330 and 418 °C, no precipitates were observed, as evidenced by the TEM DPs showing only the γ matrix spots (**Figure 5.8b, c**). APT ion maps and TEM DP confirmed the absence of solute clustering or precipitates in solutionized Alloy 690 (**Figure 5.8d**).

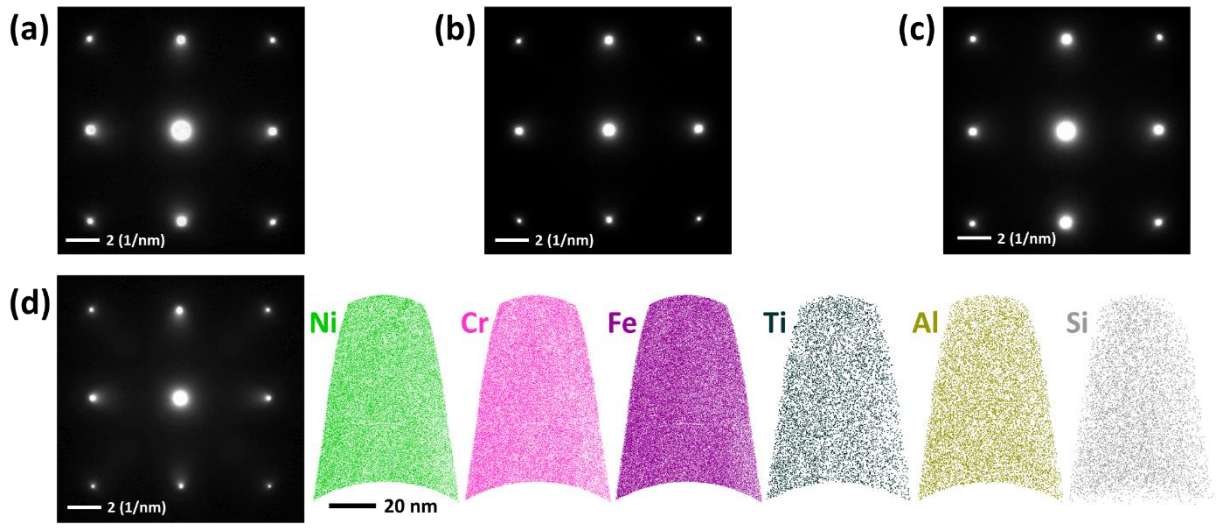

Figure 5.8. TEM DPs of Alloy 690 (a) in as-received condition, (b) after aging at 330 °C for 10,000 h, and (c) after aging at 418 °C for 10,000 h. (d) <0 0 1>-zone TEM DP and APT ion maps of Alloy 690 after solution treatment at 1100 °C for 1 h.

5.3.4 Proton-irradiated microstructures of Alloy 690

Proton irradiation at 300 °C caused the formation of the Pt_2Mo-type phase, Al-rich clusters, Si-rich clusters, and Si-decorated dislocation loops. The superlattice diffraction spots of the Pt_2Mo-type phase were present from 1.5 to 11 dpa (**Figure 5.9**). The intensities of these spots appeared to be weaker than those of Alloy 625 under the same irradiation condition. APT ion maps showed spatial coincidence of the Al and Ti clusters (hereafter called Al-rich clusters). The clusters evolved from a fine scale and uniform distribution at 1.5 dpa to a larger size and non-uniform distribution as dose increased to 11 dpa (**Figure 5.9**). The Al-rich clusters were enriched in Ni, Al, and Ti while depleted in Cr and Fe (**Figure 5.10a**).

After proton irradiation at 400 °C to 3 dpa, no Pt_2Mo-type superlattice diffraction spots were observed (**Figure 5.11a**). Instead, superlattice spots corresponding to the γ′ FCC $L1_2$ structure were present, as evidenced by the intensity line profile of diffraction spots along [2 -2 0] direction

(**Figure 5.11b**). APT ion maps revealed Al-rich clusters that correspond to Ni_3(Al, Ti) precipitates based on the composition measurement (**Figure 5.10b**). Si-rich clusters were also observed and their composition was consistent with that of Ni_3Si precipitates (**Figure 5.12**). Several Si-rich clusters exhibited P and Cr enrichment at the precipitate core, and Al and Ti segregation at the precipitate/matrix interface (**Figure 5.12b**).

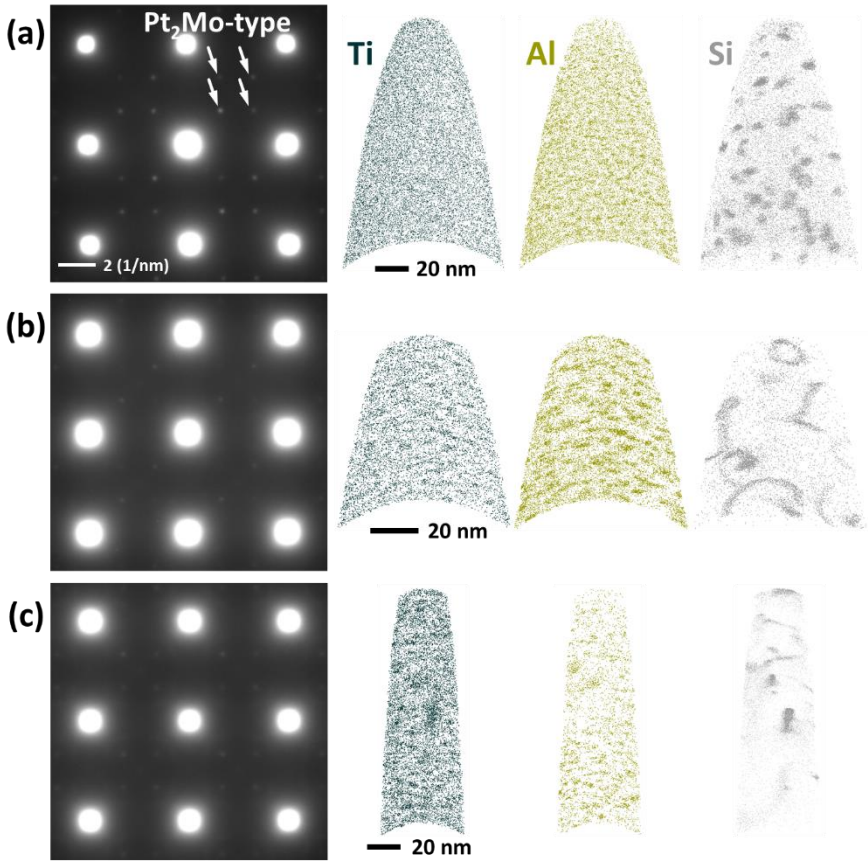

Figure 5.9. <0 0 1>-zone TEM DPs and APT ion maps of Alloy 690 after proton irradiation at 300 °C to (a) 1.5, (b) 6, and (c) 11 dpa.

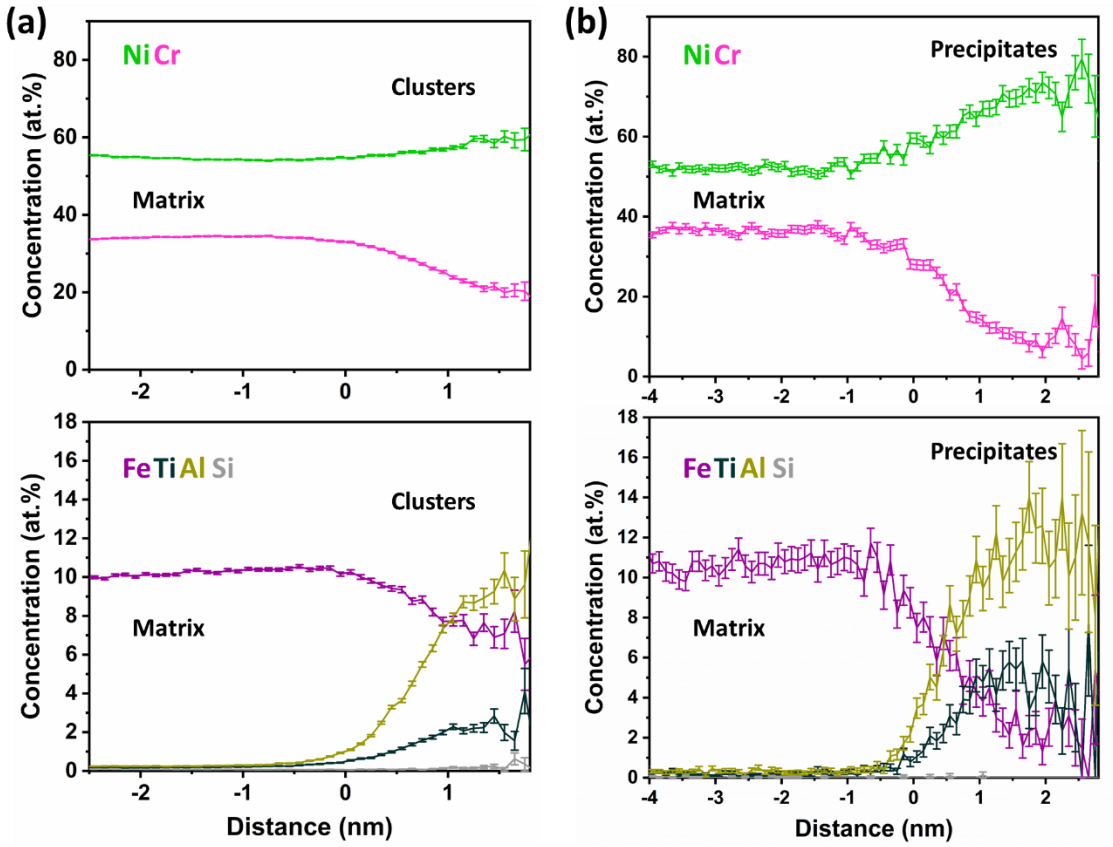

Figure 5.10. (a) Proxigrams of Al-rich clusters, generated from Al = 1.2 at.% iso-concentration surfaces, in Alloy 690 after proton irradiation at 300 °C to 6 dpa. (b) Proxigrams of γ′ precipitates, generated from Al = 3 at.% iso-concentration surfaces, in Alloy 690 after proton irradiation at 400 °C to 3 dpa.

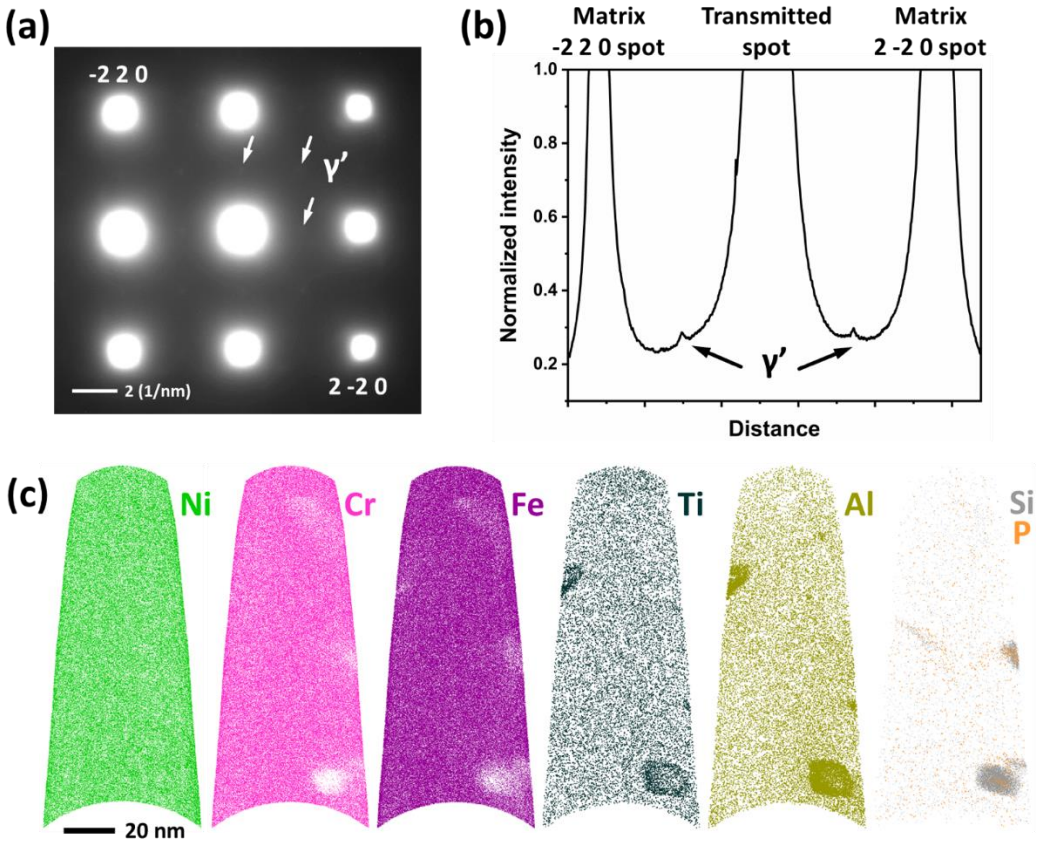

Figure 5.11. (a) TEM DP of Alloy 690 after proton irradiation at 400 °C to 3 dpa. (b) Intensity line profile of TEM DP in (a) across matrix -2 2 0 spot, transmitted spot, and matrix 2 -2 0 spot, showing the presence of γ′ superlattice diffraction spots. (c) APT ion maps of Alloy 690 after proton irradiation at 400 °C to 3 dpa.

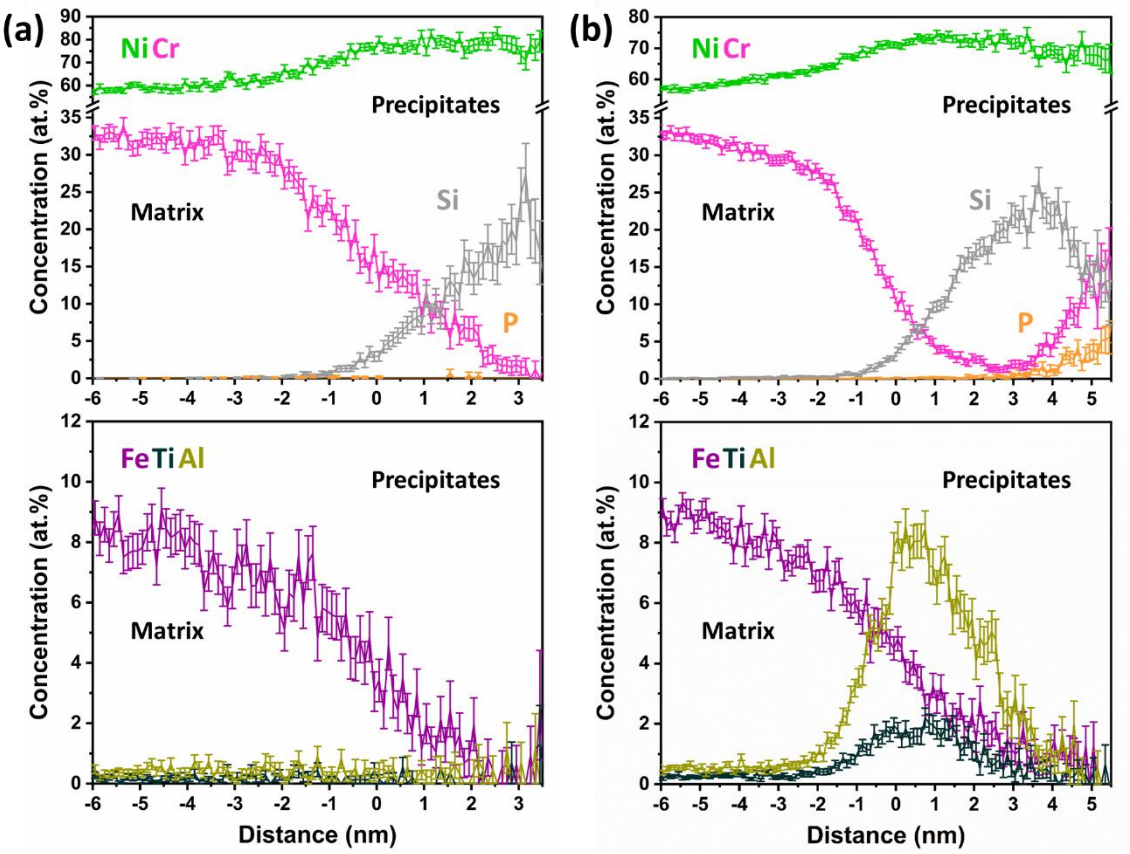

Figure 5.12. Proxigrams of (a) Ni_3Si precipitates, generated from Si = 4 at.% iso-concentration surfaces, and (b) Ni_3Si precipitates with Al and Ti segregation at precipitate/matrix interface in Alloy 690 after proton irradiation at 400 °C to 3 dpa.

5.4 Discussion

Under thermal aging conditions, Thermocalc calculations suggest that in Alloy 625 the δ phase is the equilibrium phase and the γ″ phase is metastable (**3.4**). Experimentally, the δ phase has been observed after thermal aging between 650 to 900 °C [34, 35] and the γ″ phase has been observed when aging within 550 to 750 °C [25, 33, 34]. The Pt_2Mo-type ordered phase was also reported in Alloy 625 after prolonged aging between 500 and 600 °C [28, 29, 41], but dissolved above 650 °C [28, 29]. Our results here showed that the Pt_2Mo-type phase can form at lower temperatures, i.e. 418 °C, but requires a long aging time, 10,000 h (**Figure 5.1c**). The absence of

this phase after aging at an even lower temperature, 330 °C, is attributed to slow kinetics hindering its formation despite the very long aging time of 10,000 h.

In Alloy 690, the γ″ and δ phases do not form due to the absence of Nb. While Thermocalc predictions (**Figure 5.13**) suggested that γ′ Ni_3(Ti, Al) is a stable phase, it was not experimentally observed in Alloy 690 under thermal aging. Indeed, Alloy 690 remained as FCC γ solid solution after long-term aging at 330 and 418 °C (**Figure 5.8b, c**), which suggests that slow diffusion kinetics impede the formation of any phases. The Pt_2Mo-type phase was not observed at 330 and 418 °C either. While slow ordering kinetics might also be at play, particularly at 330 °C, we believe thermodynamic destabilization is happening at 418 °C. A previous study showed that the order-disorder transformation temperature in a Ni-30Cr-10Fe (at.%) alloy, whose composition is similar to the Alloy 690 composition used in this study, is around 400 °C [38]. Furthermore, the addition of Nb and Mo in Ni-Cr-based alloys was found to stabilize the Pt_2Mo-type phase to higher temperatures [170, 171]. Therefore, observations of Pt_2Mo-type phase in Alloy 625 and Alloy 625 Plus, which both contain Nb and Mo, aged at 418 °C (**Figure 5.1c** and **Chapter 4**) but not in Alloy 690 are qualitatively consistent with the literature.

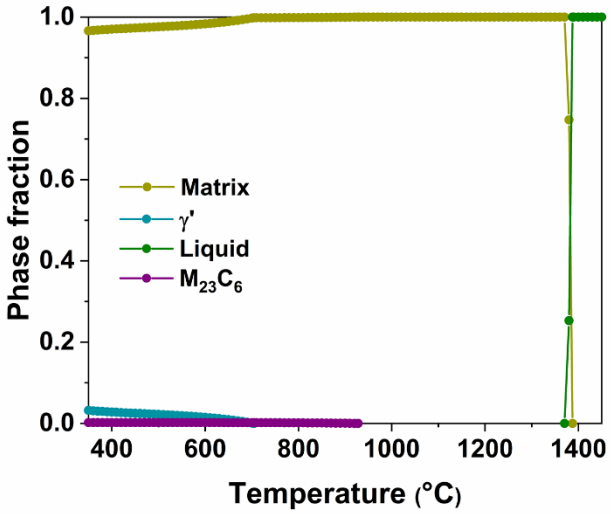

Figure 5.13. Equilibrium phase fraction in Alloy 690 calculated using Thermocalc software with TCNI10 database.

Compared to the absence of the Pt_2Mo-type phase after thermal aging at 330 °C, its presence after proton irradiation at 300 °C in both Alloy 625 and Alloy 690 strongly suggests a radiation-enhanced ordering mechanism, in agreement with previous observations [93]. Alloy 690 did not exhibit the Pt_2Mo-type phase formation after proton irradiation at 400 °C, which is consistent with its absence after aging at 418 °C and further supports the lack of thermodynamic stability of this phase at that temperature range.

Al-rich clusters that formed under proton irradiation at 300 °C in Alloy 625 were enriched in Ni, Al, Ti, and Nb, suggesting these clusters may be the precursors of γ′ Ni_3(Al, Ti, Nb) precipitates. However, no γ′ superlattice diffraction spots (FCC $L1_2$ structure) were observed. The γ′ Ni_3(Al, Ti, Nb) phase has never been reported in Alloy 625 under thermal aging. Thus, whether the formation mechanism of these Al-rich clusters is radiation-enhanced or radiation-induced remains unclear. At 11 dpa, regions without Al clusters were noted near the Si-dense regions that correspond to dislocation loops or cavities (**Figure 5.3a**). The formation of Ni_3Al precipitate free zone near

defect sinks was observed in irradiated Ni-Al alloys [83, 172, 173], and was explained by a mechanism related to radiation-induced segregation [83, 174]. Vacancies tend to migrate to defect sinks during irradiation. Since Al atoms are oversized and more likely to diffuse by exchanging with vacancies, an Al solute flux away from sinks is expected and can cause the development of Ni_3Al precipitate free zone near sinks. However, in our case, no obvious depletion of Al atoms near defect sinks was observed. Thus, we hypothesize that defect sinks prevent the formation of Al clusters by trapping defects nearby, locally limiting Al diffusion to clusters.

In Alloy 690, Al-rich clusters that correspond the precursor of the FCC $L1_2$ γ' Ni_3(Al, Ti) precipitates formed under proton irradiation at 300 °C without structural ordering. The missing low-temperature aging behavior of this alloy makes the clarification of radiation-enhanced or radiation-induced mechanism unresolved. After 400 °C proton irradiation, the presence of γ' diffraction spots indicates structural ordering of the precipitates, possibly due to the higher diffusion rate that counterbalance the cascade mixing effect. However, both Ni_3(Al, Ti) and Ni_3Si have the FCC $L1_2$ crystal structure. Thus, it is unknown which phase actually contributed to the superlattice spots.

γ'' precipitates, which are typically observed after thermal aging at 550 to 750 °C [25, 34], did not form in Alloy 625 after long-term thermal aging at both 330 and 418 °C. The slow kinetics is most likely responsible for the absence of this phase. A previous study showed that γ'' precipitates formed in Alloy 625 under 550 °C aging for ~1000 h [34], but no precipitation information was reported at temperature below 550 °C. In another similar Ni-based alloy, Alloy 625 Plus, the pre-existing γ'' precipitates only slightly increased in averaged long-axis (<4 nm) after aging at 330 and 418 °C for 10,000 h (**Chapter 4**), suggesting a slow diffusion rate. Under proton irradiation at 300 °C, despite the enhanced diffusion rate due to high defect concentration,

cascade mixing was sufficient to impede γ″ precipitation in the solutionized alloys (**Figure 5.2**), and destroy pre-existing γ″ precipitates in the aged alloys (**Figure 5.7**). In contrast, γ″ precipitates remained present in Alloy 625 Plus under the same irradiation condition (proton irradiation at 300 °C) (**Chapter 4**). The difference in the irradiation response is attributed to the larger γ″ precipitation driving force in Alloy 625 Plus than Alloy 625, as reported in **Chapter 3**.

Some Ni_3Si precipitates exhibited obvious segregation of Al and Ti at the precipitate/matrix interfaces in Alloy 690 (**Figure 5.12b**). Diffusion-limited pile-up mechanism could be ruled out since the diffusion rate under irradiation is significantly enhanced. In addition, the lattice parameter mismatch at Ni_3Si precipitate/γ matrix interface is about ~2.1% (the lattice parameter of Alloy 690 is ~3.577 nm after aging at 420 °C for 10,000 h [175], and Ni_3Si is ~3.504 nm [176]), which is smaller than the linear mismatch of Al and Ti in Ni (~4.7% and ~9.0%, respectively [177]). Thus, elastic interactions are thought to be negligible. RIS of Al to the Ni_3Si precipitate/matrix interfaces could be ruled out since Al is usually depleted at defect sinks in Ni-based alloys [83, 174]. Another possibility would be the heterogeneous precipitation of γ′ Ni_3(Al, Ti) on the Ni_3Si precipitate/matrix interfaces that may act as nucleation sites.

In summary, the comparisons of the irradiated microstructures of Alloy 625 and Alloy 690 with Alloy 625 Plus confirm that precipitation behavior depends on irradiation conditions and the thermodynamic properties of the alloys. Despite the compositional similarity, alloys have their own microstructural responses under irradiation.

5.5 Conclusions

The precipitation behavior of Alloy 625 and Alloy 690 under proton (dose rate: 10^{-5} dpa/s)

irradiations at 300 and 400 °C was characterized using TEM and APT. The main findings are summarized as follow:

- Unlike in Alloy 625 Plus, the γ″ phase was not observed in Alloy 625 after proton irradiation at 300 °C, which is attributed to the smaller precipitation driving force in Alloy 625 than in Alloy 625 Plus.
- The Pt_2Mo-type phase was observed in Alloy 625 and Alloy 625 Plus but not in Alloy 690 after aging at 418 °C, in agreement with the observations that Fe decreases, and Nb and Mo increases the order-disorder transformation temperature.
- Some Ni_3Si precipitates showed segregation of Al and Ti at the precipitate/matrix interfaces in Alloy 690, which could be related to the formation of γ′ Ni_3(Al, Ti).

Chapter 6

Cavity and Dislocation Loop Evolution

6.1 Introduction

Cavities and dislocation loops are common microstructural features that form during irradiation. As mentioned in **2.3.6**, cavities were observed in Ni-based alloys under irradiation at temperatures between 300 and 750 °C (**Figure 2.11**). Cavity evolution was found to be dependent on alloy composition. In binary Ni alloys under ion irradiation, the average cavity size is smaller in alloys containing larger-sized solute atoms [123], which was explained by the stronger binding energy of large-sized solute atoms with vacancies that reduces the vacancy mobility. Similarly, cavities are in smaller sizes and higher number densities in commercial 316L steels with minor addition (~0.4 at.%) of larger-sized solute atoms under electron irradiation [124]. As summarized in **2.3.7**, dislocation loops were observed in Ni-based alloys under irradiations at temperatures up to 700 °C (**Figure 2.12**). The dislocation structures developed under irradiation can be altered by solute atoms. Dislocation loops were observed in smaller sizes and higher number densities in binary Ni alloys containing larger solute atoms, which is mainly attributed to the trapping of interstitials by large-sized solute atoms, leading to a higher migration barrier for interstitials [123]. Based on these findings above, we hypothesize that in commercial Ni-based alloys with higher concentrations of large-sized solute atoms, cavities and dislocation loops would be in smaller sizes and higher number densities. To test the hypothesis, we characterized the cavity and dislocation loop structures in three commercial Ni-based alloys (Alloy 625, Alloy 625 Plus, and Alloy 690)

after proton irradiation at 300 °C to dose up to 11 dpa. We also characterized the microstructure of Alloy 690 after proton irradiation at 400 °C to elucidate the role of temperature on cavity and dislocation loop evolutions.

6.2 Materials and methods

Alloy 625, Alloy 625 Plus, and Alloy 690 were solution treated at 1100 °C for 1 h and then water quenched before irradiation. Proton irradiations were conducted at 300 °C to 1.5, 6, and 11 dpa, and at 400 °C to 3 dpa at the dose rate of 10^{-5} dpa/s. The detailed procedures of sample preparation and irradiation can be found in **4.2**. TEM specimens were characterized on a JEOL 3011 high resolution TEM, and bright-field (BF) scanning transmission electron microscopy (STEM) images were obtained using a JEOL 2100F microscope. Cavities were characterized using an under-focus imaging condition. The local samples thickness for number density calculation was estimated using convergent beam diffraction (CBED) method. Volumetric swelling was estimated from the total volume of the cavities divided by the volume of the sample, assuming the cavities were spheres.

6.3 Results

6.3.1 Alloy 625

Cavities were observed at all three doses (1.5, 6, and 11 dpa) after proton irradiation at 300 °C (**Figure 6.1a-c**). The distribution of cavity diameters is displayed in **Figure 6.1d**. Only few cavities were observed due to the low cavity number density at 1.5 dpa, so the distribution of cavity

diameters at 1.5 dpa was not included. From 6 to 11 dpa, the average cavity diameter remained constant (from 6.1 ± 1.4 to 6.2 ± 1.8 nm), and the distribution ranges of cavity diameters were nearly identical. The number density of cavities increased considerably as dose increased from 1.5 to 6 dpa (from 0.14 to 12.2 ± 1.7 $\times 10^{21}$ m^{-3}), and slightly increased as dose reached to 11 dpa (18.9 ± 1.5 $\times 10^{21}$ m^{-3}). The volumetric swelling was 0.3 ± 0.03% at 11 dpa.

Faulted dislocation loops were quantified using the rel-rod dark-field imaging condition [178] (**Figure 6.1e-g**). This imaging method can only observe dislocation loops lying on {1 1 1} crystallographic planes with Burgers vector of 1/3<1 1 1>. Additionally, only one quarter of the total number of the 1/3<1 1 1> type dislocation loops can be imaged for a given diffraction condition. Thus, the number density of dislocation loops was estimated by multiplying a factor of 4. This correction assumes that the numbers of dislocation loops on each of the {1 1 1} crystallographic planes are equivalent and no other potential artefacts associated with dislocation loop imaging affected the measurements [178]. The distribution of dislocation loop diameters became broader with increasing doses (**Figure 6.1h**). The average diameter and number density of cavities and dislocation loops as a function of dose are summarized in **Table 6.1** and **Table 6.2**.

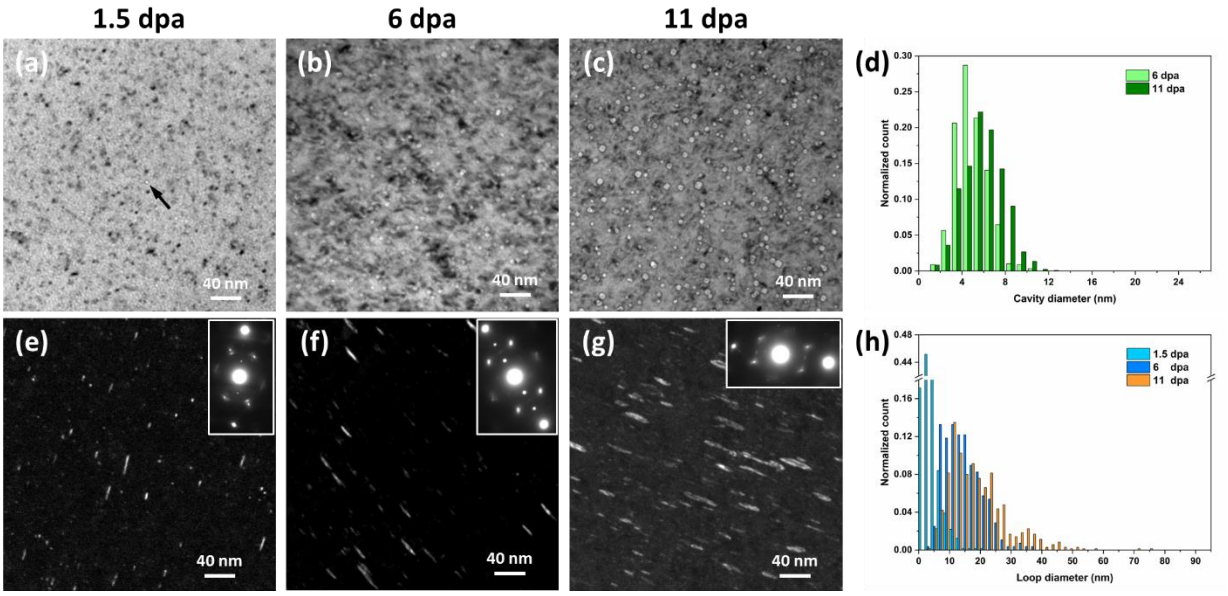

Figure 6.1. TEM bright-field (BF) images showing the formation of cavities in Alloy 625 after proton irradiation at 300 °C to (a) 1.5, (b) 6, and (c) 11 dpa. (d) Cavity diameter distribution at 6 and 11 dpa. TEM rel-rod dark-field (DF) images showing the formation of dislocation loops after proton irradiation at 300 °C to (e) 1.5, (f) 6, and (g) 11 dpa. (h) Loop diameter distribution at 1.5, 6, and 11 dpa. The insets in (e-g) show the imaging conditions of the DF images.

Table 6.1. Summary of cavity diameter and number density in Alloy 625, Alloy 625 Plus, and Alloy 690 after proton irradiation.

Alloy	Irradiation temperature (°C)	Dose (dpa)	Average cavity diameter (nm)	Average cavity number density (10^{21} m^{-3})
625	300	1.5	4.2	0.14
		6	6.1 ± 1.4	12.2 ± 1.7
		11	6.2 ± 1.8	18.9 ± 1.5
625 Plus	300	1.5	2.9 ± 0.6	0.17 ± 0.1
		6	7.3 ± 1.9	2.0 ± 0.4
		11	18.5 ± 2.6	1.6 ± 0.3
690	300	1.5	3.8 ± 0.6	0.23 ± 0.1
		6	9.9 ± 1.9	1.0 ± 0.2
		11	14.1 ± 5.0	2.9 ± 0.5
	400	3	23.1 ± 7.5	0.5 ± 0.1

Table 6.2. Summary of 1/3<1 1 1> dislocation loop diameter and number density in Alloy 625, Alloy 625 Plus, and Alloy 690 after proton irradiation, measured using rel-rod DF imaging method.

Alloy	Irradiation temperature (°C)	Dose (dpa)	Average loop diameter (nm)	Average loop number density (10^{21} m^{-3})
625	300	1.5	5.8 ± 3.2	14.7 ± 4.4
		6	12.6 ± 5.9	16.8 ± 3.7
		11	17.3 ± 9.3	33.5 ± 4.3
625 Plus	300	1.5	4.3 ± 1.6	6.3 ± 2.2
		6	13.5 ± 8.1	11.2 ± 2.8
		11	18.6 ± 10.1	26.7 ± 6.0
690	300	1.5	5.2 ± 1.8	25.0 ± 2.9
		6	18.5 ± 9.6	8.7 ± 1.9
		11	19.1 ± 13.0	18.2 ± 2.4

6.3.2 Alloy 625 Plus

Proton-irradiated Alloy 625 Plus also exhibited high densities of cavities and dislocation loops at 300 °C. Small cavities formed at 1.5 dpa and grew larger with increasing doses (**Figure 6.2a-d**). The average cavity number density increased from 0.17 ± 0.1 to 2.0 ± 0.4 ×10^{21} m^{-3} as dose increased from 1.5 to 6 dpa, and maintained nearly the same (1.6 ± 0.3 ×10^{21} m^{-3}) as dose increased to 11 dpa. The cavities have truncated shapes with major facets lying on {1 1 0}. The volumetric swelling was 0.56 ± 0.1% at 11 dpa. 1/3<1 1 1> type dislocation loops were observed at 1.5 dpa, and their average diameter increased after longer irradiation exposure to 6 and 11 dpa (**Figure 6.2e-h**). Loop diameter distribution became broader with increasing dose as well. The number density of dislocation loops increased monotonically as dose increased. The average diameter and number density of cavities and dislocation loops as a function of dose are summarized

in **Table 6.1** and **Table 6.2**.

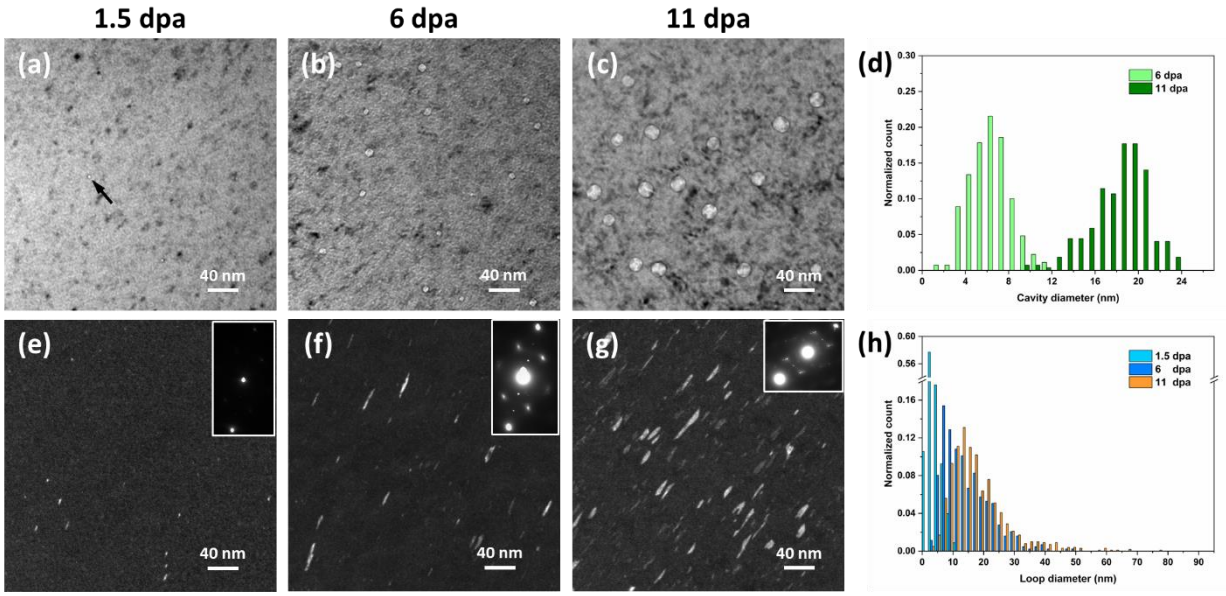

Figure 6.2. TEM BF images showing the formation of cavities in Alloy 625 Plus after proton irradiation at 300 °C to (a) 1.5, (b) 6, and (c) 11 dpa. (d) Cavity diameter distribution at 6 and 11 dpa. TEM rel-rod DF images showing the formation of dislocation loops after proton irradiation at 300 °C to (e) 1.5, (f) 6, and (g) 11 dpa. (h) Loop diameter distribution at 1.5, 6, and 11 dpa. The insets in (e-g) show the imaging conditions of the DF images.

6.3.3 Alloy 690

Cavities and 1/3<1 1 1> type dislocation loops were observed after proton irradiation at 300 °C. For both cavities and dislocation loops, the average diameter increased and the diameter distribution broadened as dose increased (**Figure 6.3**). Measured average diameters and number densities of cavities and dislocation loops as a function of dose are summarized in **Table 6.1** and **Table 6.2**. The volumetric swelling was 0.59 ± 0.13% at 11 dpa. For dislocation loops, <0 0 1> on-zone STEM BF imaging method was also used for quantification. Both 1/3<1 1 1> type and

1/2<1 1 0> type dislocation loops were observed (**Figure 6.4a**). The two different loop types were distinguished based on their projected morphologies (**Figure 6.5**). The proportion of 1/3<1 1 1> loops is ~87% and ~78% at 6 and 11 dpa, respectively. The average diameter and number density of each type of the loop are summarized in **Table 6.3**. The distribution of dislocation loop diameters is summarized in **Figure 6.6**. The measured average diameters and number densities of the 1/3<1 1 1 > type loops using STEM BF imaging method were consistent with those measured using rel-rod method (**Table 6.2** and **Table 6.3**).

Characterization on cavities and dislocation loops in Alloy 690 after proton irradiation at 400 °C to 3 dpa was also conducted. The cavities that formed after proton irradiation at 400 °C were significantly larger than those formed at 300 °C (**Figure 6.7** and **Table 6.1**). The cavities had major facets lying on {1 1 0} planes (**Figure 6.7**). Regarding dislocation loops, both 1/3<1 1 1> type and 1/2<1 1 0> type dislocation loops were observed (**Figure 6.4b**), and ~78% of the loops are 1/3<1 1 1> type loops. Larger loops formed after proton irradiation at 400 °C than those at 300 °C (**Table 6.3**). Some dislocation lines (dislocation network) were also observed (**Figure 6.4b**).

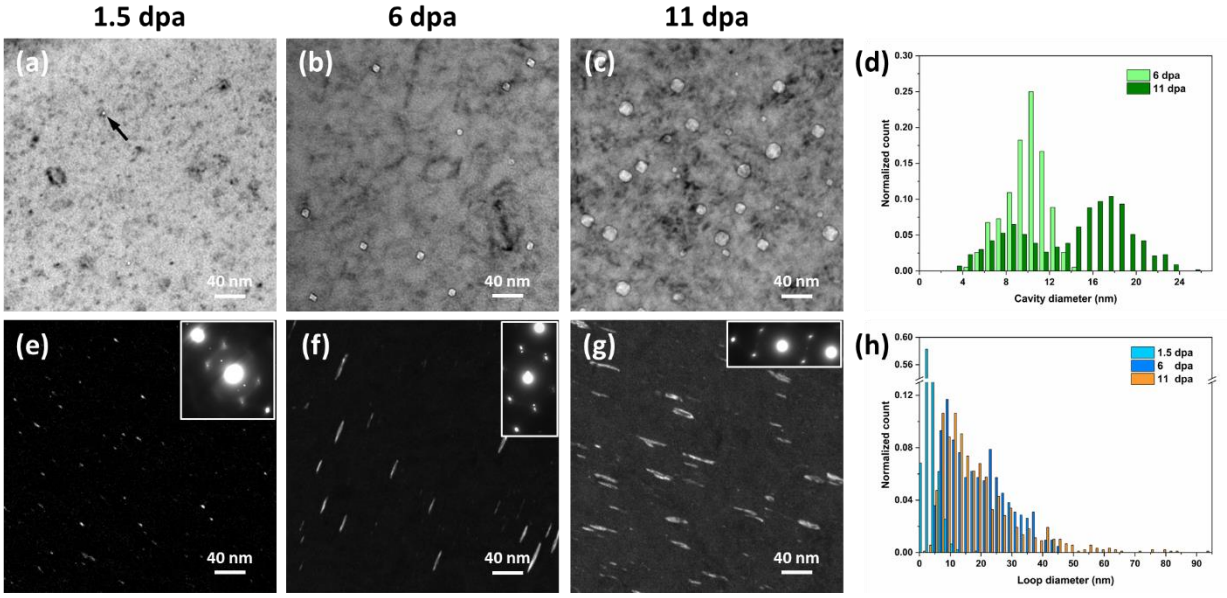

Figure 6.3. TEM BF images showing the formation of cavities in Alloy 690 after proton irradiation at 300 °C to (a) 1.5, (b) 6, and (c) 11 dpa. (d) Cavity diameter distribution at 6 and 11 dpa. TEM rel-rod DF images showing the formation of dislocation loops after proton irradiation at 300 °C to (e) 1.5, (f) 6, and (g) 11 dpa. (h) Loop diameter distribution at 1.5, 6, and 11 dpa. The insets in (e-g) show the imaging conditions of the DF images.

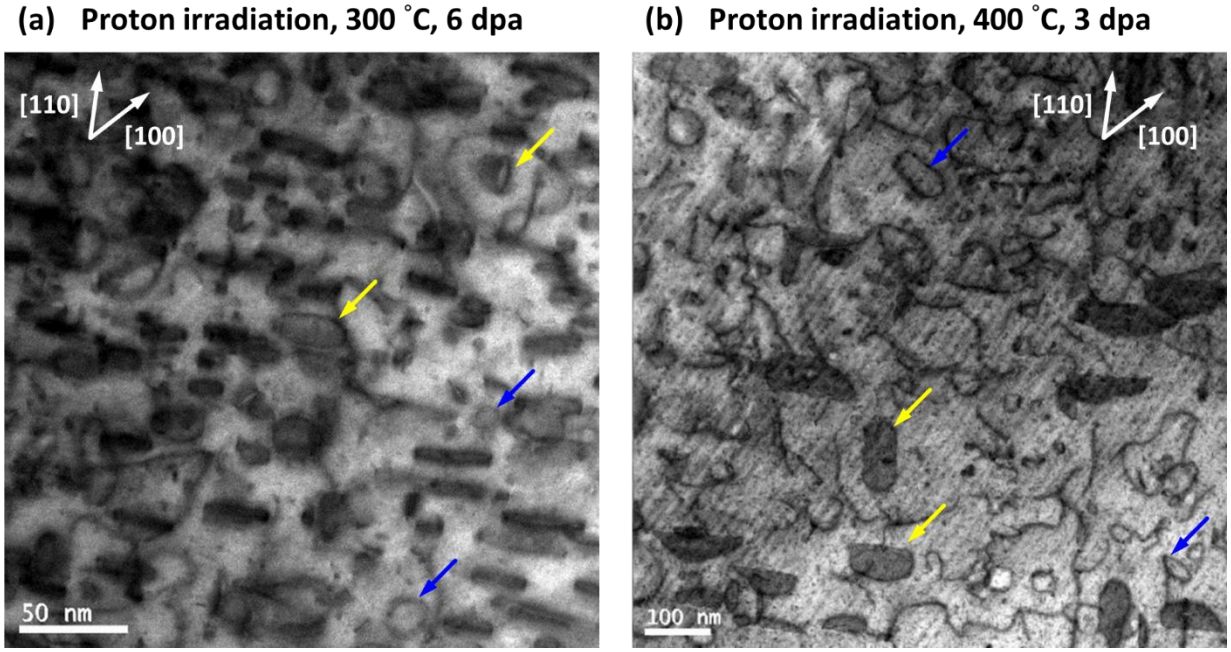

Figure 6.4. <0 0 1> on-zone STEM BF images showing the formation of 1/3<1 1 1> type (indicated by yellow arrows) and 1/2<1 1 0> type (indicated by blue arrows) dislocation loops in

Alloy 690 after proton irradiation at (a) 300 °C to 6 dpa, and (b) 400 °C to 3 dpa.

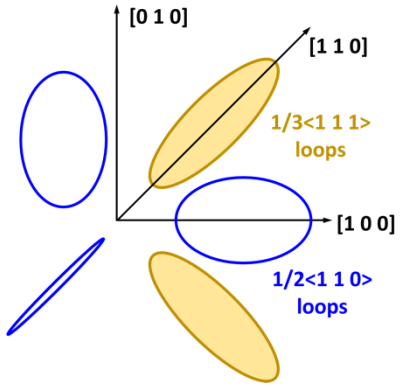

Figure 6.5. Schematic illustration of the projected dislocation loop morphologies imaged from [0 0 1] zone axis.

Table 6.3. Summary of loop diameter and number density in Alloy 690 after proton irradiation, measured using STEM BF imaging method.

Irradiation temperature (°C)	Dose (dpa)	1/3<1 1 1> loop		1/2<1 1 0> loop		Proportion of 1/3<1 1 1> loop (%)
		Average diameter (nm)	Average number density (10^{21} m^{-3})	Average diameter (nm)	Average number density (10^{21} m^{-3})	
300	1.5	5.7 ± 1.3	32.5 ± 2.0	Negligible	Negligible	Negligible
	6	19.9 ± 8.3	12.6 ± 1.5	20.0 ± 7.1	1.9 ± 0.5	87
	11	19.7 ± 8.0	21.0 ± 2.4	20.5 ± 9.9	5.7 ± 0.6	79
400	3	71.9 ± 35.8	0.5 ± 0.1	57.6 ± 22.4	0.1 ± 0.04	78

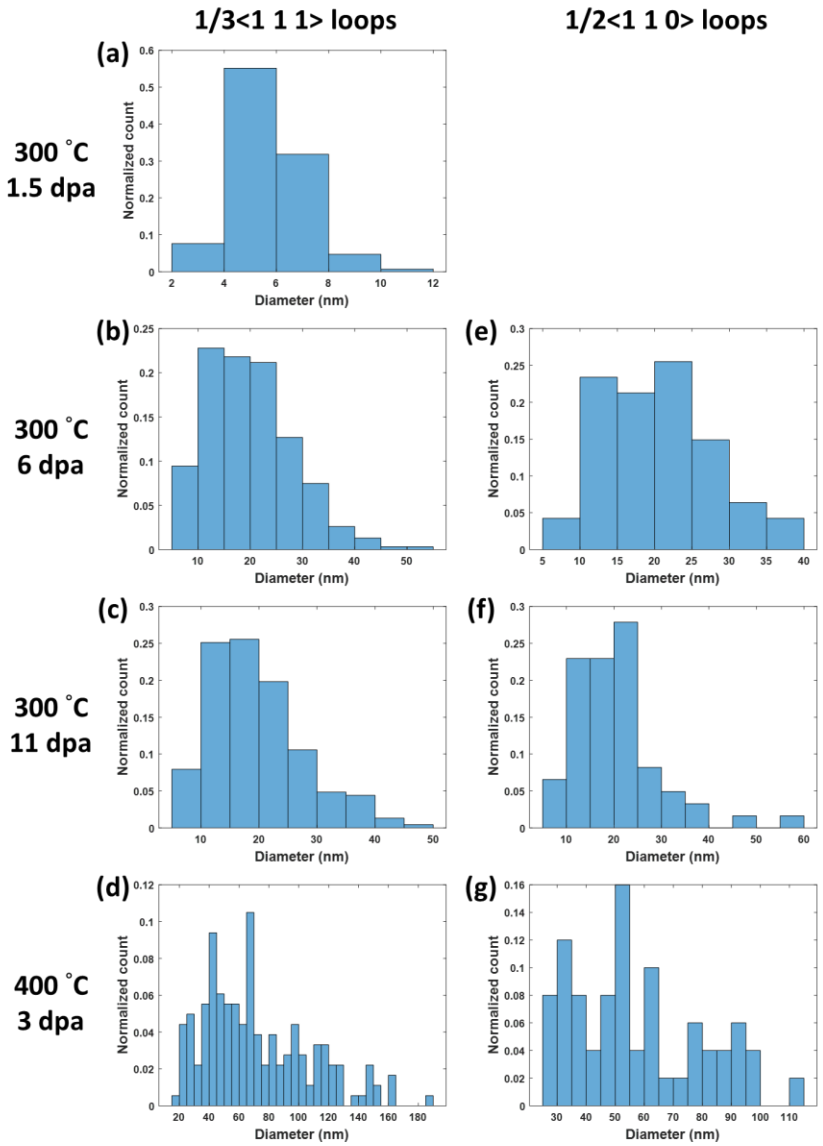

Figure 6.6. Dislocation loop diameter distribution of 1/3<1 1 1> type loops in Alloy 690 after proton irradiation at 300 °C to (a) 1.5, (b) 6, (c) 11 dpa, and (d) at 400 °C to 3 dpa. Dislocation loop diameter distribution of 1/2<1 1 0> type loops in Alloy 690 after proton irradiation at 300 °C to (e) 6, (f) 11 dpa, and (g) at 400 °C to 3 dpa.

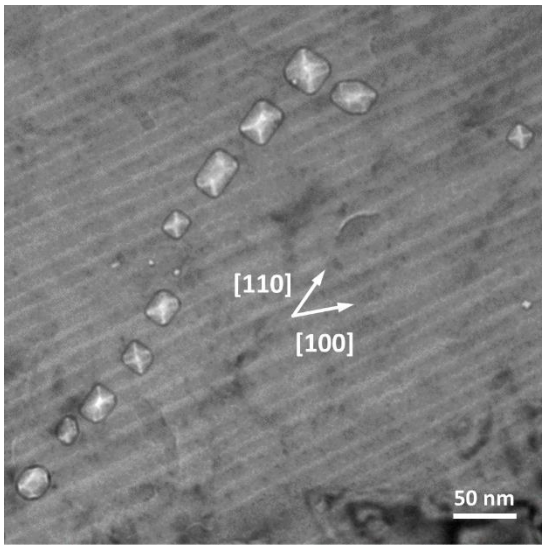

Figure 6.7. TEM BF image showing the formation of cavities in Alloy 690 after proton irradiation at 400 °C to 3 dpa.

6.4 Discussion

Alloy 625 exhibited smaller and a higher number density of cavities, and smaller volumetric swelling compared to the other two alloys after the same irradiation condition (**Figure 6.8**). The activation energy for cavity nucleation depends on the vacancy supersaturation, which is the ratio of the vacancy concentration under irradiation to the thermal equilibrium vacancy concentration at a given temperature [94]. Since the thermal equilibrium vacancy concentration is related to the vacancy formation energy, different vacancy formation energies in alloys could cause different cavity formation behaviors [179]. Cr and Mo were found to increase the vacancy formation energy in Ni alloys [180]. Further calculations of vacancy formation energies in these three alloys would verify this possible mechanism. In addition, solute defect interactions can also affect cavity formation [181]. The strong binding of large-sized solute atoms with vacancies can limit their mobility [123, 124]. The atomic volume size factors for solute atoms in Ni [177] are summarized in **Table 6.4**. Comparing the compositions of Alloy 625 and Alloy 690, the higher concentrations

of two large-sized atoms, Mo and Nb, in Alloy 625, agrees with the formation of a higher number density of smaller cavities. However, the compositions of Alloy 625 and Alloy 625 Plus are quite similar but the alloys still exhibited significantly different cavity sizes and number densities. Recall that γ″ precipitates were observed in Alloy 625 Plus but not in Alloy 625 under proton irradiation at 300 °C (**4.3.2** and **5.3.2**). The formation of γ″ precipitates consumes large-sized solute atoms Nb and Ti. The higher Nb and Ti concentrations in the matrix of Alloy 625 than in that of Alloy 625 Plus might explain the higher number density of smaller cavities in Alloy 625. In terms of dislocation loop evolution, the three alloys displayed similar dislocation loop sizes and number densities despite the different alloy compositions. This might suggest that interstitial mobility was not significantly altered by solute elements in these three alloys. Si segregation to dislocation loops could also affect dislocation loop evolution. Segregation of undersized Si on dislocation loops would reduce the stress field of the faulted loops, which could stabilize the loops against un-faulting. The reduction of stress field could also reduce the sink strength of loops, suppressing the net flux of interstitials to loops [182]. The effects of solute segregation on dislocation loop evolution would need further clarification.

Both cavities and dislocation loops in Alloy 690 showed larger size and a lower number density after irradiation at 400 °C compared to those at 300 °C. Vacancy supersaturation decreases with increasing temperature, leading to a slower cavity nucleation rate and a lower cavity number density [105]. At the same time, the higher vacancy mobility at high temperatures could cause faster growth of cavities [183]. Similarly, interstitials have higher mobility at high temperatures, and thus, are more likely to reach existing dislocation loops, which leads to faster growth of dislocation loops [184]. Concurrently, the faster mobility would allow interstitials to migrate to existing loops rather than condense as new loops, which may cause the lower number density [185].

Moreover, faster loop evolution rate at higher temperature would result in loop un-faulting, which would decrease the number density of 1/3<1 1 1> faulted loops and some dislocation networks may form.

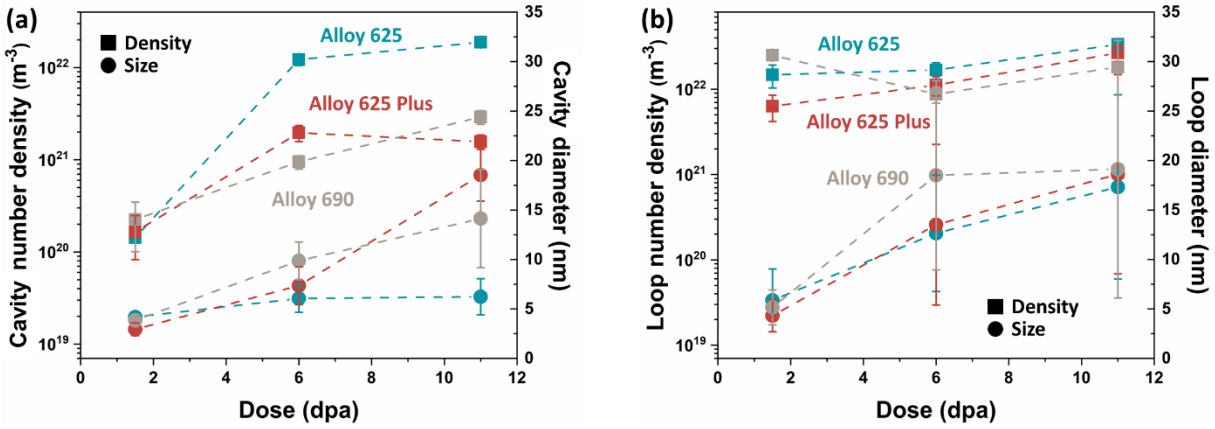

Figure 6.8. (a) Cavity diameter and number density, and (b) dislocation loop diameter and number density in Alloy 625, Alloy 625 Plus, and Alloy 690 after proton irradiation at 300 °C.

Table 6.4. Summary of solute size factors in Ni obtained from [177].

	Ni-Cr	Ni-Fe	Ni-Al	Ni-Mo	Ni-Ti	Ni-Nb
Solute atomic volume size factor (%)	10.3	10.6	14.7	22.3	29.4	51.2

6.5 Conclusions

In the three commercial Ni-based alloys tested in this chapter, the different cavity evolutions under irradiation are consistent with the hypothesis that large-sized solute atoms can strongly bind with vacancies, leading to the formation of cavities with smaller sizes and higher number densities. However, the similar loop evolution seems to suggest that the interstitial mobility was not

significantly altered by alloy composition. Cavity and dislocation loop sizes increase and number densities decrease with increasing irradiation temperature.

Chapter 7

Conclusions and Perspective

7.1 Summary of main findings

This research investigated the effects of irradiation conditions on the microstructural evolution of selected commercial Ni-based alloys. Specifically, three alloys, Alloy 625, Alloy 625 Plus, and Alloy 690, in solutionized (for all three alloys) and aged (for Alloy 625 and Alloy 625 Plus) starting conditions were irradiated using protons and ions under different dose rates (10^{-5}, 10^{-4}, and 10^{-3} dpa/s) and temperatures (300 and 400 °C). The main findings are summarized below:

1. Overall, the precipitation behavior under irradiations is consistent with existing theories stating that cascade mixing and radiation-enhanced diffusion control precipitation evolution. Specifically, cascade mixing dominates at 300 °C under ion irradiation at dose rates above 10^{-4} dpa/s, resulting in the formation of solid solutions. Under proton irradiations at 300 and 400 °C where the effects of cascade mixing and diffusion annihilate, non-equilibrium steady state phase separated microstructures can develop. Although not observed in this study, diffusion-dominated coarsening is expected at the dose rates below 10^{-5} dpa/s and temperatures above 400 °C.

2. Under the non-equilibrium steady state condition tested in this thesis (proton irradiations at the dose rate of 10^{-5} dpa/s at 300 and 400 °C), precipitated phases/precursors included γ′, γ″, Ni_3Si, and Pt_2Mo-type ordered phase in these three alloys. The microstructural

characterizations on both aged and solutionized samples of the same materials under the same irradiation condition successfully confirmed the establishment of steady state precipitate microstructures with constant average size and number density that are independent of the initial alloy microstructures.

3. The initial microstructures (annealed versus aged) can evolve through different decomposition pathways, eventually leading to the same steady state microstructure. In Alloy 625 Plus, the Pt_2Mo-type ordered phase was not always immediately observed, and required the formation of γ″ precipitates to change the matrix composition and favor the formation of the Pt_2Mo-type ordered phase (**Chapter 4**).

4. The precipitation behavior of each phase depends distinctively on alloy compositions. The strengthening γ″ phase can maintain present in Alloy 625 Plus but not in Alloy 625 under the same irradiation condition, which may be attributed to the larger precipitation driving force of γ″ phase in Alloy 625 Plus (**Chapter 4**), as observed under high temperature thermal aging (**Chapter 3**). The Pt_2Mo-type ordered phase remained present at higher temperatures in Alloy 625 and Alloy 625 Plus than in Alloy 690 (**Chapter 5**), in agreement with the observations that Fe decreases, and Nb and Mo increases the order-disorder transformation temperature.

5. The three alloys showed different cavity evolutions under the same irradiation condition, which would indicate the dependence of vacancy mobility on alloy composition. Cavity size and number density evolutions were qualitatively consistent with prior predictions that large-sized solute atoms have strong binding with vacancies, which limits the vacancy mobility and leads to cavity formation with smaller sizes and higher number densities. Yet, the dislocation loop evolution appeared to be similar despite the compositional differences, which would suggest similar interstitial mobility in these three alloys (**Chapter 6**).

7.2 Recommendations for future works

This study expands our understanding of precipitation behavior in three commercial Ni-based alloys under ion and proton irradiations at relevant reactor service temperatures. The precipitation behavior captured in this study under proton and ion irradiations at different dose rates and temperatures can be used to validate simulation models for predictions of neutron irradiation responses. However, no neutron irradiated data were obtained at the time of this study due to delay related to the COVID-19 pandemic. We have been awarded a Nuclear Science User Facilities (NSUF) Rapid Turnaround Experiment (RTE) project titled "Microstructure analysis of neutron irradiated Alloy 625". This project will focus on quantifying the microstructure of Alloy 625 developing after neutron irradiation. Characterization of neutron irradiated microstructures of these commercial alloys is beneficial for benchmarking the prediction of simulation model using charged particle irradiation experiments data, and for understanding the different natures between neutron and charged particle irradiations.

We used proton and ion irradiations across three dose rates with one order of magnitude difference between each condition to investigate the dose rate effects on precipitation behavior. Although the dose rate difference may be large enough and can dominantly affect the resulting microstructures, the impact of different irradiating particles cannot be ruled out. Cascade mixing is inherently less significant under proton than ion and neutron irradiations. Moreover, the higher production of freely migrating defects under proton irradiation may cause enhanced diffusion than under ion and neutron irradiations. Hence, characterization of samples of the same material, after the same irradiation exposure conditions (dose, dose rate, and temperature) will be beneficial for verifying the extent of influence of using different irradiating particles. Analyses on the effects of

cascade morphology, and relative amount of freely migrating defects between different types of irradiating particles could be studied. Using ion and proton irradiations at the dose rate of 10^{-5} dpa/s is experimentally feasible and would be a good starting point. So far, only one study focuses on comparing ion-irradiated and proton-irradiated microstructures, especially cavities, dislocation loops, and α′ precipitates of Fe-Cr alloys under the same dose, dose rate, and temperature [186].

The Pt_2Mo-type ordered phase was not fully characterized in terms of composition, size, and number density from direct imaging in this study, which hinders the understanding of how irradiation conditions affect the order-disorder transformation behavior, and the necessary information for building simulation model of precipitate evolution under irradiation. Especially, whether the Pt_2Mo-type phase evolved toward a constant size and number density or coarsened remains unclear, which needs further clarification. The low contrast between the precipitates and the matrix makes the quantification difficult via TEM DF imaging. In addition, the lack of obvious compositional difference between the Ni/Cr ratio of the precipitates and the matrix challenges the quantification of precipitate composition, size, volume fraction, and number density from APT data. High Mo ternary Ni-Cr-Mo would be a good starting point since Mo is expected to partition to the Pt_2Mo-type precipitates, leading to obvious compositional differences that are favorable for APT characterization. The Ni-Cr-Mo ternary model alloys can also serve as a basis for understanding the precipitation behavior of more complex commercial Ni-based alloys.

As we observed in this study, the phase decomposition in an alloy during irradiation is significantly related to its thermal precipitation behavior. However, due to the sluggish diffusion kinetics, little information was reported especially at temperatures below 500 °C, which are also within the working temperature ranges of LWRs and several advanced reactors. This knowledge gap limits the direct comparison between thermally treated and irradiated samples for

understanding of the exclusive influence of irradiation damage. Thus, long-term thermal aging experiments (for aging time up to the order of 10^5 h) on commercial Ni-based alloys would assist in bridging the gap.

Finally, this work focused exclusively on the characterization and analysis of the irradiated microstructures. Investigation on the mechanical properties of the irradiation alloys is favorable for understanding macroscopic materials behavior, and developing the irradiated microstructure-property relationship.

Appendices

Appendix I Irradiation experiment details

Prior to irradiation, alloys were cut in the form of 12 × 2 × 3 mm^3 bars by electrical discharge machining (EDM). These bar samples were hand-ground using silicon carbide grinding papers with grits of 600, 800, and 1200. After grinding, samples were also hand-polished using a cloth pad with 1 μm diamond suspension solution. To remove the surface damage induced by hand-polishing, the sample surfaces for further irradiation were then electropolished. The schematic illustration of the set-up of electropolishing is shown in **Figure I.1**. A sample was connected to a power supply and served as the anode. A graphite bar was used as the cathode. The electrolyte was made up of 10% perchloric acid plus 90% methanol, and was cooled down to around -30 to -40 °C using a cooling bath containing methanol and dry ice pellets. Once the sample was soaked into the electrolyte, electropolishing started. All the Ni-based alloys used in this thesis were electropolished at an applied voltage of 30 V at -30 to -40 °C for around 30 seconds. The sample surface for further irradiation was aligned to face to the cathode graphite bar. During electropolishing, a magnetic stirrer was used to create a constant stirring in order to refresh the electrolyte near the sample surface. After electropolishing, the sample was quickly removed from the electrolyte and rinsed with methanol to prevent further etching of electrolyte residue on the sample surface.

The proton irradiation experiments were conducted using a 3 MV Pelletron accelerator to generate a 2 MeV proton beam, and ion irradiation experiments were conducted using a 1.7 MV

Tandem accelerator to generate a 5 MeV Ni^{3+} ion beam in the Michigan Ion Beam Laboratory at the University of Michigan. Five samples and two guide bars (additional bars of Ni-based alloys that were not intended for characterization) were held down on an irradiation stage and irradiated. For proton irradiation, a thin layer of indium was placed on the stage, and a thin graphite layer was placed between the indium and samples. The indium layer was molten during irradiation to provide effective thermal contact between the samples and the irradiation stage. The graphite layer was used since it can prevent any chemical reactions between the indium layer and Ni-based samples, and can still have good thermal conduction. For ion irradiation, a thin copper foil was placed between the stage and the samples to facilitate thermal contact. A stainless steel mask with an opening of 9 × 18 mm^2 was placed on top of the samples in order to define the irradiated area. Samples, guide bars, and the mask were then held down firmly on the irradiation stage using hold-down bars. Four thermocouples were welded on the guide bars and used for calibrating the temperature of the samples. A photo of an assembled irradiation stage is shown in **Figure I.2**.

Stopping and Range of Ions in Matter (SRIM) calculation was performed to estimate the damage level using quick Kinchin–Pease mode with the displacement energy of 25 eV. The compositions of alloys used for SRIM calculation are listed in **Table 2.1**. The damage profiles after proton and ion irradiations are shown in **Figure I.3**. The calculated SRIM damage value was used to estimate the appropriate beam current that will be used to obtain the desired dose rate. The relation between dose rate (dap/time) and beam current is:

$$\text{dose rate}\left(\frac{\text{dpa}}{\text{time}}\right) = \frac{(SRIM\ damage\ value)(average\ beam\ current)}{(alloy\ atomic\ density)(ion\ charge)(irradiated\ area)}$$

Taking Alloy 625 as an example, for proton irradiation, the depth of about 3 μm below the sample surface was chosen for damage calculation and further TEM and APT characterizations. The SRIM damage value at this depth was ~5.4×10^{-5} displacements/angstrom/ion. Using the atomic density

of ~8.3 × 10^{22} at/cm^3, and the irradiated area of ~1.28 cm^2, the calculated average proton beam current for obtaining the dose rate of 10^{-5} dpa/s was ~31 μA. For the other two alloys, the calculated SRIM damage values are ~5.1 × 10^{-5} and ~5.2 × 10^{-5} displacements/angstrom/ion, respectively, and the average beam currents for reaching the same dose rate (10^{-5} dpa/s) are 33 and 34 μA, respectively, which do not largely deviate from the beam current for Alloy 625. Thus, all samples were subjected to a similar dose rate. For ion irradiation, the depth of ~700 nm below the sample surface was selected, and SRIM damage value was ~6.9 × 10^{-1} (displacements/angstrom/ion) for Alloy 625. The calculated average ion beam currents for obtaining the dose rate of 10^{-4} and 10^{-3} dpa/s are ~0.07 and ~0.7 μA, respectively. Again, the other two alloys were subjected to similar dose rates as Alloy 625 when using the same beam current.

Before irradiation, the irradiation stage was first heated up to the desired temperature (300 or 400 °C in this thesis), as measured by the four thermocouples welded on the guide bars. Infrared thermal images were taken to monitor the temperature of the samples throughout the irradiation experiment, as shown in **Figure I.4**. Three user-defined area of interests (AOIs) were located on the irradiated regions of each sample for monitoring the samples temperature. The emissivity of the AOIs was calibrated based on the temperature displayed by the thermocouples, so that the infrared image then reported the correct temperature. Once the calibration was finished, the ion beam was turned on. During irradiation, the irradiation temperature was carefully remained at the desired temperature by adjusting the heater and air cooling loop on the backside of the irradiation stage. Irradiation was performed under a pressure below 10^{-7} torr. A raster-scanning beam with frequencies of ~220 Hz in the x-direction and ~2000 Hz in the y-direction, was used for both proton and ion irradiations in this thesis in order to fully cover all the sample surfaces. Beam current was monitored throughout the experiment. Once the desired dose level was reached, the

irradiation stage was rapidly cooled down to room temperature to avoid any thermal annealing effects.

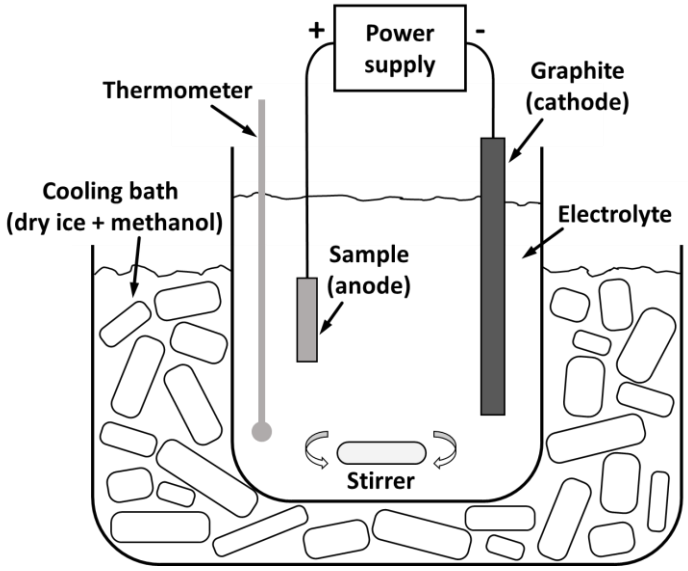

Figure I.1. Schematic illustration of the set-up of electropolishing.

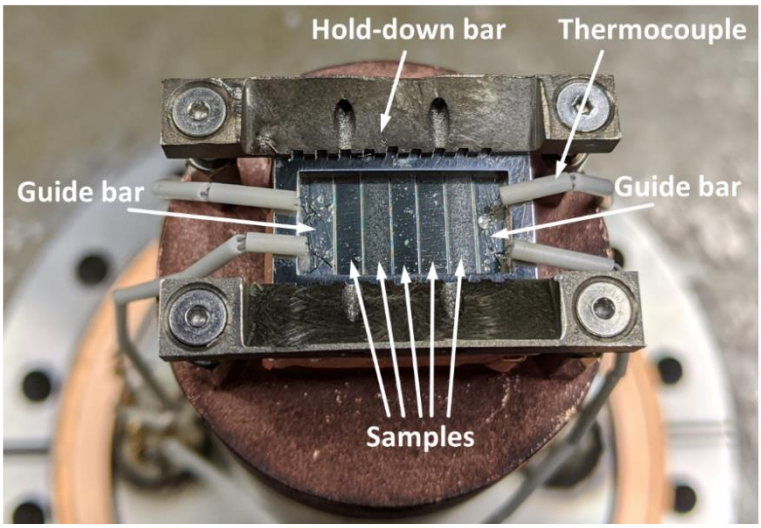

Figure I.2. Photo of an assembled irradiation stage.

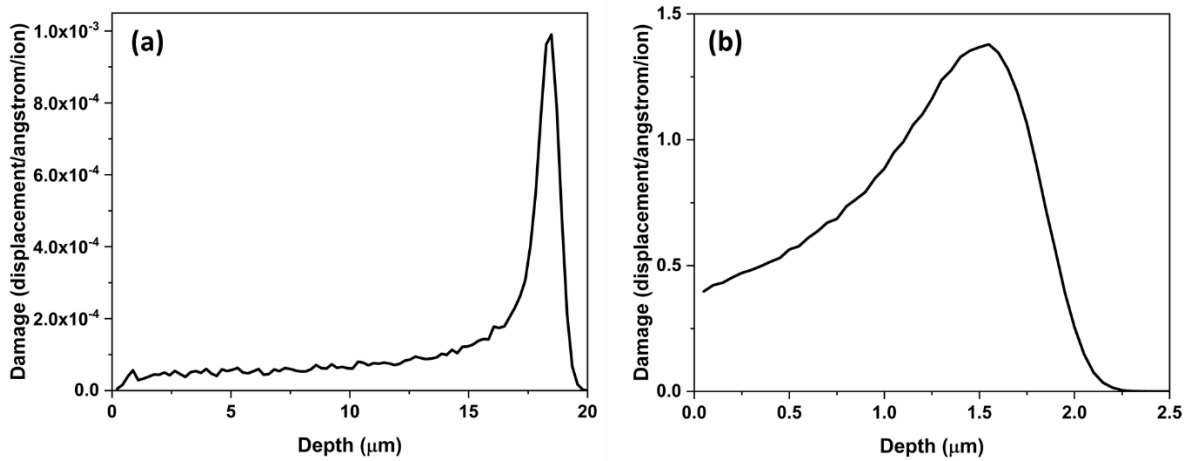

Figure I.3. SRIM calculated damage profiles in Alloy 625 under (a) 2 MeV proton irradiation, and (b) 5 MeV Ni ion irradiation.

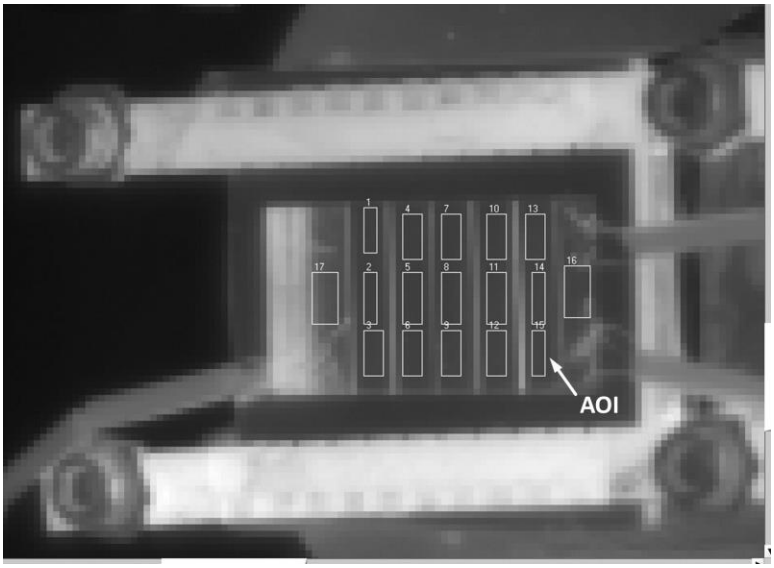

Figure I.4. Infrared image of the irradiation stage.

Appendix II Complementary APT datasets

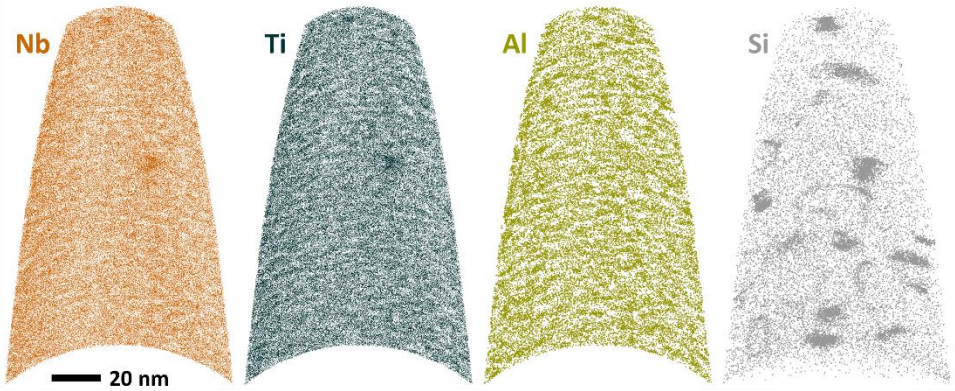

Figure II.1. APT ion maps of Alloy 625 Plus after proton irradiation at the dose rate of 10^{-5} dpa/s to 6 dpa at 300 °C.

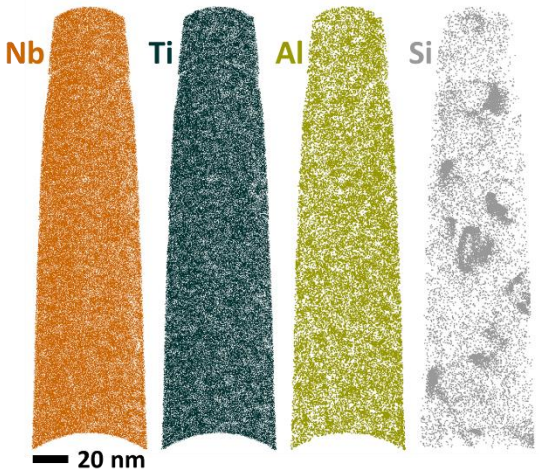

Figure II.2. APT ion maps of Alloy 625 Plus after proton irradiation at the dose rate of 10^{-5} dpa/s to 11 dpa at 300 °C.

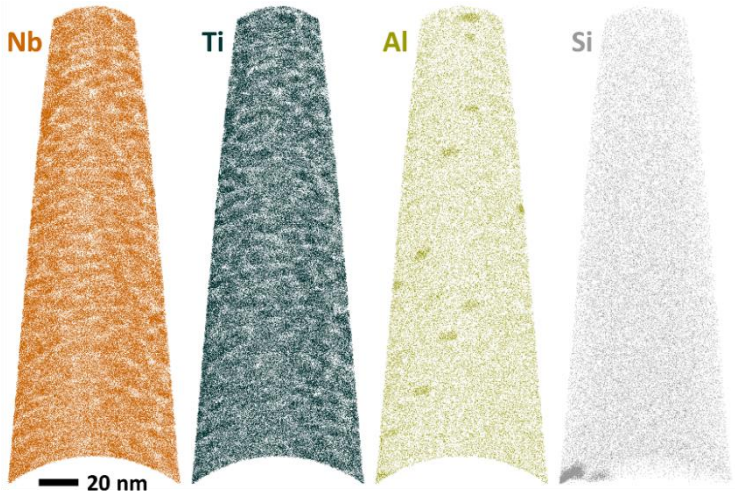

Figure II.3. APT ion maps of Alloy 625 Plus after proton irradiation at the dose rate of 10^{-5} dpa/s to 3 dpa at 400 °C.

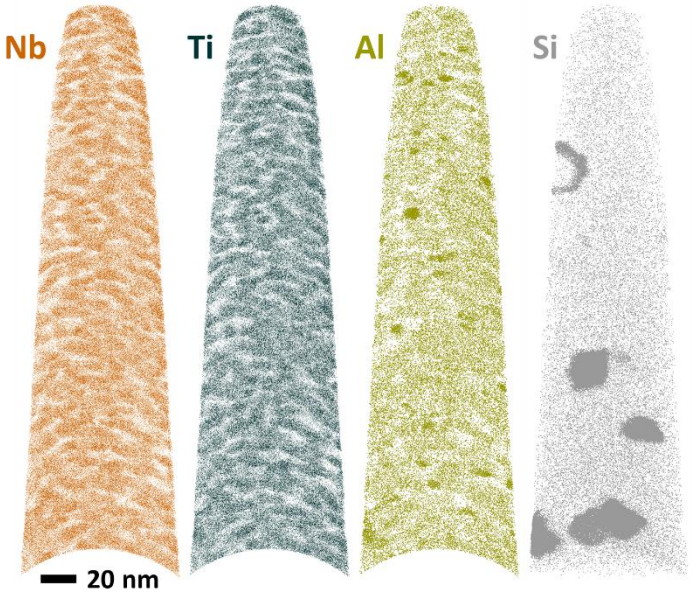

Figure II.4. APT ion maps of Alloy 625 Plus after aging at 650 °C for 100 h + proton irradiation at the dose rate of 10^{-5} dpa/s to 3 dpa at 400 °C.

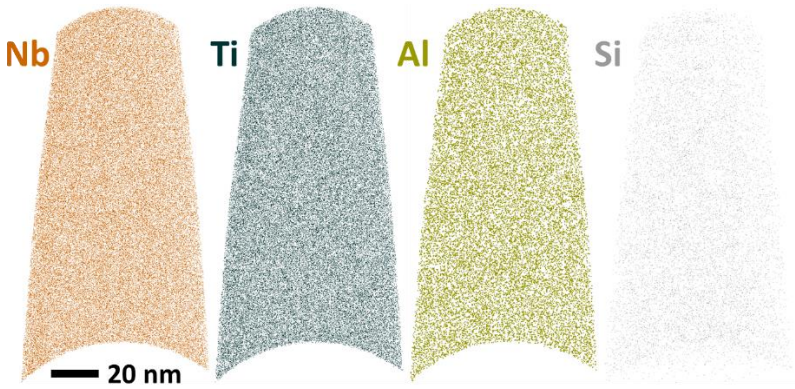

Figure II.5. APT ion maps of Alloy 625 Plus showing the uniform distribution of elements after ion irradiation at the dose rate of 10^{-3} dpa/s to 1.5 dpa at 300 °C.

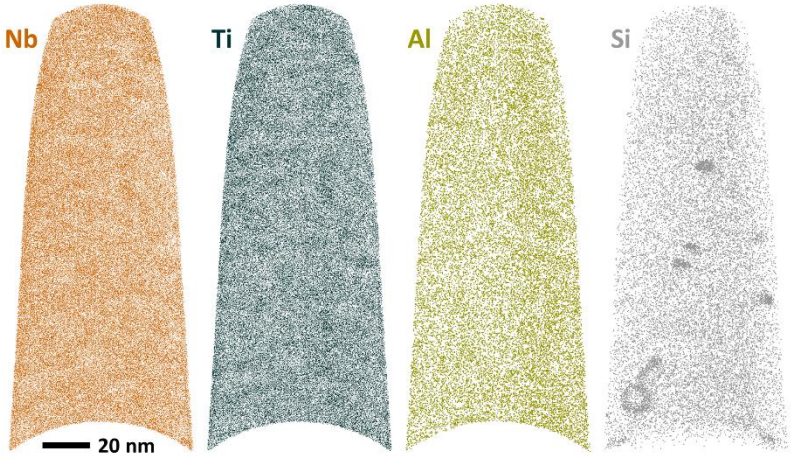

Figure II.6. APT ion maps of Alloy 625 Plus after aging at 650 °C for 100 h + ion irradiation at the dose rate of 10^{-4} dpa/s to 3 dpa at 400 °C.

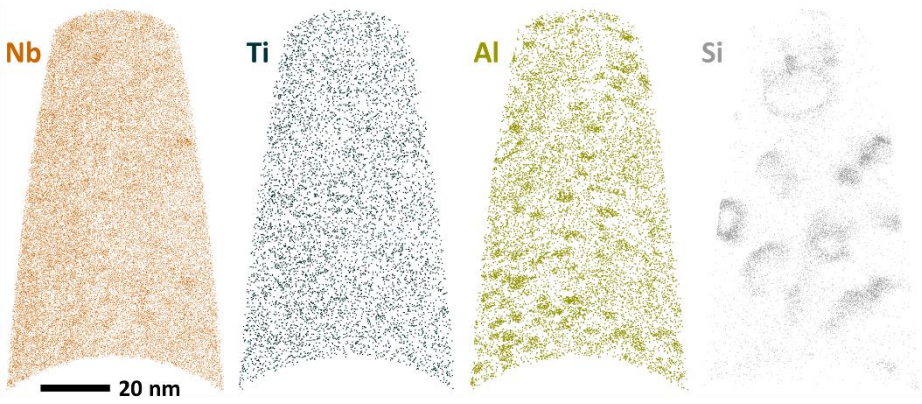

Figure II.7. APT ion maps of Alloy 625 after proton irradiation at the dose rate of 10^{-5} dpa/s to 6 dpa at 300 °C.

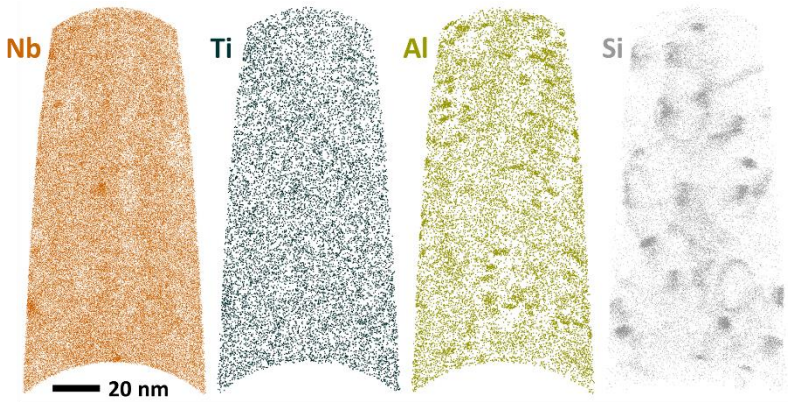

Figure II.8. APT ion maps of Alloy 625 after proton irradiation at the dose rate of 10^{-5} dpa/s to 11 dpa at 300 °C.

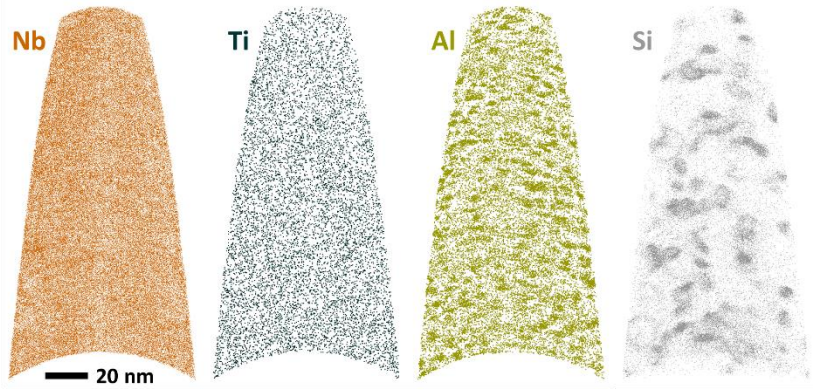

Figure II.9. APT ion maps of Alloy 625 after aging at 650 °C for 25 h + proton irradiation at

the dose rate of 10^{-5} dpa/s to 5 dpa at 300 °C.

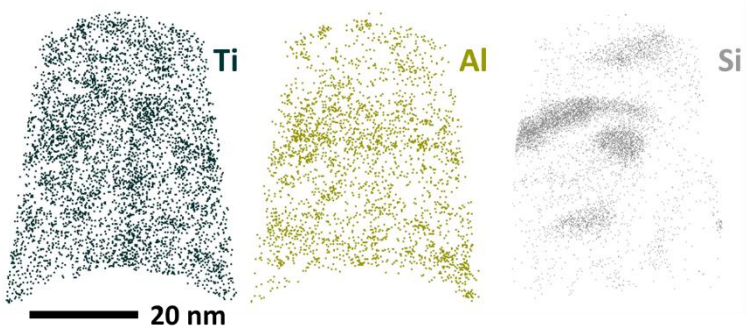

Figure II.10. APT ion maps of Alloy 690 after proton irradiation at the dose rate of 10^{-5} dpa/s to 11 dpa at 300 °C.

Additional APT ion maps of Alloy 690 after proton irradiation at 400 °C to 3 dpa from different datasets are shown in **Figure II.11**. Most of the γ′ Ni_3(Al, Ti) precipitates were only partially contained in the datasets (**Figure II.11a-d**). One dataset contains three complete γ′ precipitates, as pointed out by the black arrows in **Figure II.11e**, which would suggest that in addition to forming heterogeneously on the Ni_3Si precipitate/matrix interfaces (**Chapter 5**), γ′ phase can also precipitate from the matrix.

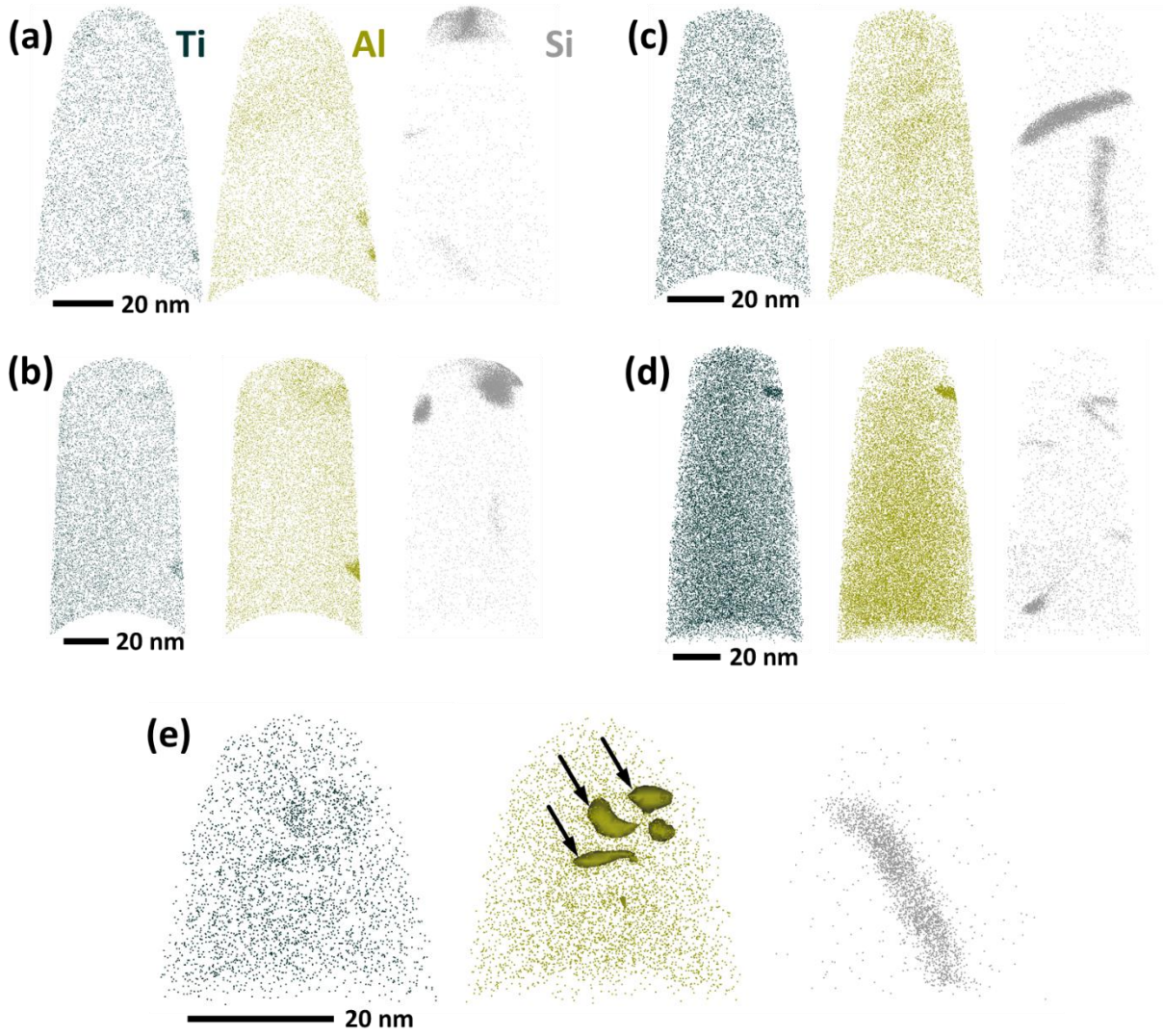

Figure II.11. APT ion maps of Alloy 690 after proton irradiation at the dose rate of 10^{-5} dpa/s to 3 dpa at 400 °C from different datasets.

References

1. License renewals granted for operating nuclear power reactors, United States Nuclear Regulatory Commission, August 2019. https://www.nrc.gov/images/reading-rm/doc-collections/maps/power-reactors-license-renewals.png

2. Reactor license renewal and subsequent renewal, NUREG/BR-0291, Revision 3, United States Nuclear Regulatory Commission, April 2018.

3. A technology roadmap for Generation IV nuclear energy systems, U.S. DOE Nuclear Energy Research Advisory Committee and the Generation IV International Forum, December 2002.

4. Technology roadmap update for Generation IV nuclear energy systems, the OECD Nuclear Energy Agency for the Generation IV International Forum, January 2014.

5. S. J. Zinkle and J. T. Busby, Structural materials for fission & fusion energy, *Materials Today* **12** (2009) 12-19.

6. S. J. Zinkle and G. S. Was, Materials challenges in nuclear energy, *Acta Materialia* **61** (2013) 735-758.

7. A. F. Rowcliffe, L. K. Mansur, D. T. Hoelzer and R. K. Nanstad, Perspectives on radiation effects in nickel-base alloys for applications in advanced reactors, *Journal of Nuclear Materials* **392** (2009) 341-352.

8. S. Fyfitch, Corrosion and Stress Corrosion Cracking of Ni-Base Alloys, in *Comprehensive Nuclear Materials*, ed. R. J. M. Konings (Oxford: Elsevier, 2012) 69-92.

9. D. L. Harrod, R. E. Gold and R. J. Jacko, Alloy optimization for PWR steam generator heat-transfer tubing, *JOM* **53** (2001) 14-17.

10. P. Andresen, F. Garner, J. A. Gorman, S. A. Maloy, J. L. Nelson, L. Tan, M. Toloczko and G. Was, Critical Issues Report and Roadmap for the Advanced Radiation-Resistant Materials Program, 1026482, EPRI, December 2012.

11. G. S. Was, M. Song and M. Wang, Assessment of Radiation Resistance of Selected Alloys in

the ARRM Program Using Ion Irradiation, M3LW-16OR0406024, U.S. Department of Energy, Office of Nuclear Energy, September 2016.

12. Y. Guérin, G. S. Was and S. J. Zinkle, Materials Challenges for Advanced Nuclear Energy Systems, *MRS Bulletin* **34** (2017) 10-19.

13. D. Sandusky, W. Lunceford, S.M. Bruemmer, and M.A. Catalan, Assessment of Materials Issues for Light-Water Small Modular Reactors, PNNL-22290, Pacific Northwest National Laboratory, February 2013.

14. G. S. Was, Z. Jiao, E. Getto, K. Sun, A. M. Monterrosa, S. A. Maloy, O. Anderoglu, B. H. Sencer and M. Hackett, Emulation of reactor irradiation damage using ion beams, *Scripta Materialia* **88** (2014) 33-36.

15. S. J. Zinkle and L. L. Snead, Opportunities and limitations for ion beams in radiation effects studies: Bridging critical gaps between charged particle and neutron irradiations, *Scripta Materialia* **143** (2018) 154-160.

16. G. S. Was and T. Allen, Intercomparison of microchemical evolution under various types of particle irradiation, *Journal of Nuclear Materials* **205** (1993) 332-338.

17. E. R. Reese, N. Almirall, T. Yamamoto, S. Tumey, G. Robert Odette and E. A. Marquis, Dose rate dependence of Cr precipitation in an ion-irradiated Fe 18Cr alloy, *Scripta Materialia* **146** (2018) 213-217.

18. Monthly energy review, DOE/EIA-0035(2020/7), U.S. Energy Information Administration, Office of Energy Statistics, U.S. Department of Energy, July 2020.

19. Information Digest, 2019–2020, NUREG-1350, Volume 31, U.S. Nuclear Regulatory Commission, Office of Public Affairs, August 2019.

20. C. Lemaignan, A.T. Motta, Zirconium alloys in nuclear applications, B.R.T. Frost (Ed.), Materials Science and Technology, A Comprehensive Treatment, vol. 10B, VCH, New York (1994) 1-51.

21. R. L. Klueh and A. T. Nelson, Ferritic/martensitic steels for next-generation reactors, *Journal of Nuclear Materials* **371** (2007) 37-52.

22. F. A. Garner, M. B. Toloczko and B. H. Sencer, Comparison of swelling and irradiation creep behavior of fcc-austenitic and bcc-ferritic/martensitic alloys at high neutron exposure, *Journal of Nuclear Materials* **276** (2000) 123-142.

23. R. Bajaj, W. J. Mills, M. R. Lebo, B. Z. Hyatt and M. G. Burke, Irradiation-Assisted Stress Corrosion Cracking of HTH Alloy X-750 and Alloy 625, *7th International Symposium on Environmental Degradation of Materials in Nuclear Power Systems - Water Reactors* (1995) 1093-1107.

24. A. Strasser and P. Ford, High Strength Nickel Alloys for Fuel Assemblies, ZIRAT17/IZNA12 STR, Advanced Nuclear Technolocy International, 2012.

25. S. Floreen, G. E. Fuchs and W. J. Yang, The Metallurgy of Alloy 625, in *Superalloys 718, 625, 706 and Various Derivatives*, ed. E.A. Loria (Warrendale, PA: TMS, 1994) 13-37.

26. G. D. Smith, D. J. Tillack and S. J. Patel, Alloy 625 - Impressive past/sigmificant presence/awesome future, in *Superalloys 718, 625, 706 and Various Derivatives*, ed. E.A. Loria (Warrendale, PA: TMS, 2001) 35-46.

27. H. L. Eiselstein and D. J. Tillack, The invention and definition of Alloy 625, in *Superalloys 718, 625, and Various Derivatives*, ed. E.A. Loria (Warrendale, PA: TMS, 1991) 1-14.

28. V. Shankar, K. B. S. Rao and S. L. Mannan, Microstructure and mechanical properties of Inconel 625 superalloy, *Journal of Nuclear Materials* **288** (2001) 222-232.

29. M. Sundararaman, L. Kumar, G. E. Prasad, P. Mukhopadhyay and S. Banerjee, Precipitation of an intermetallic phase with Pt_2Mo-type structure in alloy 625, *Metallurgical and Materials Transactions A* **30** (1999) 41-52.

30. R. C. Reed, *The Superalloys: Fundamentals and Applications*, Cambridge: Cambridge University Press, 2006.

31. B. Gwalani, T. Alam, C. Miller, T. Rojhirunsakool, Y. S. Kim, S. S. Kim, M. J. Kaufman, Y. Ren and R. Banerjee, Experimental investigation of the ordering pathway in a Ni-33 at.%Cr alloy, *Acta Materialia* **115** (2016) 372-384.

32. N. C. Eurich and P. D. Bristowe, Thermodynamic stability and electronic structure of η-Ni_6Nb(Al, Ti) from first principles, *Scripta Materialia* **77** (2014) 37-40.

33. M. G. Burke, W. J. Mills and R. Bajaj, Microstructure and properties of direct-aged alloy 625, in *Superalloys 718, 625, 706 and Various Derivatives*, ed. E.A. Loria (Warrendale, PA: TMS, 2001) 389-398.

34. L. M. Suave, J. Cormier, P. Villechaise, A. Soula, Z. Hervier, D. Bertheau and J. Laigo, Microstructural Evolutions During Thermal Aging of Alloy 625: Impact of Temperature and

Forming Process, *Metallurgical and Materials Transactions A* **45** (2014) 2963-2982.

35. M. Sundararaman, P. Mukhopadhyay and S. Banerjee, Precipitation of the δ-Ni_3Nb phase in two nickel base superalloys, *Metallurgical Transactions A* **19** (1988) 453-465.

36. I. J. Moore, M. G. Burke and E. J. Palmiere, Modelling the nucleation, growth and coarsening kinetics of γ″ ($D0_{22}$) precipitates in the Ni-base Alloy 625, *Acta Materialia* **119** (2016) 157-166.

37. W. Xiong, Thermodynamic and Kinetic Investigation of the Fe-Cr-Ni System Driven by Engineering Applications, Doctoral thesis, KTH Royal Institute of Technology, Stockholm, Sweden (2012).

38. G. A. Young, J. D. Tucker and D. R. Eno, The kinetics of long range ordering in Ni-Cr and Ni-Cr-Fe alloys, *Proceedings of the 16th International Conference on Environmental Degradation of Materials in Nuclear Power Systems - Water Reactors, ANS, Asheville, NC, 2013* (2013) 1-22.

39. A. Marucco, Atomic ordering in the Ni-Cr-Fe system, *Materials Science and Engineering A* **189** (1994) 267-276.

40. A. Verma, J. B. Singh, S. D. Kaushik and V. Siruguri, Lattice parameter variation and its effect on precipitation behaviour of ordered Ni_2(Cr, Mo) phase in Ni-Cr-Mo alloys, *Journal of Alloys and Compounds* **813** (2020) 152195.

41. C. Thomas and P. Tail, The performance of Alloy 625 in long-term intermediate temperature applications, *International Journal of Pressure Vessels and Piping* **59** (1994) 41-49.

42. N. B. Schmidt, T. A. Debold and R. B. Frank, Custom Age 625 Plus Alloy - A Higher Strength Alternative to Alloy 625, *Journal of Materials Engineering and Performance* **1** (1992) 483-488.

43. G. F. Vander Voort, J. W. Bowman and R. B. Frank, Microstructural Characterization of Custom Age 625 Plus Alloy, in *Superalloys 718, 625, 706 and Various Derivatives*, ed. E.A. Loria (Warrendale, PA: TMS, 1994) 489-498.

44. A. J. Sedriks, J. W. Schultz and M. A. Cordovi, Inconel Alloy 690 - A New Corrosion Resistant Material, *Corrosion Engineering* **28** (1979) 82-95.

45. A. Marucco, G. Carcano and E. Signorelli, Consequences of ordering on the structural stability of Ni base superalloys over extended exposure times at 450-600 °C, *Materials*

Ageing and Component Life Extension (1995) 363-372.

46. F. Delabrouille, D. Renaud, F. Vaillant and J. Massoud, Long Range Ordering of Alloy 690, *14th International Conference on Environmental Degredation of Materials in Nuclear Power Systems - Water Reactors* **2** (2009) 888-894.

47. T. Larsson, J.-O. Nilsson and J. Frodigh, On the Possibility of Forming Ordered Ni_2Cr in Alloy 690, *Ninth International Symposium on Environmental Degradation of Materials in Nuclear Power Systems - Water Reactors* (1999) 143-148.

48. G. H. Kinchin and R. S. Pease, The Displacement of Atoms in Solids by Radiation, *Reports on Progress in Physics* **18** (1955) 1-51.

49. H. Ullmaier and W. Schilling, Radiation damage in metallic reactor materials, in *Physics of Modern Materials* (Vienna: International Atomic Energy Agency (IAEA), 1980) 301-397.

50. T. D. de la Rubia, R. S. Averback, R. Benedek and W. E. King, Role of thermal spikes in energetic displacement cascades, *Physical Review Letters* **59** (1987) 1930-1933.

51. R. E. Stoller, Primary Radiation Damage Formation, in *Comprehensive Nuclear Materials*, ed. R. J. M. Konings (Oxford: Elsevier, 2012) 293-332.

52. K. Nordlund and F. Djurabekova, Multiscale modelling of irradiation in nanostructures, *Journal of Computational Electronics* **13** (2014) 122-141.

53. L. E. Rehn, P. R. Okamoto and R. S. Averback, Relative efficiencies of different ions for producing freely migrating defects, *Physical Review B* **30** (1984) 3073-3080.

54. R. Sizmann, The effect of radiation upon diffusion in metals, *Journal of Nuclear Materials* **69-70** (1978) 386-412.

55. H. Wiedersich, Phase Stability and Solute Segregation during Irradiation, in *Modern Problems in Condensed Matter Sciences*, ed. R. A. Johnson and A. N. Orlov (Elsevier, 1986) 225-280.

56. O. Tissot, C. Pareige, E. Meslin, B. Decamps and J. Henry, Kinetics of α′ precipitation in an electron-irradiated Fe15Cr alloy, *Scripta Materialia* **122** (2016) 31-35.

57. P. R. Okamoto and L. E. Rehn, Radiation-induced segregation in binary and ternary alloys, *Journal of Nuclear Materials* **83** (1979) 2-23.

58. K. C. Russell, Phase stability under irradiation, *Progress in Materials Science* **28** (1984) 229-

434.

59. A. D. Marwick, R. C. Piller and P. M. Sivell, Mechanisms of radiation-induced segregation in dilute Nickel alloys, *Journal of Nuclear Materials* **83** (1979) 35-41.

60. N. Q. Lam, P. R. Okamoto and R. A. Johnson, Solute segregation and precipitation under heavy-ion bombardment, *Journal of Nuclear Materials* **78** (1978) 408-418.

61. R. A. Johnson and N. Q. Lam, Solute segregation in metals under irradiation, *Physical Review B* **13** (1976) 4364-4375.

62. R. S. Averback, L. E. Rehn, W. Wagner, H. Wiedersich and P. R. Okamoto, Kinetics of radiation-induced segregation in Ni-12.7 at.% Si, *Physical Review B* **28** (1983) 3100-3109.

63. A. Barbu and A. J. Ardell, Irradiation-induced precipitation in Ni-Si alloys, *Scripta Metallurgica* **9** (1975) 1223-1237.

64. A. Barbu and G. Martin, Radiation induced precipitation in nickel silicon solid solution: II - dose rate effects, *Scripta Metallurgica* **11** (1977) 771-775.

65. M. Nastar and F. Soisson, Radiation-Induced Segregation, in *Comprehensive Nuclear Materials*, ed. R. J. M. Konings (Oxford: Elsevier, 2012) 471-496.

66. H. J. Frost and K. C. Russell, Particle stability with recoil resolution, *Acta Metallurgica* **30** (1982) 953-960.

67. G. Martin, Phase stability under irradiation: Ballistic effects, *Physical Review B* **30** (1984) 1424-1436.

68. R. S. Nelson, J. A. Hudson and D. J. Mazey, The stability of precipitates in an irradiation environment, *Journal of Nuclear Materials* **44** (1972) 318-330.

69. H. J. Frost and K. C. Russell, Recoil resolution and particle stability under irradiation, *Journal of Nuclear Materials* **104** (1981) 1427-1432.

70. P. Wilkes, Phase stability under irradiation - a review of theory and experiment, *Journal of Nuclear Materials* **83** (1979) 166-175.

71. R. A. Enrique and P. Bellon, Compositional Patterning in Systems Driven by Competing Dynamics Of Different Length Scale, *Physical Review Letters* **84** (2000) 2885-2888.

72. H. Ro and T. E. Mitchell, Effects of electron irradiation on precipitation in Ni-Al alloys, *Metallurgical Transactions A* **9** (1978) 1749-1760.

73. D. I. Potter and A. W. McCormick, Irradiation-enhanced coarsening in Ni-12.8 at.% Al, *Acta Metallurgica* **27** (1979) 933-941.

74. D. I. Potter and H. Wiedersich, Mechanisms and kinetics of precipitate restructuring during irradiation, *Journal of Nuclear Materials* **83** (1979) 208-213.

75. S. A. Briggs, P. D. Edmondson, K. C. Littrell, Y. Yamamoto, R. H. Howard, C. R. Daily, K. A. Terrani, K. Sridharan and K. G. Field, A combined APT and SANS investigation of α′ phase precipitation in neutron-irradiated model FeCrAl alloys, *Acta Materialia* **129** (2017) 217-228.

76. N. Hashimoto, J. D. Hunn, T. S. Byun and L. K. Mansur, Microstructural analysis of ion-irradiation-induced hardening in inconel 718, *Journal of Nuclear Materials* **318** (2003) 300-306.

77. D. I. Potter and O. G. Hernandez, Ion-bombardment-induced disordering of γ′-Ni_3Si, *Acta Metallurgica* **29** (1981) 187-196.

78. S. W. Chee, B. Stumphy, N. Q. Vo, R. S. Averback and P. Bellon, Dynamic self-organization in Cu alloys under ion irradiation, *Acta Materialia* **58** (2010) 4088-4099.

79. X. Zhang, S. Shu, P. Bellon and R. S. Averback, Precipitate stability in Cu–Ag–W system under high-temperature irradiation, *Acta Materialia* **97** (2015) 348-356.

80. H. K. Zhang, Z. Yao, G. Morin and M. Griffiths, TEM characterization of in-reactor neutron irradiated CANDU spacer material Inconel X-750, *Journal of Nuclear Materials* **451** (2014) 88-96.

81. E. Camus, C. Abromeit, F. Bourdeau, N. Wanderka and H. Wollenberger, Evolution of long-range order and composition for radiation-induced precipitate dissolution, *Physical Review B* **54** (1996) 3142-3150.

82. H. K. Zhang, Z. Yao, M. A. Kirk and M. R. Daymond, Stability of Ni_3(Al, Ti) Gamma Prime Precipitates in a Nickel-Based Superalloy Inconel X-750 Under Heavy Ion Irradiation, *Metallurgical and Materials Transactions A* **45** (2014) 3422-3428.

83. D. I. Potter and D. G. Ryding, Precipitate coarsening, redistribution and renucleation during irradiation of Ni-6.35 wt.% Al, *Journal of Nuclear Materials* **71** (1977) 14-24.

84. C. Sun, M. Kirk, M. Li, K. Hattar, Y. Wang, O. Anderoglu, J. Valdez, B. P. Uberuaga, R. Dickerson and S. A. Maloy, Microstructure, chemistry and mechanical properties of Ni-based

superalloy Rene N4 under irradiation at room temperature, *Acta Materialia* **95** (2015) 357-365.

85. T. Lee, A. Caro and M. J. Demkowicz, Atomistic modeling of radiation-induced disordering and dissolution at a Ni/Ni_3Al interface, *Journal of Materials Research* **30** (2015) 1456-1463.

86. S. Matsumura, M. Okudaira and C. Kinoshita, Instability of ordered precipitates due to local disordering and atomic mixing under irradiation, *Journal of Nuclear Materials* **251** (1997) 145-149.

87. M. G. Burke, Advanced Materials Characterization using AEM and APFIM, in *Developments in materials characterization technologies: symposium held 23 and 24 July 1995, during the 28th Annual Technical Meeting of the International Metallographic Society, Albuquerque, New Mexico, USA*, ed. G. F. V. Voort and J. J. Friel (Columbus, Ohio: International Metallographic Society - ASM International, 1996) 91-101.

88. M. Sundararaman, S. Banerjee and H. Mori, The stability of γ" and γ' phases in Alloy 718 under electron irradiation, in *Superalloys 718, 625, 706 and Various Derivatives*, ed. E.A. Loria (Warrendale, PA: TMS, 2001) 379-387.

89. L. E. Thomas and S. M. Bruemmer, Radiation-induced microstructural evolution and phase stability in Nickel-base Alloy 718, *Proceedings of the 8th International Symposium on Environmental Degradation of Materials in Nuclear Power Systems - Water Reactor* **2** (1997) 772-779.

90. L. E. Thomas, The stability of γ' and γ" in Inconel 706 under neutron irradiation, in *Phase stability during irradiation*, ed. J. R. Holland, J. A. Spitznagel and D. I. Potter (New York: AIME, 1981) 237-255.

91. E. Frely, B. Beuneu, A. Barbu and G. Jaskierowicz, Investigation of ordering kinetics in Ni-Cr-Fe alloys under electron irradiation, *Annales de Physique* **22** (1997) C2-137-144.

92. M. G. Burke and R. Bajaj, Irradiation-Induced Precipitation in Direct-Aged Alloy 625 (1996).

93. M. Song, Y. Yang, M. Wang, W. Kuang, C. R. Lear and G. S. Was, Probing long-range ordering in nickel-base alloys with proton irradiation, *Acta Materialia* **156** (2018) 446-462.

94. D. R. Olander, Fundamental aspects of nuclear reactor fuel elements, TID-26711-P1, Technical Information Center, U.S. Energy Research and Development Administration, April 1976.

95. G. W. Greenwood, A. J. E. Foreman and D. E. Rimmer, The role of vacancies and dislocations in the nucleation and growth of gas bubbles in irradiated fissile material, *Journal of Nuclear Materials* **1** (1959) 305-324.

96. W. G. Wolfer, The Dislocation Bias, *Journal of Computer-Aided Materials Design* **14** (2007) 403-417.

97. C. Cawthorne and E. J. Fulton, Voids in Irradiated Stainless Steel, *Nature* **216** (1967) 575-576.

98. N. H. Packan, K. Farrell and J. O. Stiegler, Correlation of neutron and heavy-ion damage: I. The influence of dose rate and injected helium on swelling in pure nickel, *Journal of Nuclear Materials* **78** (1978) 143-155.

99. L. K. Mansur, Theory and experimental background on dimensional changes in irradiated alloys, *Journal of Nuclear Materials* **216** (1994) 97-123.

100. D. S. Gelles, Microstructural examination of several commercial alloys neutron irradiated to 100 dpa, *Journal of Nuclear Materials* **148** (1987) 136-144.

101. A. I. Bondarenko and Y. V. Konobeev, Void coalescence in metals at high irradiation doses, *Radiation Effects* **29** (1976) 47-51.

102. L. K. Mansur, Void Swelling in Metals and Alloys Under Irradiation: An Assessment of the Theory, *Nuclear Technology* **40** (1978) 5-34.

103. B. N. Singh and S. J. Zinkle, Defect accumulation in pure fcc metals in the transient regime: a review, *Journal of Nuclear Materials* **206** (1993) 212-229.

104. J. L. Brimhall, H. E. Kissinger and G. L. Kulcinski, The effect of temperature on void formation in irradiated pure and impure metals, in *Radiation-induced Voids in Metals: Proceedings of the 1971 International Conference Held at Albany, New York, June 9-11, 1971, AEC Symposium Series 26, CONF-710601,* eds. J. W. Corbett and L. C. Ianniello (Oak Ridge, TN: U.S. Atomic Energy Commission, Technical Information Center, 1972) 338-362.

105. J. L. Brimhall and B. Mastel, Temperature dependence of void formation in neutron irradiated nickel, *Scripta Metallurgica* **4** (1970) 51-54.

106. J. L. Brimhall and H. E. Kissinger, Void formation in irradiated copper, nickel and copper-nickel alloys, *Radiation Effects* **15** (1972) 259-272.

107. J. L. Brimhall and B. Mastel, Stability of voids in neutron irradiated nickel, *Journal of*

Nuclear Materials **33** (1969) 186-194.

108. J. O. Stiegler and E. E. Bloom, Void formation in irradiated Nickel 270, *Radiation Effects* **8** (1971) 33-41.

109. X. Liu, L. He, H. Yan, M. Bachhav and J. F. Stubbins, A transmission electron microscopy study of EBR-II neutron-irradiated austenitic stainless steel 304 and nickel-base alloy X-750, *Journal of Nuclear Materials* **528** (2020) 151851.

110. J.-J. Kai and R. D. Lee, Effects of proton irradiation on the microstructural and microchemical evolution of Inconel 600 alloy, *Journal of Nuclear Materials* **207** (1993) 286-294.

111. S. I. Porollo, A. M. Dvoriashin, Y. V. Konobeev and F. A. Garner, Microstructure and swelling of neutron irradiated nickel and binary nickel alloys, *Journal of Nuclear Materials* **442** (2013) S809-S812.

112. J. Gan and G. S. Was, Microstructure evolution in austenitic Fe–Cr–Ni alloys irradiated with protons: comparison with neutron-irradiated microstructures, *Journal of Nuclear Materials* **297** (2001) 161-175.

113. S. Teysseyre, Z. Jiao, E. West and G. S. Was, Effect of irradiation on stress corrosion cracking in supercritical water, *Journal of Nuclear Materials* **371** (2007) 107-117.

114. R. Zhou, E. A. West, Z. Jiao and G. S. Was, Irradiation-assisted stress corrosion cracking of austenitic alloys in supercritical water, *Journal of Nuclear Materials* **395** (2009) 11-22.

115. S. A. Briggs, C. M. Barr, J. Pakarinen, M. Mamivand, K. Hattar, D. D. Morgan, M. Taheri and K. Sridharan, Observations of defect structure evolution in proton and Ni ion irradiated Ni-Cr binary alloys, *Journal of Nuclear Materials* **479** (2016) 48-58.

116. L. K. Mansur, Correlation of neutron and heavy-ion damage: II. The predicted temperature shift if swelling with changes in radiation dose rate, *Journal of Nuclear Materials* **78** (1978) 156-160.

117. L. K. Mansur, Theory of transitions in dose dependence of radiation effects in structural alloys, *Journal of Nuclear Materials* **206** (1993) 306-323.

118. S. M. Foiles, M. I. Baskes and M. S. Daw, Embedded-atom-method functions for the fcc metals Cu, Ag, Au, Ni, Pd, Pt, and their alloys, *Physical Review B* **33** (1986) 7983-7991.

119. H. H. Neely and K. Herschbach, Void formation in Nickel during high temperature proton irradiation, *Radiation Effects* **7** (1971) 187-194.

120. L. R. Greenwood, A new calculation of thermal neutron damage and helium production in nickel, *Journal of Nuclear Materials* **115** (1983) 137-142.

121. K. C. Russell, The theory of void nucleation in metals, *Acta Metallurgica* **26** (1978) 1615-1630.

122. J. F. Bates and R. W. Powell, Irradiation-induced swelling in commercial alloys, *Journal of Nuclear Materials* **102** (1981) 200-213.

123. T.-n. Yang, C. Lu, G. Velisa, K. Jin, P. Xiu, M. L. Crespillo, Y. Zhang, H. Bei and L. Wang, Effect of alloying elements on defect evolution in Ni-20X binary alloys, *Acta Materialia* **151** (2018) 159-168.

124. T. Kato, H. Takahashi and M. Izumiya, Effects of Systematic Modification with Oversized Elements on Void Formation in 316L Austenitic Stainless Steel under Electron Irradiation, *Materials Transactions, JIM* **32** (1991) 921-930.

125. K. C. Russell and R. W. Powell, Dislocation loop nucleation in irradiated metals, *Acta Metallurgica* **21** (1973) 187-193.

126. F. Kroupa and P. B. Hirsch, Elastic interaction between prismatic dislocation loops and straight dislocations, *Discussions of the Faraday Society* **38** (1964) 49-55.

127. D. J. Bacon, F. Gao and Y. N. Osetsky, The primary damage state in fcc, bcc and hcp metals as seen in molecular dynamics simulations, *Journal of Nuclear Materials* **276** (2000) 1-12.

128. S. J. Zinkle, P. J. Maziasz and R. E. Stoller, Dose dependence of the microstructural evolution in neutron-irradiated austenitic stainless steel, *Journal of Nuclear Materials* **206** (1993) 266-286.

129. P. J. Maziasz, Temperature dependence of the dislocation microstructure of PCA austenitic stainless steel irradiated in ORR spectrally-tailored experiments, *Journal of Nuclear Materials* **191-194** (1992) 701-705.

130. M. Song, C. R. Lear, C. M. Parish, M. Wang and G. S. Was, Radiation tolerance of commercial and advanced alloys for core internals: a comprehensive microstructural characterization, *Journal of Nuclear Materials* **510** (2018) 396-413.

131. C. R. Lear, M. Song, M. Wang and G. S. Was, Dual ion irradiation of commercial and advanced alloys: Evaluating microstructural resistance for high dose core internals, *Journal of Nuclear Materials* **516** (2019) 125-134.

132. N. A. P. K. Kumar, C. Li, K. J. Leonard, H. Bei and S. J. Zinkle, Microstructural stability and mechanical behavior of FeNiMnCr high entropy alloy under ion irradiation, *Acta Materialia* **113** (2016) 230-244.

133. P. Changizian, Z. Yao, C. Lu, F. Long and M. R. Daymond, Radiation effect on nano-indentation properties and deformation mechanisms of a Ni-based superalloy X-750, *Journal of Nuclear Materials* **515** (2019) 1-13.

134. W. Z. Friend, *Corrosion of nickel and nickel-base alloys*, New York, NY: Wiley-Interscience, 1980.

135. J. R. Hayes, J. J. Gray, A. W. Szmodis and C. A. Orme, Influence of Chromium and Molybdenum on the Corrosion of Nickel-Based Alloys, *CORROSION* **62** (2006) 491-500.

136. P. Crook, Corrosion of Nickel and Nickel-Base Alloys, in *ASM Handbook, Volume 13B: Corrosion: Materials*, eds. S. D. Cramer and B. S. Covino, Jr. (ASM International, 2005) 228-251.

137. A. K. Jena and M. C. Chaturvedi, The role of alloying elements in the design of nickel-base superalloys, *Journal of Materials Science* **19** (1984) 3121-3139.

138. R. Cozar, M. Rouby, B. Mayonobe and C. Morizot, Mechanical properties, corrosion resistance and microstructure of both regular and titanium hardened 625 alloys, in *Superalloys 718, 625, and Various Derivatives*, ed. E.A. Loria (Warrendale, PA: TMS, 1991) 423-436.

139. R. Schafrik and R. Sprague, Saga of gas turbine materials, part III, *Advanced Materials and Processes* **162** (2004) 29-33.

140. D. F. Paulonis and J. J. Schirra, Alloy 718 at Pratt & Whitney: Historical Perspective and Future Challenges, in *Superalloys 718, 625, 706 and Various Derivatives*, ed. E.A. Loria (Warrendale, PA: TMS, 2001) 13-23.

141. D. F. Paulonis, J. M. Oblak and D. S. Auvall, Precipitation in Nickel-base Alloy 718, *Transactions of the American Society for Metals* **62** (1969) 611-622.

142. R. B. Frank and T. A. DeBold, Heat treatment of an age-hardenable corrosion-resistant alloy - UNS NO7716, paper No. 59, in *the NACE Corrosion '90 Conference* (Las Vegas, NV 1990).

143. R. B. Frank and R. Grimes, Properties of Ultra-high-strength Custom Age 625 Plus Alloy, in *Superalloys 718, 625, 706 and Various Derivatives*, ed. E.A. Loria (Warrendale, PA: TMS, 1994) 499-508.

144. T. T. Tsong, Field ion image formation, *Surface Science* **70** (1978) 211-233.

145. O. C. Hellman, J. A. Vandenbroucke, J. Rüsing, D. Isheim and D. N. Seidman, Analysis of Three-dimensional Atom-probe Data by the Proximity Histogram, *Microscopy and Microanalysis* **6** (2002) 437-444.

146. J. F. Radavich and A. Fort, Effects of Long-Time Exposure in Alloy 625 at 1200 °F, 1400 °F and 1600 °F, in *Superalloys 718, 625, 706 and Various Derivatives*, ed. E.A. Loria (Warrendale, PA: TMS, 1994) 635-647.

147. C. R. Conder, G. D. Smith and J. F. Radavich, *Microstructural and Mechanical Property Characterization of Aged Inconel Alloy 625LCF*, in *Superalloys 718, 625, 706 and Various Derivatives*, ed. E.A. Loria (Warrendale, PA: TMS, 1997) 447-458.

148. R. Cozar and A. Pineau, Morphology of γ′ and γ″ precipitates and thermal stability of Inconel 718 type alloys, *Metallurgical Transactions* **4** (1973) 47-59.

149. A. J. Detor, R. DiDomizio, R. Sharghi-Moshtaghin, N. Zhou, R. Shi, Y. Wang, D. P. McAllister and M. J. Mills, Enabling Large Superalloy Parts Using Compact Coprecipitation of γ′ and γ″, *Metallurgical and Materials Transactions A* **49** (2017) 708-717.

150. H. Gardner, S. Pedrazzini, J. O. Douglas, D. De Lille, M. P. Moody and P. A. J. Bagot, Atom Probe Tomography Investigations of Microstructural Evolution in an Aged Nickel Superalloy for Exhaust Applications, *Metallurgical and Materials Transactions A* **50** (2019) 1862-1872.

151. M. K. Miller, Contributions of atom probe tomography to the understanding of nickel-based superalloys, *Micron* **32** (2001) 757-764.

152. A. Drexler, B. Oberwinkler, S. Primig, C. Turk, E. Povoden-Karadeniz, A. Heinemann, W. Ecker and M. Stockinger, Experimental and numerical investigations of the γ″ and γ′ precipitation kinetics in Alloy 718, *Materials Science and Engineering: A* **723** (2018) 314-323.

153. R. Lawitzki, S. Hassan, L. Karge, J. Wagner, D. Wang, J. von Kobylinski, C. Krempaszky, M. Hofmann, R. Gilles and G. Schmitz, Differentiation of γ′- and γ″- precipitates in Inconel 718 by a complementary study with small-angle neutron scattering and analytical microscopy, *Acta Materialia* **163** (2019) 28-39.

154. I. M. Lifshitz and V. V. Slyozov, The kinetics of precipitation from supersaturated solid solutions, *Journal of Physics and Chemistry of Solids* **19** (1961) 35-50.

155. C. Wagner, Theorie der Alterung von Niederschlägen durch Umlösen (Ostwald-Reifung), *Zeitschrift für Elektrochemie, Berichte der Bunsengesellschaft für physikalische Chemie* **65** (1961) 581-591.

156. C. J. Kuehmann and P. W. Voorhees, Ostwald ripening in ternary alloys, *Metallurgical and Materials Transactions A* **27** (1996) 937-943.

157. F. Theska, A. Stanojevic, B. Oberwinkler, S. P. Ringer and S. Primig, On conventional versus direct ageing of Alloy 718, *Acta Materialia* **156** (2018) 116-124.

158. R. Shi, D. P. McAllister, N. Zhou, A. J. Detor, R. DiDomizio, M. J. Mills and Y. Wang, Growth behavior of γ′/γ″ coprecipitates in Ni-Base superalloys, *Acta Materialia* **164** (2019) 220-236.

159. M. Sundararaman, P. Mukhopadhyay and S. Banerjee, Some aspects of the precipitation of metastable intermetallic phases in Inconel 718, *Metallurgical Transactions A* **23** (1992) 2015-2028.

160. J. F. Ziegler, M. D. Ziegler and J. P. Biersack, SRIM – The stopping and range of ions in matter (2010), *Nuclear Instruments and Methods in Physics Research Section B: Beam Interactions with Materials and Atoms* **268** (2010) 1818-1823.

161. R. E. Stoller, M. B. Toloczko, G. S. Was, A. G. Certain, S. Dwaraknath and F. A. Garner, On the use of SRIM for computing radiation damage exposure, *Nuclear Instruments and Methods in Physics Research Section B: Beam Interactions with Materials and Atoms* **310** (2013) 75-80.

162. P. G. Lucasson and R. M. Walker, Production and Recovery of Electron-Induced Radiation Damage in a Number of Metals, *Physical Review* **127** (1962) 485-500.

163. L. Couturier, F. De Geuser and A. Deschamps, Direct comparison of Fe-Cr unmixing characterization by atom probe tomography and small angle scattering, *Materials Characterization* **121** (2016) 61-67.

164. Thermocalc Ni-based alloys database version 10.0 (TCNI10).

165. J. L. Brimhall, D. R. Baer and R. H. Jones, Effect of irradiation on phosphorus segregation, *Journal of Nuclear Materials* **117** (1983) 218-223.

166. J. M. Perks, C. A. English and M. L. Jenkins, Radiation-Induced Segregation of Phosphorus in Nickel and Fe-Cr-Ni Alloys, in *Effects of Radiation on Materials: 14th International Symposium (Volume I)* (West Conshohocken, PA: ASTM International, 1990) p. 379-395.

167. B. Gault, M. P. Moody, J. M. Cairney and S. P. Ringer, Tomographic Reconstruction, in *Atom Probe Microscopy* (New York, NY: Springer New York, 2012) 157-209.

168. E. A. Marquis, Atom probe tomography applied to the analysis of irradiated microstructures, *Journal of Materials Research* **30** (2015) 1222-1230.

169. X. Wang, C. Hatzoglou, B. Sneed, Z. Fan, W. Guo, K. Jin, D. Chen, H. Bei, Y. Wang, W. J. Weber, Y. Zhang, B. Gault, K. L. More, F. Vurpillot and J. D. Poplawsky, Interpreting nanovoids in atom probe tomography data for accurate local compositional measurements, *Nature Communications* **11** (2020) 1022.

170. R. Hu, G. M. Cheng, J. Q. Zhang, J. S. Li, T. B. Zhang and H. Z. Fu, First principles investigation on the stability and elastic properties of $Ni_2Cr_{1-x}M_x$ (M = Nb, Mo, Ta, and W) superlattices, *Intermetallics* **33** (2013) 60-66.

171. H. C. Pai, M. Sundararaman, B. C. Maji, A. Biswas and M. Krishnan, Influence of Mo addition on the solvus temperature of Ni_2(Cr, Mo) phase in Ni_2(Cr, Mo) alloys, *Journal of Alloys and Compounds* **491** (2010) 159-164.

172. D. I. Potter and H. A. Hoff, Irradiation effects on precipitation in γ/γ′ Ni-Al alloys, *Acta Metallurgica* **24** (1976) 1155-1164.

173. J. Sprague, J. Westmoreland, F. Smidt and P. Malmberg, Effects of Dose Rate on the Precipitate Distribution in an Ion-Irradiated Nickel-Aluminum Alloy, in *Effects of Radiation on Materials, STP725-EB*, ed. D. Kramer, H. R. Brager and J. S. Perrin (West Conshohocken, PA: ASTM International, 1981) 528-540.

174. L. E. Rehn, Surface Modification and Radiation-Induced Segregation, in *Metastable materials formation by ion implantation*, ed. S. T. Picraux and W. J. Choyke (New York: Elsevier Science, 1982) 17-33.

175. R. Mouginot, T. Sarikka, M. Heikkilä, M. Ivanchenko, U. Ehrnstén, Y. S. Kim, S. S. Kim and H. Hänninen, Thermal ageing and short-range ordering of Alloy 690 between 350 and 550 °C, *Journal of Nuclear Materials* **485** (2017) 56-66.

176. P. Nash and A. Nash, The Ni−Si (Nickel-Silicon) system, *Bulletin of Alloy Phase Diagrams* **8** (1987) 6-14.

177. H. W. King, Quantitative size-factors for metallic solid solutons, *Journal of Materials Science* **1** (1966) 79-90.

178. D. J. Edwards, E. P. Simonen and S. M. Bruemmer, Evolution of fine-scale defects in stainless steels neutron-irradiated at 275 °C, *Journal of Nuclear Materials* **317** (2003) 13-31.

179. W. Chen, X. Ding, Y. Feng, X. Liu, K. Liu, Z. P. Lu, D. Li, Y. Li, C. T. Liu and X.-Q. Chen, Vacancy formation enthalpies of high-entropy FeCoCrNi alloy via first-principles calculations and possible implications to its superior radiation tolerance, *Journal of Materials Science & Technology* **34** (2018) 355-364.

180. X.-X. Yu and C.-Y. Wang, The effect of alloying elements on the dislocation climbing velocity in Ni: A first-principles study, *Acta Materialia* **57** (2009) 5914-5920.

181. L. K. Mansur and M. H. Yoo, The effects of impurity trapping on irradiation-induced swelling and creep, *Journal of Nuclear Materials* **74** (1978) 228-241.

182. E. A. Kenik, Radiation-induced solute segregation in a low swelling 316 stainless steel, *Scripta Metallurgica* **10** (1976) 733-738.

183. A. D. Brailsford and R. Bullough, The rate theory of swelling due to void growth in irradiated metals, *Journal of Nuclear Materials* **44** (1972) 121-135.

184. P. Xiu, Y. N. Osetsky, L. Jiang, G. Velisa, Y. Tong, H. Bei, W. J. Weber, Y. Zhang and L. Wang, Dislocation loop evolution and radiation hardening in nickel-based concentrated solid solution alloys, *Journal of Nuclear Materials* **538** (2020) 152247.

185. J. C. Haley, S. A. Briggs, P. D. Edmondson, K. Sridharan, S. G. Roberts, S. Lozano-Perez and K. G. Field, Dislocation loop evolution during in-situ ion irradiation of model FeCrAl alloys, *Acta Materialia* **136** (2017) 390-401.

186. J. C. Haley, S. de Moraes Shubeita, P. Wady, A. J. London, G. R. Odette, S. Lozano-Perez and S. G. Roberts, Microstructural examination of neutron, proton and self-ion irradiation damage in a model Fe9Cr alloy, *Journal of Nuclear Materials* **533** (2020) 152130.